UNIVERSIDAD AUTÓNOMA DE NUEVO LEÓN
FACULTAD DE CIENCIAS QUÍMICAS

SYNTHESIS OF POLY(3-HEXYLTHIOPHENE) ACTIVE LAYER WITH ZnO NANORODS AND Au NANOPARTICLES FOR THE FABRICATION OF HYBRID PLASMONIC SOLAR CELLS

POR

ADELA VERÓNICA GONZÁLEZ PÉREZ

COMO REQUISITO PARCIAL PARA OBTENER EL GRADO DE DOCTOR EN CIENCIAS CON ORIENTACIÓN EN QUÍMICA DE LOS MATERIALES

JULIO, 2019

“We divide the world into smaller and smaller particles, looking for answers, and we only find more questions…”

-VG

SUMMARY

Adela Verónica González Pérez **Date of graduation: Julio 2019**

Universidad Autónoma de Nuevo León

Facultad de Ciencias Químicas

Study title: Synthesis of poly(3-hexylthiophene) active layer with ZnO nanorods and Au nanoparticles for the fabrication of hybrid plasmonic solar cells.

Number of pages: 106	Candidate for the degree of Doctorate in Sciences with Orientation in Chemistry of Materials

Study area: Chemistry of Materials

Purpose and method of study: In the present study, zinc oxide nanobars were synthesized by electrochemical method and poly(3-hexylthiophene) by template-assisted method, as well as gold nanoparticles by microwave. The three components were incorporated as part of a hybrid plasmonic solar cell, in two configurations: inverted ITO/ZnO/P3HT/Au and conventional ITO/P3HT/ZnO/Au. The nanobars and nanoparticles were characterized by Fourier transform infrared spectroscopy, scanning electron microscopy, UV-Vis spectroscopy and dynamic light scattering. The solar cells were characterized with the use of a solar simulator and a picoammeter.

Conclusions and contributions: A methodology was developed to adhere polymer nanorods, vertically aligned, on ITO glass; subsequently, ZnO nanobars were formed on the polymer matrix. Two hybrid plasmonic solar cells were fabricated in which gold nanoparticles were used as cathode; the nanoparticles were incorporated into the hybrid layer of ZnO and P3HT by electrophoretic deposition, which is presented as an alternative to the deposit of conductive metals by thermal evaporation. The basic parameters of the conventional solar cell were V_{oc} = 200 mV, J_{sc} = $1.09x10^{-7}$ mA/cm^2, FF of 30%, while those of the inverted solar cell were V_{oc} = 400 mV, J_{sc} = $6.95x10^{-8}$ mA/cm^2, FF of 28%, however, the efficiencies of both were null (in the order of 10^{-7}), due to the little contact between the different components of the cell.

SIGNATURE OF THE ADVISER: _____

Dra. Ma. Idalia Gómez de la Fuente

SIGNATURE OF THE CO-ADVISOR: _____

Dr. Israel Alejandro López Hernández

ACKNOWLEDGEMENT

I would like to thank to Conacyt for the scholarship granted during these three years and for the support of the Proyect PN150.

Also, I would like to thank to “Facultad de Ciencias Químicas”, “Facultad de Ciencias Fisico Matemáticas” and “Facultad Autónoma de Madrid” for the facilities, the supplies and reagents.

Table of content

List of figures

Figure **Page**

List of tables

Table **Page**

List of abbreviations

ρ_{ext} – external charge

AAO – anodic aluminum oxide

AFM – Atomic Force Microscopy

B – magnetic flux density

D – dielectric displacement

DLS – Dynamic light scattering

E – electric field

EQE – external quantum efficiency

FF – fill factor

FTIR – Fourier transform infrared spectroscopy

FTO – fluorine tin oxide

GO – Graphene oxide

H – magnetic field

HSC – hybrid solar cells

ITO – indium tin oxide

J_{ext} – external current density

J_{sc} – short circuit current

LSPR – localized surface plasmon resonance

N_A – Avogadro number

NP – nanoparticles

PCE – power conversion efficiency

P_{max} – maximum power

SCCM – standard cubic centimeters per minute

SEM – scanning electron microscopy

SPR – surface plasmon resonance

UV – ultraviolet

Vis – visible

V_{oc} – Open circuit voltage

XRD – X-ray diffraction

η – efficiency

CHAPTER 1

1. INTRODUCTION

Increasing energy demand worldwide as well as the fossil fuels reserves reduction (petroleum, particularly) shows the urgent need to have alternative energy sources that are renewable, clean and economical, such as wind power [1–3], tidal power [4], hydropower [5–7], biomass [8] and solar energy [9–13]. The latter being the cleanest and most abundant renewable energy source available. That is why the solar energy harnessing is one of the most promising approaches to solve the growing energy problems [14, 15].

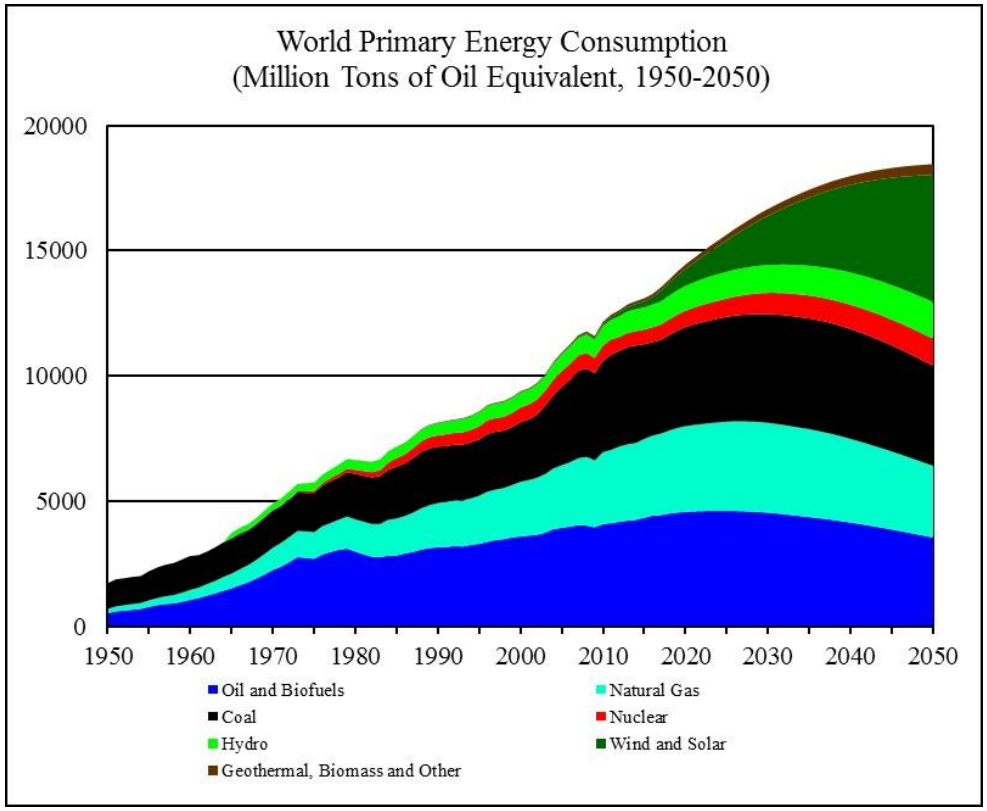

Figure 1. World historical and projected energy consumption, 1950-2050 [16].

Nowadays, the use of oil energy represents the bulk of the global energy consumption, follow by coal and natural gas, being renewable energies the least used at worldwide. However, it is expected that these amounts will be invested in the coming years, in order to reduce the damage to the environment. Figure 1 shows a scheme of the main energy sources and its consumption since the fifties, as well as the projection until the year 2050.

1.1 Solar energy

In recent years, there has been an increase in research and use of solar electric technology, being solar photovoltaics the most deployed technology nowadays. Thanks to the fact that these devices are powered by solar energy and operate at room temperature, it is possible to think of them as the ideal candidates to replace the carbon power generation.

The sun continuously delivers an average power density of 1366 W/m^2, which is reduced to 1000 W/m^2 due to atmospheric absorption and scattering, however, is highly intermittent due to the changes in the seasons, diurnal variation, clouds and weather. The main challenge is to turn this intermittent resource into a steady source of electricity [17]. To achieve this, it is important to understand the overall concept of photovoltaic energy.

Light is composed of elementary particles called photons, that are the quantum of electromagnetic field including both electromagnetic radiation and the force carrier for the electromagnetic force. When matter is irradiated, photons excite the contained electrons to a higher energy state, nevertheless, these

excited electrons returns quickly to their ground state. On the other hand, in a photovoltaic device, it is possible to pull the excited electrons toward an external circuit; this is achieved by designing asymmetries within the devices (normally with the union of semiconductors of p and n type. These asymmetries generate a barrier to current flow at one of the semiconductor - metal interfaces, better known as Schottky barrier). This effect is better explained in Figure 2.

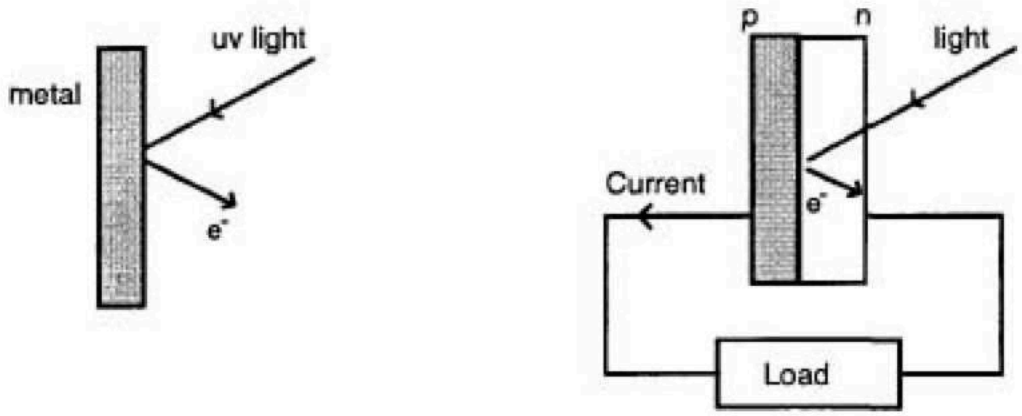

Figure 2. Comparison of the photoelectric effect (left), where UV light liberates electrons from the surface of a metal, with the photovoltaic effect in a solar cell (right), where the excited electrons are driven through the external circuit [18].

The energy contained in the excited electrons generates a potential difference that drives the electrons towards the external circuit. However, the efficiency of the photovoltaic device will depend upon the selection of the semiconductors (p and n), as well as the assembly and the position of these [18].

1.2 Inorganic solar cells

Solar energy is being exploited in different ways, but the most often used technology is that of inorganic solar cells based on silicon [19–22], in which the solar energy transformation into electricity is done through the photovoltaic effect.

These inorganic solar cells have been optimized to achieve electrical power conversion efficiencies greater than 20%, however, they require specialized manufacturing conditions involving high costs and restrict their widespread use [23–29].

1.3 Hybrid solar cells

The search for low-cost photovoltaics has led researchers to study organic materials as possible candidates [30–34]. The discovery of organic materials having properties of both conductor as semiconductor leads to new possibilities in the field of optoelectronic devices [35, 36]. Organic semiconductors have very high absorption coefficients, allowing the use in thin films to absorb a portion of the solar spectrum that allows an energy conversion efficiency of up to 7% [37–40] . Polythiophene is one of the most investigated organic polymers; its electrical conductivity can be modified between 10^{-10}-10^{5} S/cm depending on the processing technique [41–44]. It also allows the addition of metal nanoparticles to the polymer matrix, increasing the conductivity and favoring the charge transport [45–48].

Hybrid solar cells combined organic (typically conjugated polymers) and inorganic nanoparticles, in order to incorporate the advantages associated with both material groups [49–53]. The inorganic electron acceptor material may provide additional benefits to the system (as the decrease of degradation time), maintaining low production costs. These solar cells still lagged compared with organic solar cells based on fullerenes and conjugated polymers with respect to the energy conversion efficiency. However, in recent years there have been significant advances. Hybrid solar cells have the potential to exceed the performance of the organic cells while combined additional benefits such as low cost, flexibility and easy to produce [54, 55].

1.4 Plasmonic solar cells

A plasma oscillation is a collective longitudinal excitation of the conduction electron in a metal. A plasmon is a quantum of a plasma oscillation and can be defined as collective oscillation of the electron conduction in a metal surface; a plasmon can be excited by reflecting an electron/photon from a metal surface or by passing an electron through a thin metallic film. Figure 3 shows the creation of a plasmon [56].

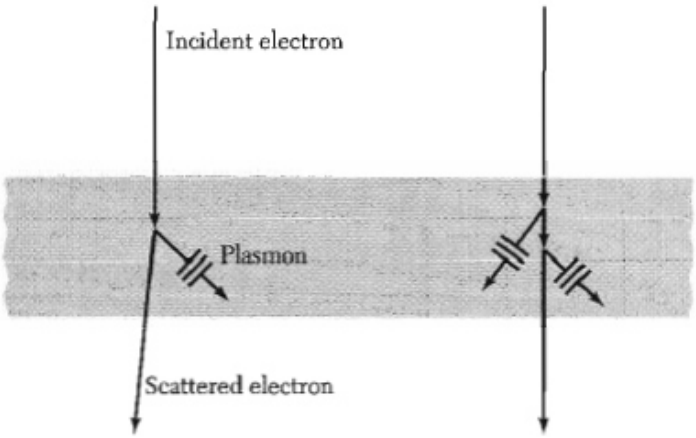

Figure 3. Creation of one and two plasmons in a metal film by inelastic scattering of an electron [56].

When a plasmon is excited, two different phenomena can take place: surface plasmon resonance (SPR) and localized surface plasmon resonance (LSPR). SPR are propagating and dispersive electromagnetic waves coupled to the electron plasma of a conductor. On the other hand, LSPR are non-propagating excitations of the conduction electrons of metallic nanoparticles coupled to the electromagnetic field. Nanoparticles are presented as a curve surface that allows an effective restoring force on the driven electrons, so that a resonance take place, leading to field amplification both inside and also in the near-field zone outside the particle. This resonance is known as localized surface plasmon [57–60].

1.4.1 Nanoparticles physical and optical properties

Gold, silver and copper are some of the most used noble metals in the nanoparticle synthesis due to its properties and the possibility of obtaining different nanoforms varying their synthesis conditions [61–65]. Metallic nanoparticles have very different physical and optical properties compared to bulk

material [66]. The size of a nanoparticle makes it possible to carry out a quantum effect by the confinement of its electrons. As a particle becomes small, its radius approach the exciton Bohr radius (and its size matches with the wavelength electron wave function), therefore the electronical, physical and optical properties are changed [67].

Optical properties of metallic nanoparticles have been of interested over the years, especially extinction, absorption and scattering properties. These optical properties can be described with the macroscopic Maxwell's equations:

$$\nabla \cdot \boldsymbol{D} = \rho_{\text{ext}} \quad (1)$$

$$\nabla \cdot \boldsymbol{B} = 0 \quad (2)$$

$$\nabla \times \boldsymbol{E} = -\frac{\partial \boldsymbol{B}}{\partial \boldsymbol{t}} \quad (3)$$

$$\nabla \times \mathbf{H} = \mathbf{J_{ext}} + \frac{\partial \boldsymbol{D}}{\partial t} \quad (4)$$

The equations present above, describe the relationship between the external charge (ρ_{ext}) and current densities ($\mathbf{J_{ext}}$) with the four macroscopic fields and: dielectric displacement (**D**), electric field (**E**), magnetic field (**H**) and magnetic flux density (**B**) [57].

Mie's theory is one the most important solution for Maxwell's equations because presents its solution of extinction = absorption + scattering (for spherical nanoparticles) in a simple and exact way [68].

1.4.2 Bimetallic nanoparticles: synergistic plasmonic effects

It has been found that the plasmonic effect can be enhanced with the combination of two different metallic nanoparticles (NP) or coupling two different nanoforms [69].

When two different metallic NP are incorporated into an active layer, some advantage can be observed, compared to solar cells containing these nanoparticles in isolation. Synergistic plasmonic effects are reflected in broader absorption in the UV/Vis spectra, improvement in external quantum efficiency (EQE) and the increment of short circuit current (J_{sc}) [70]. Also, it has been noticed that the plasmonic field generated by two different NP, facilitates the exciton dissociation while increase the charge carrier density.

1.4.3 Bimetallic nanoparticles: core-shell structures

Core-shell is a type of nanostructure that has gain special attention in the last years, due to its multiple benefits [71]. This kind of NP owes its name to the configuration of an inner material (core) and an outer layer material (shell), that could be of multiple compositions, organic/organic, inorganic/inorganic, organic/inorganic and inorganic/organic materials. When noble metal core-shell NP are incorporated into a device, some special characteristics can be observe, on one hand, the cavities allow an energy resonance that compensates for losses due to energy dissipation [72], on the other hand, the plasmonic fields resulting from the confinement effect, can improve the light scattering.

1.5 Hybrid plasmonic solar cells

Recently, metallic nanoparticles have been used to improve light absorption in hybrid active layers [49, 73–75]. This absorption improvement, due to the presence of metallic nanoparticles, is typically induced by two physical mechanisms. In the first, nanoparticles serve as additional traps of photons in the active layer [76, 77]. For effective implementation of this mechanism, periodic nanostructures are placed in front of the electrode-active layer interface, prior to deposition of the active layer. Under such conditions, the nanoparticles exhibit a SPR that is scattered strongly and improves the light absorption of the active layer. In the second mechanism, nanoparticles are embedded within the active layer so that the LSPR induces a near-field which enhances the absorption in neighboring particles [78, 79] (Figure 4).

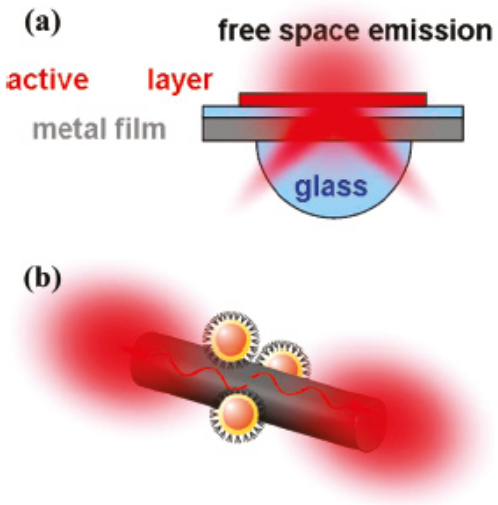

Figure 4. Exciton-plasmon interactions. (a) Surface plasmon in volume. (b) Localized surface plasmon in nanoparticles [80].

One of the biggest challenge in hybrid solar cells (HSC) is to solve the problem of the ineffective light absorption while still keeping a thin active layer [81]. Plasmonic nanomaterials offer promising routes to solve the limitations of conventional hybrid solar cells. Specifically, the plasmonic materials have been highly exploited for the effective promotion of photons absorption in the active layers. It has been found that hybrid nanostructures integrating more than two different compounds are highly necessary for the development of optical properties in the solar cells [73, 74, 77, 82].

It has been known that the improvement of optical properties in solar cells, can also be achieved when metallic nanoparticles are place on the front surface or at the back surface of a solar cell. The first of these, is presented under two configurations: randomly distributed and periodic nanostructures. When metal nanoparticles are randomly distributed on the front surface of a solar cell, plasmonic interactions allow an increase of light scattering and optical path length, resulting in improved absorption and therefore in an increase of power conversion efficiency [83–86]. On the other hand, when periodic nanoparticles are place on the top surface, an increase in scattering and guiding of light is observed, resulting in enhanced absorption. Also, it has been found that controlling the size, distribution and distance between the nanoparticles, the efficiency of a solar cell can be varied [21, 55, 87–89].

Placing metal nanoparticles on the back surface of a solar cell can also bring benefits to the optical properties, since can reduce scattering loss present in solar cells with nanoparticles placed on the top surface; the enhanced field

resulting from metallic nanoparticles, helps to increase light trapping and propagation across the active layer. Nevertheless, interactions between semiconductors and back surface nanoparticles can occur, leading to an increase of the charge transport recombination [90–94].

Nowadays, many investigations, have aimed at solving the problem of low efficiency light absorption in the active layer of hybrid solar cells. However, achieve a high current density and overcome the low efficiency of hybrid solar cells, it is still an unsolved problem [95].

1.6 Placing metal nanoparticles in the active layer according to its efficiency

1.6.1 Parameters of a solar cell

There are four parameters that are considered as the key performance characteristics of a solar cell: Open circuit voltage (V_{oc}), short circuit current density (J_{sc}), fill factor (FF) and efficiency (η) (also called power conversion efficiency, PCE). Theses parameters must be measured in specific illumination conditions, according to the Standard Test Condition, which are: Air Mass 1.5 spectrum, incident power density of 1000 W/m^2 and 25°C [18].

When the current is zero, in a solar cell, the potential difference has its maximum value, that is to say, a maximum voltage, V_{oc} and can be calculated as follow:

$$V_{oc} = \frac{kT}{q} \ln\left(1 + \frac{I_{ph}}{I_0}\right) \quad (5)$$

where k is Boltzmann's constant, T is the absolute temperature, q is the magnitude of the electronic charge and I_{ph} and I_0 are the saturation and photogenerated currents respectively.

Fill factor is a parameter which determines the maximum power of a solar cell (besides V_{oc} and J_{sc}) and describe the "squareness" of the I-V curve.

$$FF = \frac{P_{max}}{I_{sc}V_{oc}} \quad (6)$$

The short circuit current density is the current through a solar cell when the voltage is fixed to zero, and can be related to the incident spectrum trough the cell's quantum efficiency (QE) as follow:

$$J_{sc} = q \int b_s(E) QE(E) dE \quad (7)$$

where $b_s(E)$ is the incident spectral photon flux density.

Finally, the efficiency of a solar cell can be defined as the ratio of energy output to incident energy from the sunlight, and is calculated as follow:

$$\eta = \frac{J_{sc}V_{oc}FF}{P_s} \quad (8)$$

Where P_s is the incident light power density [96–100].

1.6.2 Maximizing the parameters

Table 1 shows a summary of how the efficiency of a hybrid solar cell is increased or decreased according to the form and the place of the metallic nanoparticles in a solar cell.

Table 1. Summarized list of modifications in efficiency according to NP placed in different sites of an active layer or solar cell.

NP	Place	NP form	Efficiency (%)	Increase (%)	Ref
		Inorganic solar cells			
Ag	Surface of active layer	Nanospheres	12.4	-	[22]
Ag	Surface of transparent electrode	Nanowires	5.6	12	[83]
Ag	Electrode	Nanowires	16	6.67	[84]
Ag	Electrode	Nanowires	3.2	-22	[85]
Au, Ag	On solar cell surface	Nanospheres	9.5	18.8	[86]
Au@Ag	Between cathode/HTL	Core-shell	2.69	20.09	[89]
Au	Photoanode	Nanospheres	1.73	4.22	[91]
Ag	Photoanode	Nanospheres	0.6	114	[92]
Ag	P-layer N-layer Both (p-n) Interface	Nanospheres	1.48 0.68 1.15 0.59	56.0 -28.4 21.1 -37.9	[49]
Ag	Between Al substrate/active layer	Nanotextured layer	6.36	10.6	[87]
Al	Between Al back reflector/active layer	Grating	25	-	[88]
Au	Top surface of p-layer	Nanostars	-	20	[23]
Pd	Surface of active layer	Nanospheres	7.02	85.2	[101]
Ag	Inside of the active layer	Hexagonal nanohemisphere	6.55	5	[102]
		Organic solar cells			
Au	Between ITO/active layer	Nanodots	3.65	20.1	[103]
Ag	Between ITO glass/HTL	Nanospheres	3.69	21	[93]
Cu-Au	Embedded in P3HT	Core-shell	8.48	12.6	[70]
Au@Ag	Embedded in HTL	Core-shell nanocubes	6.3	18.9	[104]
Au	Embedded in P3HT	Nanorods	1.94	27	[105]

Au	Inside of the active layer	Nanospheres	1.84	3.95	[106]
Ag	Between two HTL	Various shapes	1.99	-10.4	[36]
Ag	Between HTL/active layer	Nanospheres	1.2	-45.4	[107]
Au	Embedded in HTL	Nanospheres	3.51	13.2	[108]
Ag	Between HTL/active layer	Nanospheres	2.75	64.7	[109]
Au	Between ITO/active layer	Nanospheres	2.21	7	[110]
Au	Embedded in HTL	Various shapes	9.26	19.8	[111]
Ag	Embedded in HTL	Island thin film	4.01	31.5	[112]
Au@SiO_2	Into active layer	Core-shell	3.80	15.5	[113]
Ag	Between ITO/HTL	Nanosheets	3.6	28.6	[114]
		Hybrid solar cells			
Ag	Electrode	Thin layer	4.83	34	[21]
CdTe	Between HTL/inorganic layer	Quantum dots	7.60	28.8	[54]
WO_3	Between electrode/HTL	Thin layer	11.7	11.5	[55]
Ag	Top surface of HTL	Nanospheres	22.6	23.8	[115]
Au-Ag	Photoanode	Alloy NP	5.81	52.1	[90]
Ag	Embedded in anode buffer	Nanospheres	3.4	14	[94]
Bi_2Te_3	Inside of HTL	Hexagonal nanoplates	12.1	30.1	[116]
Au	Inside of HTL	NP	6.10	10.9	[117]
Ag@TiO_2	Inside of the active layer	Core-shell	13.7	20.2	[118]
Au	Between HTL/organic layer	Nanospheres	7.25	17.3	[119]
Au	Embedded in HTL	Nanospheres	12.85	23.2	[120]
Ag	Embedded in P3HT	Nanospheres	4.23	41.9	[121]
Ag	Embedded in active layer	Nanoplates	9.6	12.9	[122]
Au	Embedded in inorganic layer	Nanospheres	3.25	20.4	[123]
Ag@SiO_2	Embedded in inorganic layer	Core-shell	3.68	7.92	[124]
Ag	Embedded in Si nanoholes	Nanospheres	4.8	100	[125]

Note: HTL refers to hole transporting layer, PEDOT:PSS (Poly(3,4-ethylenedioxythiophene)-poly(styrenesulfonate)) and P3HT refers to (poly(3-hexylthiophene)).

1.7 Au nanoparticles: synthesis methods

In recent years, gold nanoparticles have become the object of numerous studies due to their unique optical and physical properties. These nanoparticles have an endless number of applications in medicine [126, 127], sensors [128, 129], nanoengineering [130], solar cells [111, 123], among others [131–134]. All these areas exploit the optical property of Localized Surface Plasmon Resonance (LSPR) which oscillates around 500 nm depending on the size of the nanoparticle.

A great variety of syntheses have been proposed over the years, being the $HAuCl_4$ the most used precursor for colloidal gold. These variations include the use of reducing agents [135], stabilizing agents [136], reaction medium [137], pH control [138], reaction temperature [139], among others. Gold nanoparticles are obtained mainly by conventional heating method and microwave synthesis, being the latter the most studied in recent years, due to short synthesis times and small amounts of reagent. The synthesis conditions influence the particle size and therefore the LSPR.

Gold nanoparticles are mainly characterized by UV-Vis absorption spectrum, with which the extinction coefficient can be calculated if other parameters are known. Extinction coefficient (ε) is an important parameter that allows the average diameter and the estimation of nanoparticles concentration, however it is necessary to know the molar concentration, which is a problem due to the low monodispersity of the nanoparticles [140]. s

1.8 Nanorods: synthesis techniques

Some researchers have emphasized the importance of incorporating both the conductor and the semiconductor material in nanorod shape [141–145]. The advantage of this shape is that, in contrast to the NP network, the charge carriers can be transferred to the electrodes through the nanorods without losses due to recombination at the nanoparticles boundaries. Generally, it can be defined two distinct trends, the bottom-up ("atom-by-atom") and top-down ("etch off") [146]. The first of these methods refers to the buildup of a nanomaterial from the bottom, atom-by-atom; while the second one refers to slicing a bulk material to get a nanomaterial [147, 148]. As applied to nanorods, the bottom-up growing techniques include processes of growth either from vapor phase (D) or from aqueous solution (W), whereas the top-down technique needs crystalline substrate to be etched to form a nanorelief (Figure 5) [146].

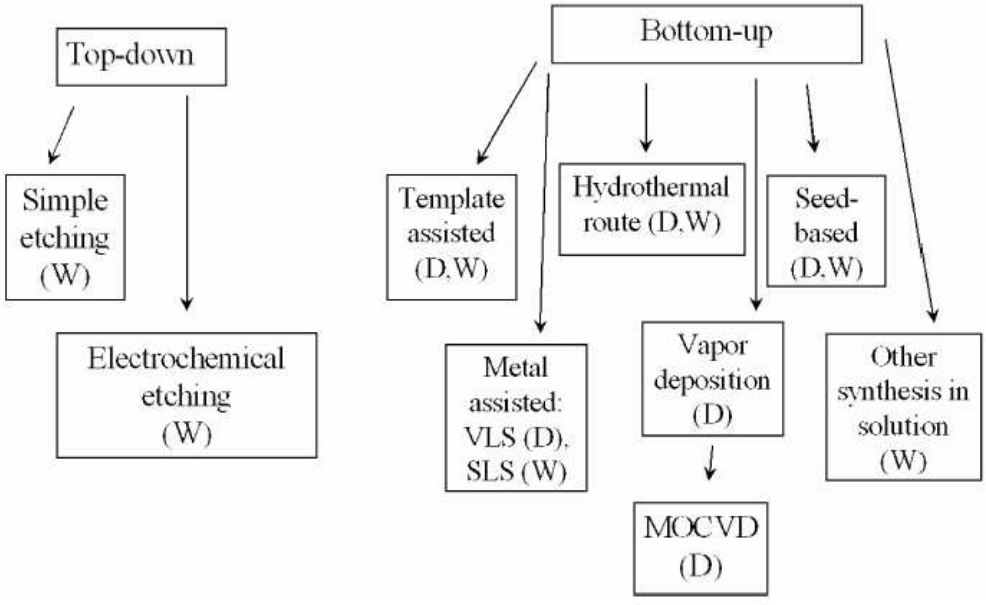

Figure 5. Schematic presentation of technological techniques available for nanorods production [146].

1.8.1 Template assisted method

One of the most widely used bottom-up methods to obtained nanorods is the synthesis of nanoporous anodic aluminum oxide (AAO); it has become a commonly used material with potential applications in a wide range of areas, such as catalysis, bionanotechnology, electronics, photonics, photoelectronics, and sensing [149]. An AAO layer is widely used as a template to prepare various nanostructure arrays. The AAO layer can provide close packed vertical channels with controlled diameters of 4–200 nm by adjusting both the anodization conditions and the pore-opening conditions [150]. It has been used mainly as a template for fabricating a variety of hybrid nanomaterials by electroplating different materials into its nanopores [151].

2. BACKGROUND

As a promising alternative to inorganic silicon solar cells, in 1991 Brian Oregan and Michael Grätzel invented a solar cell dye-sensitized consisting of liquid electrolyte and TiO_2 films, however, these cells need to be sealed to prevent the leakage of the electrolyte [152]. In 1998 Hagen et al. published a report combining the advantage of organic and inorganic materials with the name of new hybrid solar cells. These cells consisted in TiO_2 and $C_4H_6O_3$ mixed with LiI, I_2 and a ruthenium complex as a sensitizer. Although the assembly of the cell was performed successfully, the cell just achieved 0.02% of external quantum efficiency [153]. After this, many research groups have focused on replacing an inorganic material with different types of polymers.

2.1 Hybrid solar cells

In 2014, Ko et al. incorporated two amine derivatives as hole transporting materials for the fabrication of a hybrid solar cell. Two cell designs utilizing planar amine and triphenylamine in perovskite cells were investigated; cell design using planar amine as hole transporting material, showed a conversion efficiency of 13.63% [154]. A year later, they designed two hybrid perovskite cells in which two or four N,N-Di(4-methoxyphenyl)aminophenyl were used. Solar cell in which the four N,N-Di(4-methoxyphenyl)aminophenyl was used, reached a conversion efficiency of 12.77% [155].

In 2015, Z. Ge *et al.* [54] fabricated silicon nanowire and cadmium telluride quantum dots to fabricate organic hybrid solar cells. Transmission electron microscopy analysis revealed that cadmium telluride quantum dots were uniformly distributed on the surface of the silicon nanowires, which made poly(3,4-ethylenedioxythiophene):poly(styrenesulfonate) (PEDOT:PSS) easily filled the space between silicon nanowires. The current density–voltage characteristics of hybrid solar cells were investigated both in dark and under illumination. The result shows that the performance of the hybrid solar cells with cadmium telluride quantum dots layer has an obvious improvement. Power conversion efficiency of solar cells increases by 28.8%. The enhanced performance of the hybrid solar cells with quantum dots layers are ascribed to the modification of the silicon nanowires surface with the cadmium telluride quantum dots.

In 2015, X. Mu *et al.* [55] incorporated a WO_3 thin layer between the Ag front electrodes and PEDOT:PSS film in a PEDOT:PSS/silicon solar cell to increase the power conversion efficiency. With this structure it was possible to suppress the carrier recombination at the interface of silicon and electrodes, and meanwhile, the contact resistance between the Ag electrodes and PEDOT:PSS film is largely reduced. The solar cell displays a power conversion efficiency of 11.65%, which is much higher than the one without a WO_3 thin layer (10.45%).

2.2 Plasmonic solar cells

Despite the many advantages associated with metallic NPs in solar cells, some studies have shown that NPs can as recombination centers, causing a global reduction in the parameters of the solar cells, whereby the architecture and a proper dispersion are key factors for cell performance enhancement.

In 2014, S. Sánchez de la Morena *et al.* [20] performed electrodeposition of gold nanoparticles into porous silicon to develop plasmonic solar cells. They fabricated a cell with a configuration of Al/Si/PS/ITO which it was used as a control device to be compared with a cell of Al/Si/PS + Au/ITO. The results indicate that the presence of gold nanoparticles increases the spectral response from $9x10^{-6}$ a $9x10^{-4}$ A/W at 400nm, which increases with increasing concentration of nanoparticles. This effect may be associated with increased light absorption and the increase in conductivity caused by the presence of metallic nanoparticles.

As was mentioned before, addition of metallic NPs not always has positive consequence in the performance of a solar cell. In 2015, U. Dasgupta *et. al.*, develop a complete study of the incorporation of metal nanoparticles in different places of pn-junction solar cell and its consequence in the PCE. For this study, Ag NPs were placed at p-layer, n-layer, in both layers and at the interface of pn-layer. Copper, zinc, tin and sulfur (CZTS) and Cu@$AgInS_2$ were used as p- and n-layers, respectively; ITO and Ca/Al were used as electrodes. Results show that

the incorporation of metal nanoparticles in p-layer evidence an increase of 56% in efficiency compared with control device, while the incorporation in n-layer reduce efficiency dramatically in 28% because the nanoparticles act as trap for the electrons hindering its transport, reducing its efficiency even more if nanoparticles are placed at interface of the layers (38%). nanoparticles should be placed only in p-layer so that electron transport remains unaffected [49].

In 2015, M. Eskandari *et al.* synthesized a solar cell using ZnO nanorods decorated with Ag nanoparticles as photoanode. The performance of the synthesized cell was compared with a cell without Ag NPs, and the results show that the phenomenon of surface plasmonic resonance, as well as light scattering, causes an enhanced absorption in the photoanode and therefore a global improvement in the performance of the solar cell, which leads to an increase in efficiency of 114%. Also, measurements of electrochemical impedance spectroscopy revealed the increase of hole transfer kinetics and chemical capacitance [92].

Silver is one of the most utilized noble metal in optoelectronic applications, due to its high conductivity and plasmonic properties. Z. Liu et al. in 2015, studied spectral and opto-electronic conversion properties of a hybrid cell to which Ag NPs were incorporated, with the aim of improving the light absorption at the short wavelength based on LSPR effects. For the fabrication of the solar cell, Ag NPs

were deposited by spin-coating on silicon wafers and then the samples were subjected to an etching process for the formation of Si nanoholes; at the end of the process, Ag NPs fell into the holes. Etching time was varied in 10, 20 and 30 min and the manufactured solar cells were compared with solar cells without NPs. The results demonstrate that the optical absorption spectra shows an enhancement of total absorption at the short wavelength; current-voltage measurement shows that the solar cell with Ag NPs exhibit an increase of the power conversion efficiency of 100% in comparison with those without Ag NPs [125].

As mentioned earlier, silicon solar cells are the most often used technology in the photovoltaic industry, therefore, present the problem of inefficient absorption of light which limits the conversion efficiency. M. Atyaoui *et al.* in 2016, studied the effect incorporating palladium nanoparticles into a silicon solar cell. For the synthesis of the cell, a silicon wafer was used as p-type semiconductor in which palladium nanoparticles were placed on its base and a phosphorous diffusion was used as n-type region, to finally add silver paste as front contact and aluminum/silver paste as rear contact by screen printing. According to results of internal quantum efficiency and I-V measurements, the incorporation of palladium nanoparticles leads to a significant improvement of the light absorption and therefore its photovoltaic properties, which is attributed to LSPR effects. The silicon solar cells with palladium nanoparticles, has an increased efficiency of 85.2% compared to a silicon solar cells without palladium [101].

2.3 Hybrid plasmonic solar cells

Recent studies have shown the effectiveness of incorporating a polymer matrix to an active layer, which is favored by incorporating plasmonic nanoparticles.

According to R. Kim *et al.*, an easy way to induce the LSPR into a solar cell is through discontinuous metal film obtained by electron-beam deposition. In 2012, they synthesized an organic solar cell with Ag NPs, in which pure silver was deposited by electron-beam onto ITO glass, follow by spin-coating of PEDOT:PSS. For the active layer, P3HT and PCBM ([6,6]-phenyl-C61-butyric acid methyl ester) were also deposited by spin-coating to finally apply a layer of LiF/Al as electrode. Based on the optical analysis, an increased optical absorption is observed in the organic solar that utilizes silver nanoparticles leading in an increase of PCE of 64.7%. Simulation results indicate that the strong optical intensity associated with LSPR has consequently, an enhanced exciton generation, and can be conclude that the use of silver nanoparticles enhanced the electrical field excited by SPR at the interface between the nanoparticles and its surroundings [109].

In 2014, Qu *et al*. designed a hybrid plasmonic solar cell, wherein the active layer consisted in a P3HT:PCBM polymer with TiO_2 nanorods decorated with Ag

NP. With this arrangement it was possible to increase the photocurrent and PCE increased from 2.57% to 4.87% compared to a cell without NP [95].

In 2015, T. Segal-Peretz *et al.* [73] incorporated plasmonic gold nanostructures in titania-conjugated polymer devices in order to enhance the absorption of sunlight in hybrid photovoltaic devices. Two plasmonic structures were designed and studied. In the first, agglomerates of gold nanoparticles of 150 nm in diameter were positioned at the interface of the active layer and ITO electrode. In the second structure, 5 nm isolated Au nanoparticles were suspended inside the hybrid active layer to induce localized plasmonic field enhancement. The optical absorption measurements confirmed that both plasmonic structures enhance light absorption; therefore, it is possible to manufacture a device that combines the structures for a twofold increase in photocurrent generation.

In 2015, L. Hong *et al.* [82] incorporated periodic silver nanospheres on Si/PEDOT:PSS hybrid solar cell for absorption enhancement based on the plasmonic effect. The light absorption is found to improve significantly in the presence of the silver nanospheres, achieving a maximum efficiency of 22.6% when the periodicity was 600 nm and the nanosphere diameter 270 nm. The efficiency was increased by 23.8% compared to the hybrid solar cell without silver nanospheres.

As was mentioned before, the use of bimetallic nanoparticles has attracted researches attention due to the good stability and possibility to absorb light in a wide wavelength range compared to individual nanoparticles, specially Au-Ag alloys has been used to enhance the optical properties of optoelectronic devices. In 2016, M. Al-Azawi *et al.*, synthesized a plasmonic dye-sensitized solar cell in which sensitizer dye [RuL2(NCS) 2]: 2TBA (L = 2,2'-bipyridyl-4,4'-dicarboxylic acid: TBA = tetra-n-butyl ammonium) (N719) was used for this purpose; the rest of the solar cell was composed of fluorine-doped tin oxide (FTO)-coated glasses and TiO_2 paste. Au-Ag alloy nanoparticles where synthesized and FTO - TiO_2 coated glasses were used as substrates for photoanodes; the substrates were dipped into alloy nanoparticles solution to obtain a plasmonic photoanode. Three different devices were fabricated: a device without NPs, a device with Au NPs and a device with Ag-Au alloy nanoparticles. The experimental results showed a broad optical absorption of the dye sensitized solar cell with plasmonic photoanode, due to the synergistic effects of Au and Ag. The incorporation of Au-Ag alloy nanoparticles to the anode of the solar cells presented an increase of 52.1% in PCE [90].

In an attempt to reduce the associated problems of polymer solar cells, i.e. low photocurrent generation, low PCE, low carrier mobility, etc., some researchers have focused their attention in the use of graphene derivatives, including graphene oxide (GO). Graphene properties, such as, tunable bang gap, high electrical conductivity and carrier mobility, make it a promising material for

optoelectronic applications. In 2016, T. Mahmoudi *et al.*, synthesized a bulk heterojunction hybrid solar cell in which Ag and graphene oxide nanocomposites where incorporated into the active layer. The solar cell was composed of ITO/ZnO(58 nm)/P3HT:$PC_{60}BM$:Ag-GO(190 nm)/PEDOT:PSS/Ag(100 nm) and two different devices where fabricated: without nanocomposites (control) and with Ag-GO nanocomposites. According to the results, the solar cell containing Ag-GO showed a substantial increase in PCE (about 42%), which is attributed to an increase in J_{sc} [121].

According to X. Ren *et. al.,* one of the main problems of introducing metallic NPs to semi-transparent solar cells, is precisely the loss of transparency and therefore the global affectation of the performance of the solar cell. One way to avoid this, is the use of dielectric nanomaterials conversely into the electrodes, which can improve cell performance reducing light reflection. In 2015, they synthesized a hybrid electrode composed of Ag, Si NPs and tris(8-hydroxyquinolinato) aluminum (Alq_3) as dielectric nanomaterial. The electrode was coupled to a hybrid solar cell and its performance was compared with two hybrid solar cells with Ag transparent electrodes (10 and 100 nm), the first of these was illuminated form Ag electrode, while the second was illuminated from ITO. Parameters measurements revealed that the synergistic light effect of Si NPs and Alq3 induces an enhancement of 34% of the PCE [21].

As well know, silver film is one of the most utilized electrodes in solar cells due to its electrical properties, however speaking in industrial scale implies a high cost to be produced. Ag nanowires are presented as a lower cost alternative to reduce the quantity of silver used; these structures also present two plasmonic signals (longitudinal and transverse) which can improve optical properties in optoelectronic devices. In 2015, R. Jarrett *et. al.*, synthesized Ag nanowires from salt mediated polyol process and were deposited into a glass to be utilized as electrode of the inorganic solar cell. Thanks to its plasmonic properties, the incorporation of Ag nanowires to crystalline solar cells increase light transmission in 22%. However, the electrical properties of solar cells containing nanowires tends to reduce compared to solar cells without nanowires. This behavior is attributed to low contact between Ag nanowires and silicon substrate having as consequence a PCE reduction of 22% [85].

The correct distribution of metallic nanoparticles is a key factor to achieve an increase in optical properties by excited localized surface plasmon; avoid its agglomeration is one of the biggest problems in synthesis of NPs. W. Yoon *et. al.*, synthesized a colloidal silver nanoparticles solution using suitable organic capping groups as stabilizers. The synthesized solar cells were ITO/PEDOT:PSS/P3HT:PCBM/Ca/Al (which was used as control device) and ITO/PEDOT:PSS/AgNP/P3HT:PCBM/Ca/Al. Solar cell containing silver nanoparticles has a current rectification ratio of 26 V, which is much lower than the control device ($1x10^5$ V). Results suggest that silver nanoparticles increased

surface recombination at the interface between PEDOT:PSS and P3HT:PCBM, also act as energy barrier for charge extraction and injection, leading in a efficiency reduction of 45.4% [107].

2.4 Nanorod shape in active layers

ZnO is a wide band gap semiconductor with an energy gap of 3.37 eV at room temperature. ZnO has large exciton binding energy (60 meV) which allows UV lasing action to occur even at room temperature. Recently, one-dimensional (1D) nanoscale materials, i.e. nanorods and nanowires, have received considerable attention due to the remarkable properties applied in optoelectronic and electronic fields. ZnO nanorods have been intensively investigated for their notable properties [156–161].

In 2010, H. He *et al.* [162] decorated ZnO nanorods with Au nanoparticles. ZnO nanorods arrangement was made by chemical vapor deposition on Si wafer and gold nanoparticles were prepared by laser ablation of a gold metal target in deionized water to form a colloidal solution. ZnO nanorods were decorated by electrophoresis deposition in the Au colloidal solution. Experiments revealed that suitable electrophoretic potential, gold NP size control and enough spacing between each nanorods are crucial parameters to obtained homogeneous and strong surface decoration. They also founded that Au NP have good interfacial connection and strong binding with ZnO nanorods.

In the present year, N. Sabri *et al.* [163] investigated different polymer deposition parameters in order to improve the performance of the hybrid organic solar cells based on ZnO/P3HT. ZnO nanorods were grown on FTO by an aqueous hydrothermal method, follow by spin coating of P3HT. The three parameters studied were: the best polymer concentration, spin coating speed and diluted polymer concentration, and the results were 35 mg/mL, 1000 rpm and 1 mg/mL respectively. They conclude that the surface roughness, P3HT top layer thickness and P3HT infiltration contributed to the photovoltaic performance improvement.

2.5 Synthesis by template AAO assisted method

In 2014, S. Liu *et al.* [164] fabricated thin film of porous anodic aluminum oxide (AAO) on tin-doped indium oxide (ITO) substrates through via radio frequency sputtering process, in which a layer of 1,000 to 2,000 nm of Al was applied. A fast anodization process in phosphoric acid was performed. The electrolyte was the mixture of ethanol and water with a ratio of 1:4 and 2.5 wt% of phosphoric acid at 195 V and -4 °C. After this, to enlarge the holes, a phosphoric solution of 5 wt% was added at 45 °C for 30 min. They followed the current-time transitions of the anodization and founded that the barrier layer can be removed by extending the anodizing time, and with this, the physical and electrical contact between the pore and the substrate is allowed.

In 2014, P. Houng *et al.* [149] fabricated two structures of AAO on glass. In the first (structure a), a 200 nm thick Al layer was deposited on glass substrates and in the second structure (structure b), Al layer was deposited on ITO/glass substrate; both depositions were performed via sputtering. The structure a was anodized in 0.1-0.6 M H_3PO_4, 5-35 °C and 20-60 V, while the structure b in 0.3 M H_3PO_4 at 3°C and 20-120 V. Following anodic oxidation, the etching was done in 6 wt% H_3PO_4 at 30°C and 20-60 V for the structure a, and at 45°C and 80-120 V for structure b. This etching step enlarged the pores and removed the barrier layer. Finally, both structures were annealed in ambient atmosphere at 520 °C for 9 min to convert the Al in alumina. These last two steps enhanced the optical transmittance of the structures. They conclude that the second structure is more suitable for use in optoelectronic devices owing to its improved light transmittance in the near infrared region.

2.6 Critical analysis

In 2014, D. Pourjafari [165] developed an active layer consisting in nanorods of P3HT and ZnO. P3HT nanorods where made by template AAO assisted method, however this template was made starting from a high purity aluminum foil and for the application in a solar cell it's not enough. Now the problem to solve is how this active layer can be transported to ITO glass (anode) without losing its configuration of vertically aligned nanorods, to finally apply the

cathode layer. One way to solve this, is to deposit an aluminum layer direct on the glass and proceed with the synthesis of the template.

Based on the background can be concluded that the poly(3-hexylthiophene) as organic material, ZnO as inorganic material and Au NP as plasmonic elements are promising materials for the fabrication of hybrid plasmonic solar cells. The challenge will be to achieve the optimal arrangement which will produce the greatest efficiency of energy conversion.

This project proposes the design of a hybrid plasmonic solar cell with an active layer composed of Au nanoparticles in a conductive polymeric matrix (poly(3-hexylthiophene) (P3HT) nanorods) with ZnO nanorods to get an arrangement that, according to their characteristics, would increase the efficiency of converting solar energy into electrical energy in a photovoltaic system. Nanoparticles of different sizes and thicknesses will be placed on ZnO nanorods surface. It will be used an aluminum cathode and an indium tin oxide (ITO) glass anode as is shown in Figure 6.

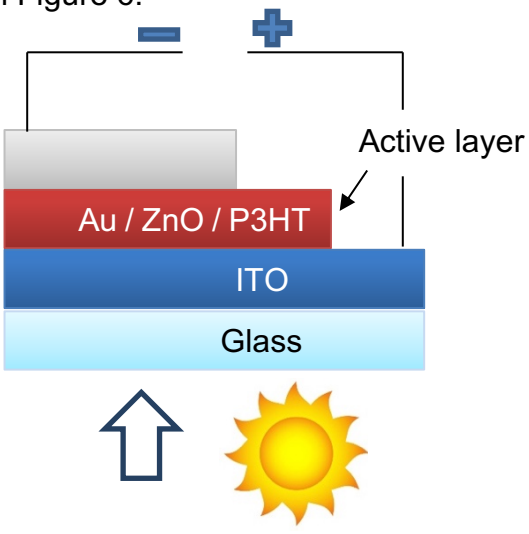

Figure 6. Proposed design for solar cell.

2.7 HYPOTHESIS

Electrophoretic deposition of Au nanoparticles on a polymeric template of poly(3-hexylthiophene) and ZnO nanorods increases the energy conversion efficiency in a hybrid solar cell by exciton-plasmon interactions.

2.8 OBJECTIVES AND GOALS

2.8.1 General objective

Synthesis of a hybrid plasmonic active layer of ZnO nanorods and Au nanoparticles in P3HT to fabricate a hybrid plasmonic solar cell.

2.8.2 Specific objectives

- Fabrication of anodic aluminum oxide (AAO) template.
- Synthesis of P3HT by electrochemical method, using the AAO template as substrate to deposit the polymer into its pores.
- Synthesis of ZnO nanorods in the polymeric template.
- Synthesis of Au nanoparticles.
- Characterization of the hybrid plasmonic active layers consisting of metallic nanoparticles, ZnO nanorods and a polymeric phase.
- Fabrication of a solar cell using the hybrid plasmonic active layer synthesized, a phase of aluminum as cathode and ITO glass as anode.

2.8.3 Scientific goals

- Obtain a plasmonic hybrid active layer for fabricating solar cells.
- Optimize the arrangement of ZnO and Au nanoparticles which allows higher energy conversion percentages.

2.8.4 Academic goals

- Presentation of the results in at least one specialized international congress.
- Publication of at least one article in journal indexed in JCR.

3. METHODOLOGY

3.1 Aluminum deposition via sputtering

Anodic Aluminum Oxide (AAO), was fabricated for two methods: deposition of aluminum by sputtering onto ITO glass and by anodization of high purity aluminum. Both methods are explained below.

High purity aluminum (99.9995%) was deposited on ITO glass by sputtering technique followed by with the anodization processes to form an AAO template on glass and solve the problem of maintaining the vertically aligned nanorods configuration. This deposition was done in a Magnetron Sputtering Chamber assisted by Radiofrequency.

3.2 Fabrication of an anodic aluminum oxide (AAO) template on ITO

A template was fabricated with a thickness of 2 μm and a pore size of 50 nm on ITO glass. Fabrication consist of 4 steps:

1. First anodization. The aluminum thin film was immersed into a cell containing 0.3M oxalic acid solution, applying a voltage of 40 V and keeping a temperature of 10°C by Peltier effect for 40 min.
2. Etching. The oxide layer formed on aluminum surface in the first anodization was etched in a solution of 1.8 wt% chromic acid and 5 wt% phosphoric acid keeping a temperature of 65°C for 40 min.

3. Second anodization. The sample from etching step was placed at the bottom of a cell containing 0.3 M oxalic acid, at a temperature of 10°C and 40 V for 10 min.
4. Dissolving the barrier layer. The remaining aluminum was dissolved in 0.1M $CuCl_2$ solution, 50 ml of distilled water and 25 ml of HCl. Finally, the barrier layer was dissolved in 5 wt% H_3PO_4 at 30°C for 30 min.

Figure 7 represents a scheme of the template synthesis on ITO glass in five steps:

a) Deposition of Al film on ITO glass via sputtering
b) First anodization
c) Second anodization
d) Dissolving the barrier layer
e) Template ready for electrodepositions

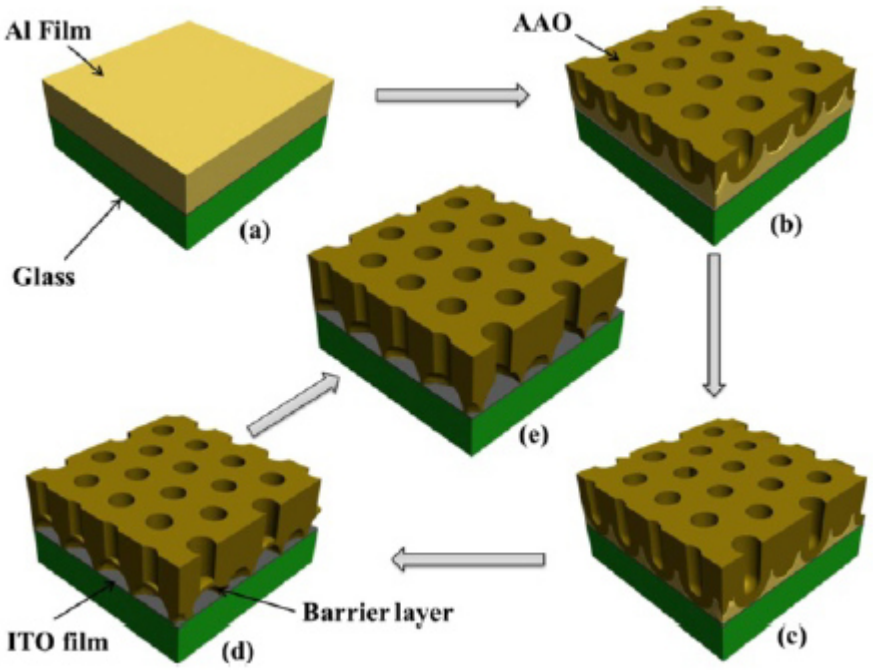

Figure 7. Representation of a template synthesis on ITO glass.

For the anodizing cell, two configurations were tested. In the first configuration, configuration “a”, the substrate containing aluminum film, was placed at the bottom of the cell (Figure 8a), however, this configuration was designed for a substrate that is conductive in all its volume, and the glass with aluminum needs to be painted with silver paint. To avoid this problem, a second configuration, configuration “b”, was designed, in which cathode and anode are placed at the top of the cell (Figure 8b).

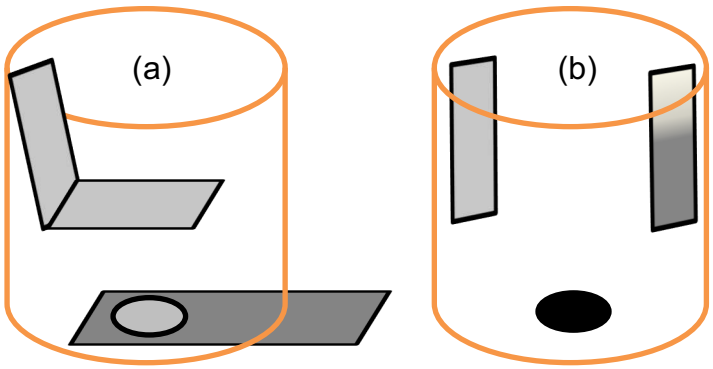

Figure 8. Internal view of the two configurations of anodizing cell.

3.3 Fabrication of an anodic aluminum oxide (AAO) template on high purity aluminum

A template was fabricated with a thickness of 2 μm and a pore size of 50 nm. Fabrication consist of 5 steps:

1. Electropolish. High purity aluminum was immersed in a conductive cell containing $HClO_4$ y C_2H_5OH (1:4) at 7 ºC and 20 V during 40 min.
2. First anodization. High purity aluminum was immersed into a cell containing 0.3 M $H_2C_2O_4$, applying a voltage of 40 V and keeping a temperature of 10 °C by Peltier effect for 12 h.
3. Etching. The oxide layer formed on aluminum surface, in the first anodization, was etched in a solution of 1.8 wt% H_2CrO_4 and 6 wt% H_3PO_4 keeping a temperature of 65 °C for 5 h.
4. Second anodization. The sample from etching step was placed at the bottom of a cell containing 0.3 M $H_2C_2O_4$, a temperature of 15 °C and 40 V for 6 min.
5. Pore widening. The pores of the template were open in a solution of 0.1 M H_3PO_4 at 30 °C for 5 to10 min.

3.4 Chemical oxidative polymerization of 3HT

P3HT is synthesized by chemical oxidative polymerization of 3-hexylthiophene monomer (3HT) and using anhydrous $FeCl_3$ as oxidant agent.

First, a solution of 4 mmol of $FeCl_3$ in 50 mL of $CHCl_3$ is placed in a three-necked ball flask (as shown in figure 7) and left under stirring for 1 h. After, 1 mmol of 3HT in 10 mL of $CHCl_3$ is added to the main solution drop wise. The mixture is left under stirring for 24 h at room temperature and nitrogen atmosphere. See Figure 9.

Once conclude the time, the nitrogen atmosphere is removed and the product is transferred to an equal amount of methanol and stirred for 5 min, to insolubilize the polymer. After, the solution is filtered, and the filter paper is placed in an oven at 80 ºC for 30 min to recover the polymer.

Finally, the polymer is ground in an agate mortar until getting fine powder for further characterization.

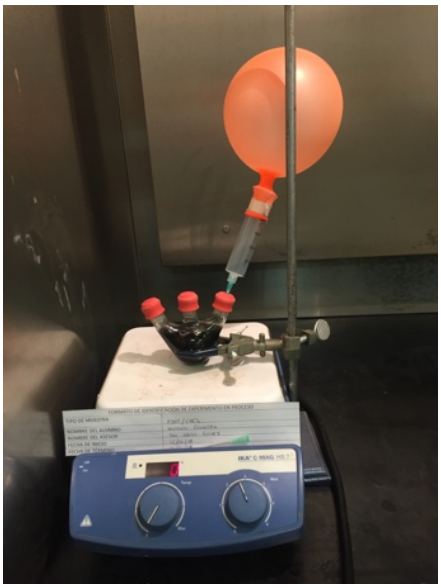

Figure 9. Polymerization reaction of 3HT.

3.5 Synthesis of poly(3-hexylthiophene) at AAO template

P3HT was synthesized by oxidative polymerization of 3-hexylthiophene (3HT) monomer and anhydrous $FeCl_3$ as an oxidant. A solution of 4 mmol $FeCl_3$ in 50 mL chloroform was placed in a 3-necked flask. Solution was stirring for 1 hour, followed by the addition of the monomer (1mmol) in 10 mL of chloroform drop wise. The mixture was kept under continuous magnetic stirring for 24 h at room temperature and nitrogen atmosphere. After these, the solution was transferred into methanol and it was stirred for a couple of minutes. Finally, P3HT was filtered under vacuum.

Once synthesized, a suspension of P3HT in chlorobenzene (3 wt%) was prepared to apply this solution using spin coating at 3500 rpm on the AAO template. Afterward, the alumina and Al substrate were removed by immersing the sample in 3 M NaOH solution for 45 min. The next step was to deposit the P3HT to the ITO glass; for this purpose, the ITO substrate was activated by soaking it in chloroform for 40 min. Figure 10 shows this process.

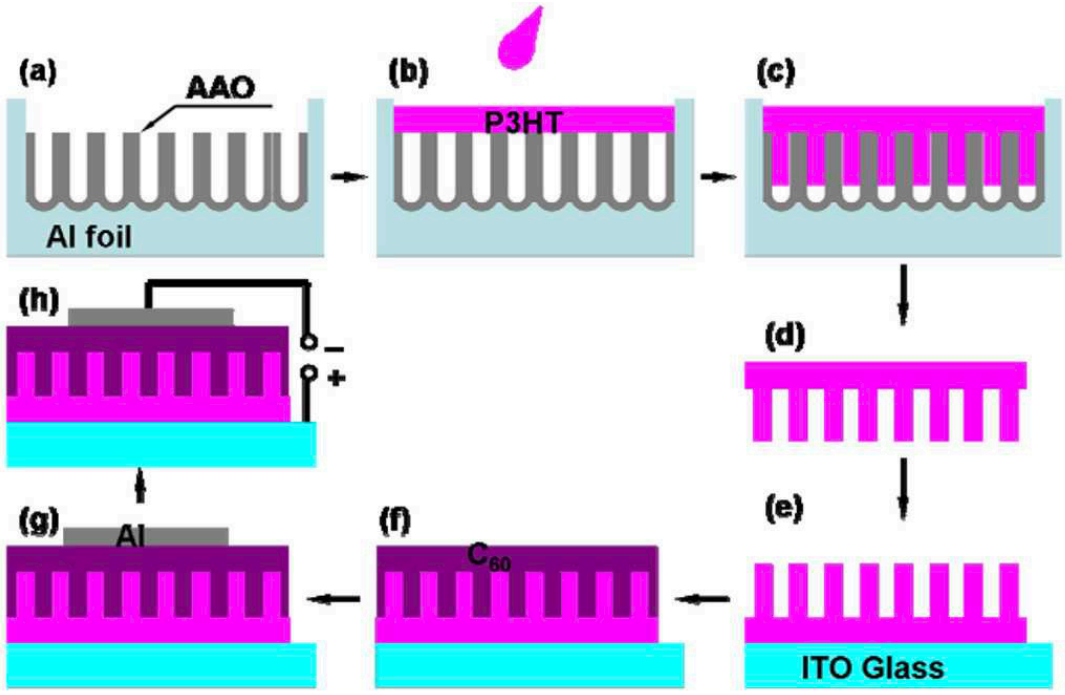

Figure 10. Schematic process of self-standing P3HT nanorods on ITO glass.

3.6 Synthesis of ZnO nanorods

3.6.1 Synthesis of ZnO nanorods at the polymeric template

The composite containing template and polymeric nanorods were immersed in 0.5 M NaOH solution to dissolve the template and release the polymer. Now the pattern polymer was used as a “template” to contain the ZnO nanorods. After this process, ZnO was electrodeposited from a solution containing 0.005 M $Zn(NO_3)_2 \cdot 6H_2O$, at 80°C for 10 min. Electrodeposition has been done in a three-electrode cell in which the counter, reference and working electrodes were Pt wire, Ag/AgCl and AAO template respectively; the applied voltage was -1 V as shown in Figure 11.

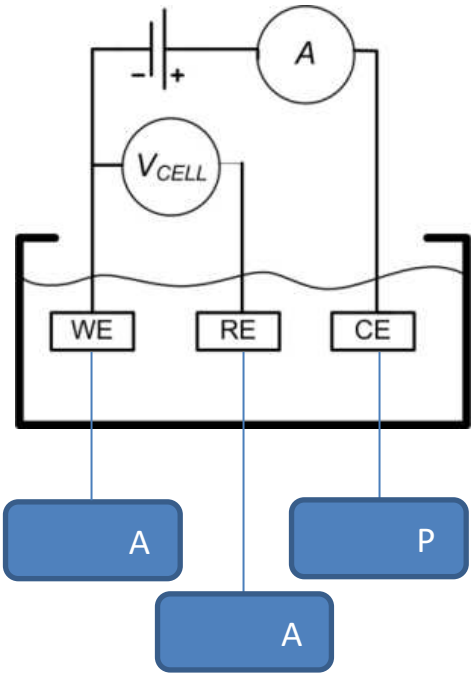

Figure 11. Three electrode cell used for electrodeposition.

3.6.2 Synthesis of ZnO nanorods by hydrothermal route

The hydrothermal synthesis was carried out by the seeds and growth method. For the ZnO seed, a solution of $Zn(CH_3COO)2H_2O$ 50 mM was kept under stirring (300 rpm) and heating (85 ºC) for 20 min. Then 349 µL of triethylamine were added and the solution was maintained at 85 ºC for 15 min.

For the growth solution, 20.8 g of $Zn(NO_3)_26H_2O$ were added to a solution of hexamethylenetetramine 100 mM and it was kept under stirring for 24 h followed by filtering.

The seed solution was spin coated on a substrate and submerged on the growth solution contained inside the hydrothermal reactor. Finally, the reactor was set inside an oven at 80 ºC for 2 h.

3.7 Synthesis of Au nanoparticles

The gold nanoparticles reported in this research were obtained from $HAuCl_4$, using sodium citrate, that act as a reducing and stabilizing agent. These nanoparticles were synthesized by thermal and microwave heating methods to compare the difference of the size and plasmon signal obtained by both methods. The details of the syntheses are presented below.

3.7.1 Thermal heating method

1 mL of 25 mM $HAuCl_4$ solution was taken and diluted up to 100 mL. This solution was kept under string and heating until boiling. Afterward, 5 mL of 1 wt% sodium citrate were added; the solution, originally yellow, turned colorless and finally changed to a red wine color. Solution was heated up to boiling for 30 min and finally was diluted up to 100 mL to compensate the evaporation losses. See Figure 12.

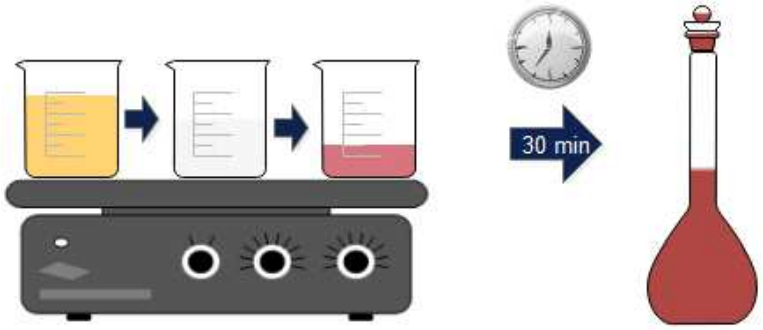

Figure 12. Gold nanoparticles synthesis by conventional heating method.

3.7.2 Microwave method

For the microwave synthesis, 1 mL of 5 mM $HAuCl_4$ and 1 mL of 25 mM sodium citrate were dissolved in 18 mL of H_2O. This solution was placed into a conventional microwave oven Whirlpool® model WM1207D, for 10 min at a power of 1275W to 20%. See Figure 13.

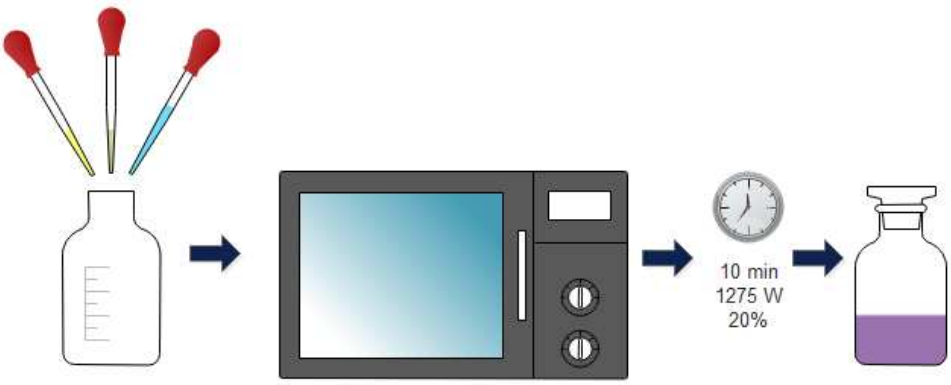

Figure 13. Gold nanoparticles synthesis by microwave method.

To study the effect on the size and plasmonic signal, two variables were studied in this method: cycles and sonication time. Cycles were varied in 0 min, 5

min and 10 min, while the sonication time was varied in 10 min,15 min and 20 min.

3.7.3 Synthesis of gold nanorods

Gold nanorods were synthesized using a seedless growth method to incorporate them at the active layer to observe its contribution compared to Au nanoparticles.

The growth solution was prepared at 25−30 °C, by mixing $HAuCl_4$ solution (5.0 mL, 1.0 mM) and 5.0 mL of 0.2 M CTAB solution. Following this, a solution of $AgNO_3$ (250 µL, 4.0 mM) was added, and was also gently shaken. In order to adjust pH around 1, an HCl solution (8.0 µL, 37%) was introduced. Then, 70 µL of ascorbic acid (78.8 mM) were added to the solution with gentle shaking until the solution was clear. Immediately afterward, ice-cold $NaBH_4$ solution (15 µL, 0.01 M) was injected to the unstirred growth solution and allowed to react for 6 h.

Five different synthesis were done in by modifying the amount of reagents to obtain nanorods of different aspect ratio. Table 2 shows these different syntheses.

Table 2. Different synthesis for gold nanorods.

Reagent	**S1**	**S2**	**S3**	**S4**	**S5**
$HAuCl_4$	5 mL	5 mL	5 mL	*2.5 mL*	5 mL
CTAB	5 mL	5 mL	5 mL	5 mL	*10 mL*
$AgNO_3$	250 µL	*270 µL*	*290 µL*	250 µL	250 µL
HCl	8 µL	8 µL	8 µL	8 µL	8 µL
$NaBH_4$	15 µL	15 µL	15 µL	*7.5 µL*	15 µL
$C_6H_8O_6$	70 µL	70 µL	70 µL	*35 µL*	70 µL

According to literature, the different aspect ratios are as follow: S1 – 18 nm x 4.5 nm, S2 – 25 nm x 5 nm, S3 – 27 nm x 5.5 nm, S4 – 10.5 nm x 2.8 nm, S5 – 14 nm x 4.2 nm [166].

3.8 Incorporation of gold nanoparticles to the polymeric template with ZnO nanorods

Gold nanoparticles were deposited on the surface of ZnO/P3HT nanorods by electrophoretic deposition to synthesize the active layer.

Electrophoretic deposition was held at 4 V for 1 min with a working electrode of the hybrid active layer synthesized (ZnO/P3HT/ITO) and a counter electrode of ITO, with a separation distance of 1 cm.

3.9 Active layer assembly

Two types of configurations can be found in a hybrid solar cell: conventional and inverted. In a conventional cell, the transparent conductive oxide glass (positive electrode) is in direct contact with organic semiconductor, whereupon holes travel through this, and electrons in opposite direction. In an inverted solar cell, the transparent conductive oxide glass (negative electrode) is cover with a thin film of inorganic semiconductor, causing electrons to travel through it and holes in opposite direction [47, 73, 163].

In this studio, two configurations were tested to establish the best performance and influence of the arrangement and nanoform of semiconductor type p (P3HT). First device (D1): ITO/ZnO/P3HT/Au and the second device (D2): ITO/P3HT/ZnO/Au.

For the first device (D1), ITO glass was previously activated in aqua regia to increase its affinity for ZnO. After, ZnO was electrodeposited from a solution containing $Zn(NO_3)_2 \cdot 6H_2O$ 0.005M, at 80°C for 10 min. Electrodeposition was done in a three-electrode cell in which the counter, reference and working electrodes were Pt wire, Ag/AgCl and ITO glass respectively; the applied voltage was -1 V. Once the ZnO NR were obtained, P3HT was suspended in chlorobenzene (5 mg/mL) and deposited on the substrate by spin-coating method; by capillary forces, the polymer fills the cavities of the ZnO NR film. Finally, the gold nanoparticles were added by electrophoretic deposition.

For the second device (D2), ITO glass was previously activated submerging it in $CHCl_3$ to increase its affinity for P3HT. To obtained P3HT NR, template assisted method was carried out. Anodic aluminum oxide (AAO) template, was obtained for the well-known two steps method [167]. After, P3HT (5 mg/mL in chlorobenzene) was spin-coated on it and by capillary forces, the polymer filled the channels of the AAO template. Later, AAO template was dissolved in a solution of NaOH 3M, leaving a “floating” polymer thin film which is adhered to ITO glass putting it in contact from the back side of the film to let the NR facing up. After this, ZnO NR are formed in the ITO/P3HT substrate by the electrochemical method already described. Finally, the gold nanoparticles were added by electrophoretic deposition.

3.10 Characterization

For measuring the thickness of the aluminum film, a profilometer KLA Tencor D-100 was used. This equipment is located at Materials Laboratory I, FCQ UANL.

To observe the structure formed in the first anodization, micrographs of aluminum films were taken in a field emission scanning electron microscope model Nova NanoSEM 200 FEI at CIMAV Monterrey.

To ensure the formation of metal nanoparticles, the localized surface plasmon resonance (LSPR) of the synthesized particles was analyzed in a

spectrophotometer UV-Vis. Analysis was done in a UV Spectrophotometer Shimadzu UV-1800 located at Laboratory of Materials I, FCQ UANL.

The metal nanoparticles morphology and size were observed by SEM JEOL JSM6701F located in LACMIMAV, FCQ UANL.

Particle size distribution of Au nanoparticles was measured in a Microtrac Zetatrac equipment located at the Laboratory of Materials I FCQ, UANL.

For quantitative information on the nanostructure of the active layer and to observe the morphology and grain size, an atomic force microscopy (AFM) analysis was carried out. Analysis was performed in a Scanning Probe Microscope AA3000 placed at the Laboratory of Materials I FCQ, UANL.

Energy bandgap of the active layer was calculated by the transmittance spectrum, for this purpose a spectrophotometer UV-Vis was used.

Finally, a solar simulator was used to measure the current-voltage curves of the solar cells.

4. RESULTS AND DISCUSSIONS

4.1 Fabrication of the template

4.1.1 Sputter Deposition

Different conditions have been proved to achieve the 2 μm of pure aluminum film that was required for the two-anodization process. Table 3 shows a summary of the tested conditions in 22 samples.

Table 3. Sputtering conditions vs profilometry measurements.

Sample	Power (W)	Argon flux (SCCM)	Distance (cm)	Deposition time (min)	Vacuum (Torr)	Thickness (nm)
1	100	60	10	15	1.5×10^{-4}	No
2	100	60	10	3	1.5×10^{-4}	40
3	100	60	10	15	1.5×10^{-4}	240
4	110/120	60	10	15	1.5×10^{-4}	Low
5	100	60	10	45	1.5×10^{-4}	680
6	100	60	10	90	1.5×10^{-4}	600
7	100	20	4	30	1.5×10^{-4}	500
8	100	30	4	30	1.5×10^{-4}	653
9	120	20	4	30	1.5×10^{-4}	600
10	140	20	4	30	2.5×10^{-5}	677
11	140	20	4	30	1.5×10^{-5}	517
12	120	40	6	30	1.5×10^{-5}	340
13	120	40	6	60	1.5×10^{-5}	543
14	120	40	6	90	1.5×10^{-5}	840
15	120	30	4	60	1.5×10^{-5}	490
16	120	30	4	90	1.5×10^{-5}	790
17	150	30	4	60	1.5×10^{-5}	660
18	150	30	4	90	1.5×10^{-5}	920
19	150	40	4	60	1.5×10^{-5}	680
20	150	40	4	60	1.5×10^{-5}	1100
21	150	40	4	90	1.5×10^{-5}	1150
22	200	40	4	120	2.0×10^{-3}	2000

*Note: [1]The parameter “distance” indicates the separation between the magnetron and the sample. [2]SCCM: standard cubic centimeters per minute.

In the first conditions tested, sample 1, no deposit was obtained, this could be due since the sputtering must be assisted by radiofrequency to achieve the erosion of the aluminum target, for this reason radiofrequency was used in the rest of the samples.

In samples 2 and 3, a power of 100 W was applied in relatively short times (3 and 15 min) and, therefore, poor deposits were obtained. Increasing the power and maintaining a high Ar flux (60 SCCM) resulted in Al film of low adherence, because a higher power increased the excitation of argon ions, being necessary to control its flux to achieve a uniform deposit, as can be observe in sample 4.

Samples 5 and 6 were tested under the same conditions at 45 and 90 min respectively, with the difference that in sample 6, two cycles of 45 min were performed. As a result, the film thickness of sample 5 increased, nevertheless, sample 6 was subjected for a longer time, a lower and non-conducting deposit was obtained. An XRD analysis revealed that aluminum oxide was formed on the surface of the film because the vacuum was removed from the chamber in the middle of the two cycles, forming a non-homogeneous surface for later deposits.

In the experiments 7 to 11, the samples were approached to the magnetron, the argon flux was reduced, and the power was varied. However, the deposits tend to be “sandy”, of low adherence and non-uniform because of the proximity to the target.

In samples 12 to 14 the magnetron was moved away from the sample, the argon flux and power were set to 40 SCCM and 120 W respectively, and it can be

seen how the thickness increased over time, however, the maximum result is far from expected.

The erosive gas flow was reduced to 30 SCCM in samples 15 to 18 because, sometimes, a high flow of erosive gas tends to reduce the rate of deposit. Samples 17 and 18 were compared to samples 19 and 20, both pairs were treated under the same conditions but increasing the argon flux in the last two; the results showed that under 150 W, a high argon flux increased the thickness of the film.

Sample 21 was placed inside the chamber after 30 min of eroding the target, this with the aim of eliminating any residual oxide and increase deposit rate, therefore, the results showed only a slight increase.

Finally, the power was adjusted to 200 W, the vacuum was increased to 2 mTorr, the argon flux and distance of the magnetron were maintained at 40 SCCM and 4 cm, respectively; a thin film of 2000 nm was obtained within 2 h (sample 22).

Figure 14 shows a SEM image of the Al film deposited by sputtering on ITO glass. It can be observed that, despite of being a homogenous deposit, presents lots of structural defects that prevents the formation of an AAO template of high order.

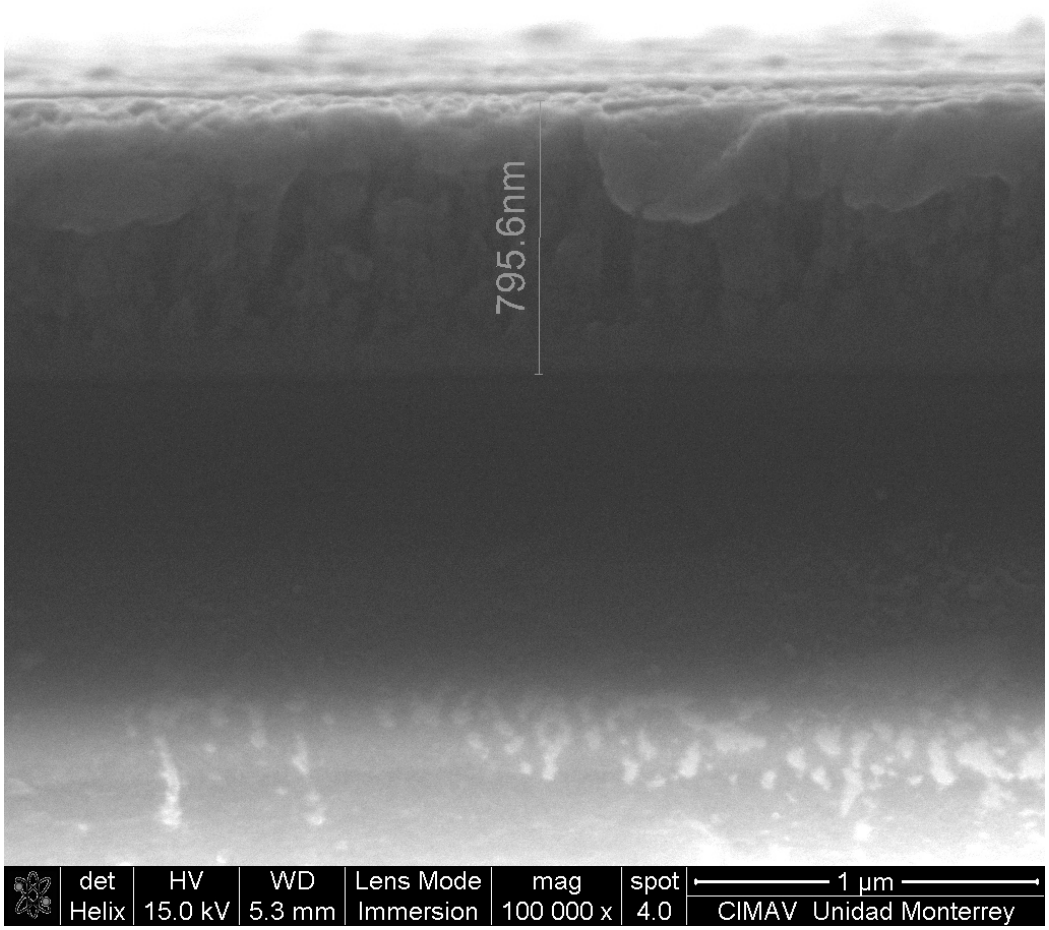

Figure 14. Al film on ITO glass by sputtering deposition.

4.1.2 Atomic Force Microscopy

Aluminum thin film of sample 7 was analyzed by AFM, micrographs showed a homogenous deposit with a grain size of approximately 500 nm as can be observed in Figure 15.

Sample 8 was deposited under the same conditions as the sample 7, but with a different argon flux of 30 SCCM and 20 SCCM, respectively. AFM micrographs show a more homogeneous deposit with a grain size of

approximately 100 nm (Figure 16). With an increase of 10 SCCM of argon flux, the thickness of the film is increased in 150 nm and the grain size is reduced in, approximately, 400 nm. Having a greater erosive gas flow, a greater quantity of aluminum ions can be detached from the target and in consequence the thickness of the deposit is increased. A low argon flux will allow the possibility to form larger grain size due to less interference of kick-off ions.

Table 4 shows the conditions utilized for the deposits of aluminum in samples 7 and 8.

Table 4. Comparing the sputtering conditions of sample 7 and 8.

Sample	7	8
Power	100 W	100 W
Argon flux	20 SCCM	30 SCCM
Distance of magnetron	4 cm	4 cm
Deposition time	30 min	30 min
Vacuum	1.5×10^{-5} Torr	1.5×10^{-5} Torr
Thickness	500 nm	653 nm

Sample 7

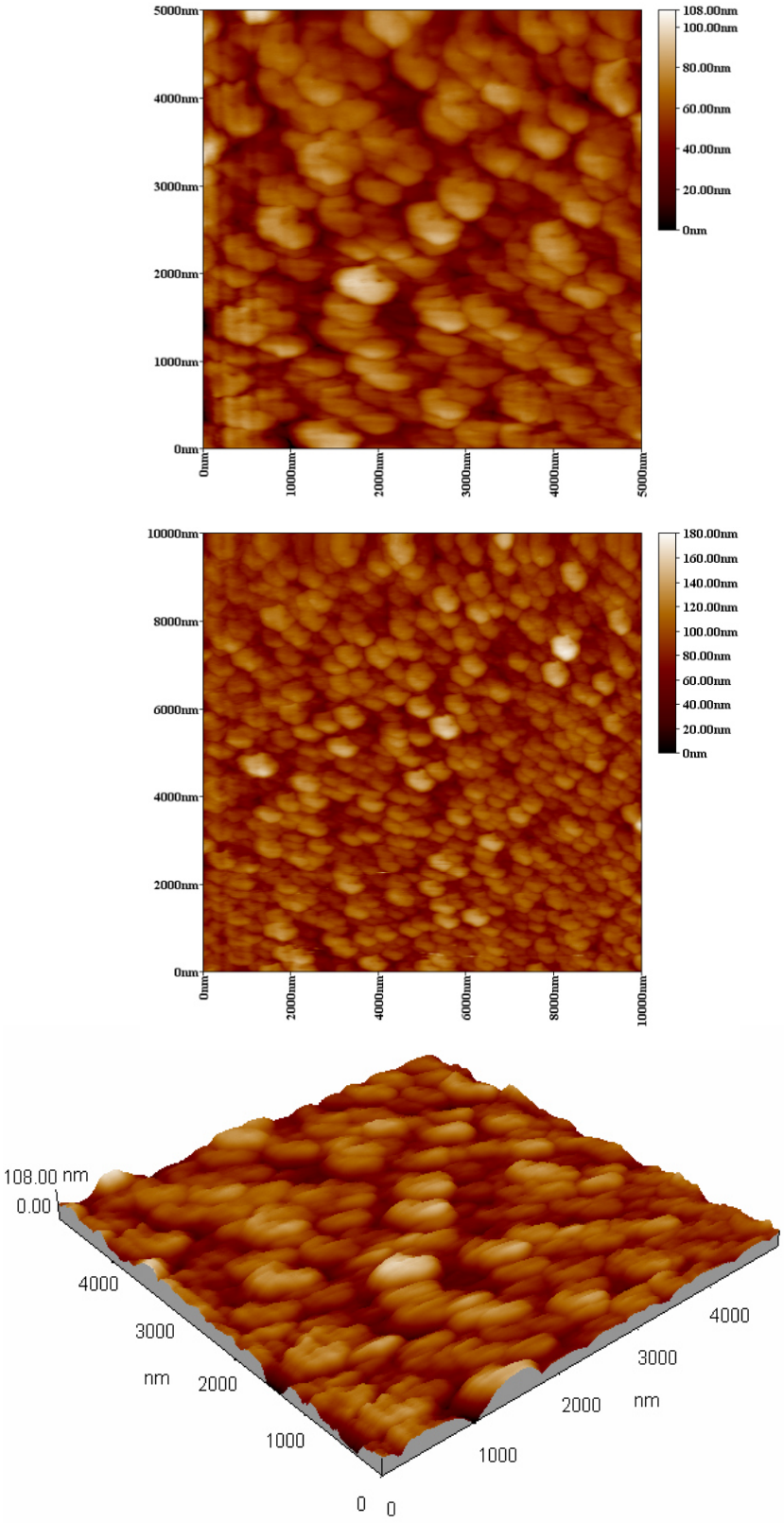

Figure 15. AFM images of aluminum film obtained at 20 SCCM of argon flux.

Sample 8

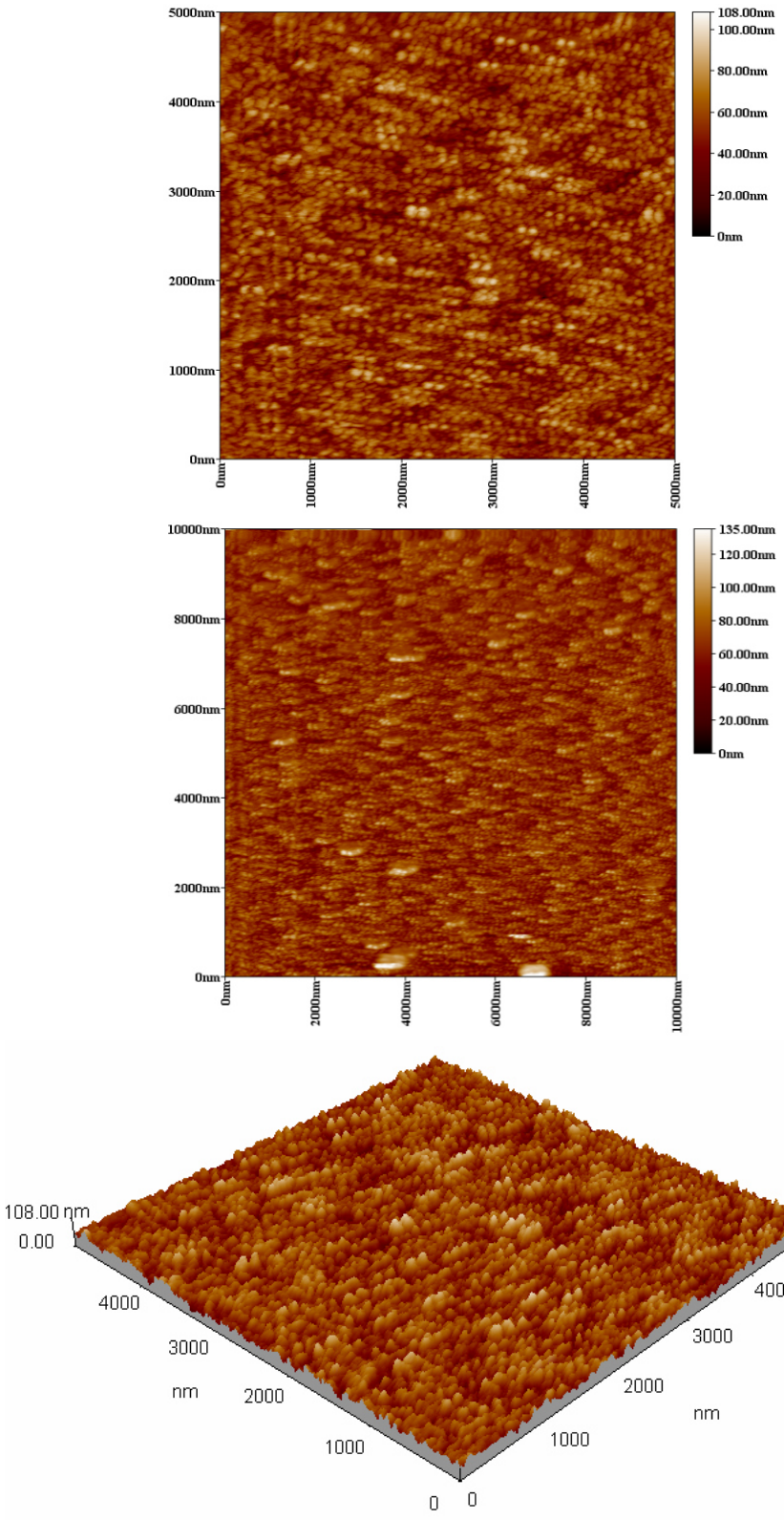

Figure 16. AFM images of aluminum film obtained at 30 SCCM of argon flux.

4.2 First anodization

4.2.1 Scanning Electron Microscopy

Different conditions were tested to find the adequate for the first anodization. SEM microscopies were obtained from each sample.

Figure 17 shows the first anodization under configuration “b” and it can be observed how defined grains begin to form a pattern. The same conditions were test but under configuration “a”, and it can be observed how the pattern is lost and the grain limits are not defined any more as can be observed in Figure 18. Configuration “a” does not maintain a constant distance between the electrodes, therefore the reaction is incomplete.

Anodizing conditions:

- Voltage: 40 V
- Time: 30 min
- Thickness: 680 nm
- Configuration: b

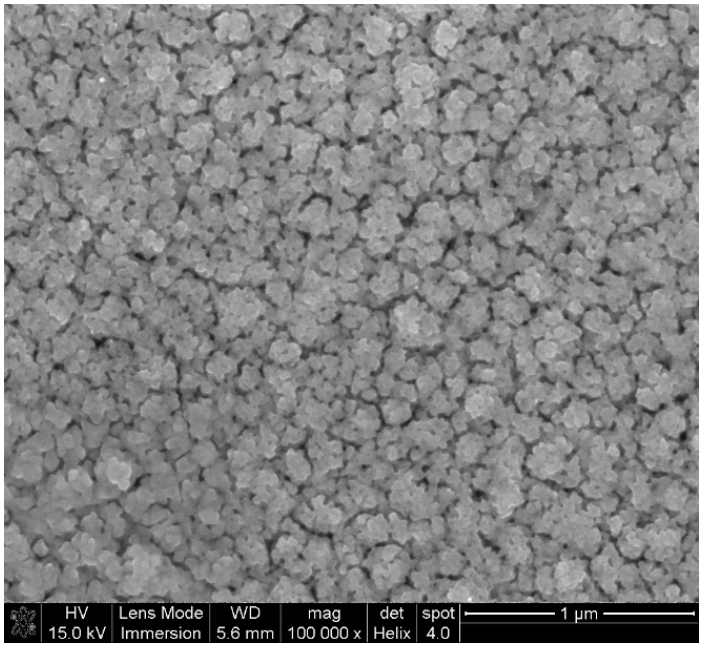

Figure 17. SEM image of first anodization under configuration b.

Anodizing conditions:

- Voltage: 40 V
- Time: 30 min
- Thickness: 680 nm
- Configuration: a

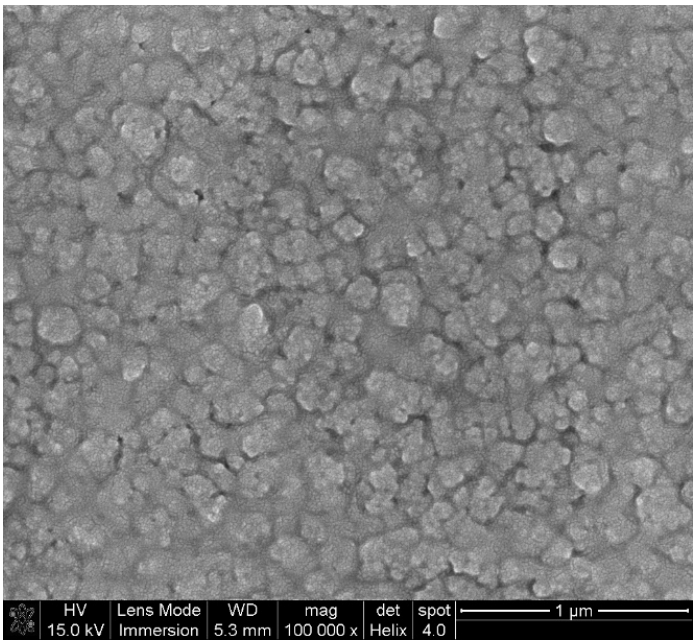

Figure 18. SEM images of first anodization under configuration “a”.

When the time of the first anodization was increased to 40 min, the template channels begin to form as shown in Figure 19.

- Voltage: 40 V
- Time: 40 min
- Thickness: 680 nm
- Configuration: b

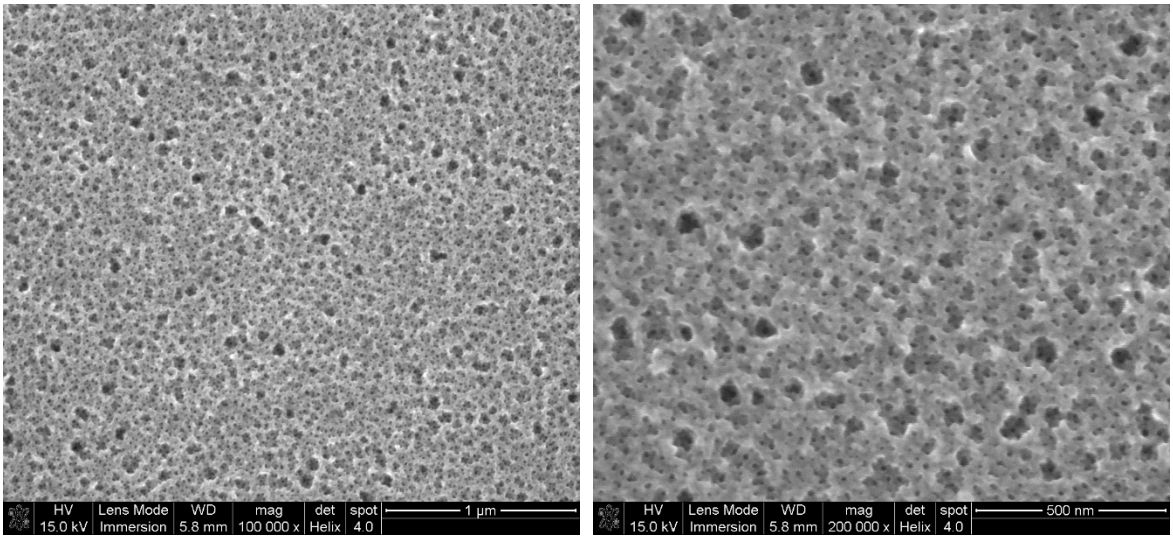

Figure 19. SEM images of first anodization for 40 min. Amplification of 100,000 x (left) and 200,000 x (right).

Increasing the anodization time to 45 min an aluminum film, with some fractures, was obtained. Leading the 40 min, as the ideal anodization time (Figure 20).

- Voltage: 40 V
- Time: 45 min
- Thickness: 680 nm
- Configuration: b

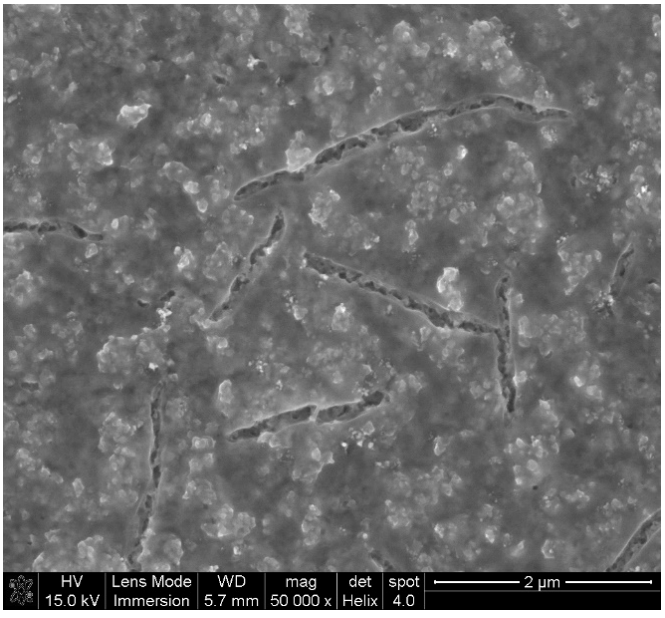

Figure 20. SEM image of first anodization for 45 min.

The objective of first anodization was to form the pattern of channels that will help as guide for the aligned channels to be formed in the second anodization.

4.3 Electron beam

Aluminum film was also deposited by electron beam technique with the objective to observe if it was possible to obtain AAO templates of better quality. In Figure 21 it can be observed a pattern with higher order that the obtained in aluminum thin film by sputtering, however the deposit is not homogeneous.

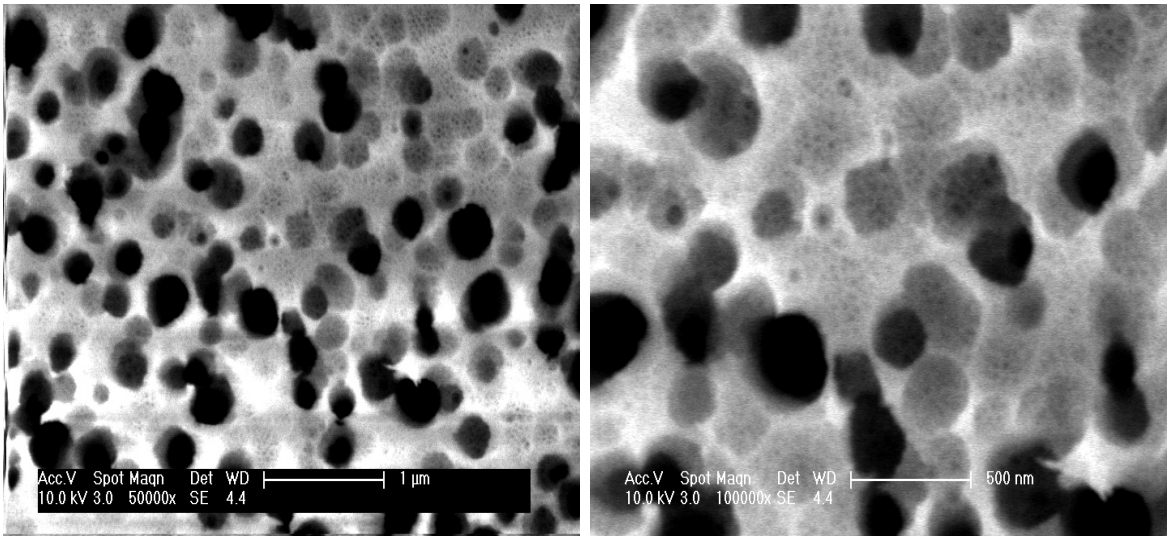

Figure 21. AAO template of aluminum on ITO deposited by electron beam.

4.4 High purity aluminum

Due to the low quality of the AAO templates obtained by sputtering and electron beam, it was decided to work with high purity aluminum. Figure 22 shows

SEM images of the template obtained by the method of two anodizations, described in the previous section (page 37). High quality AAO template was obtained with a porous diameter of 100 nm approximately.

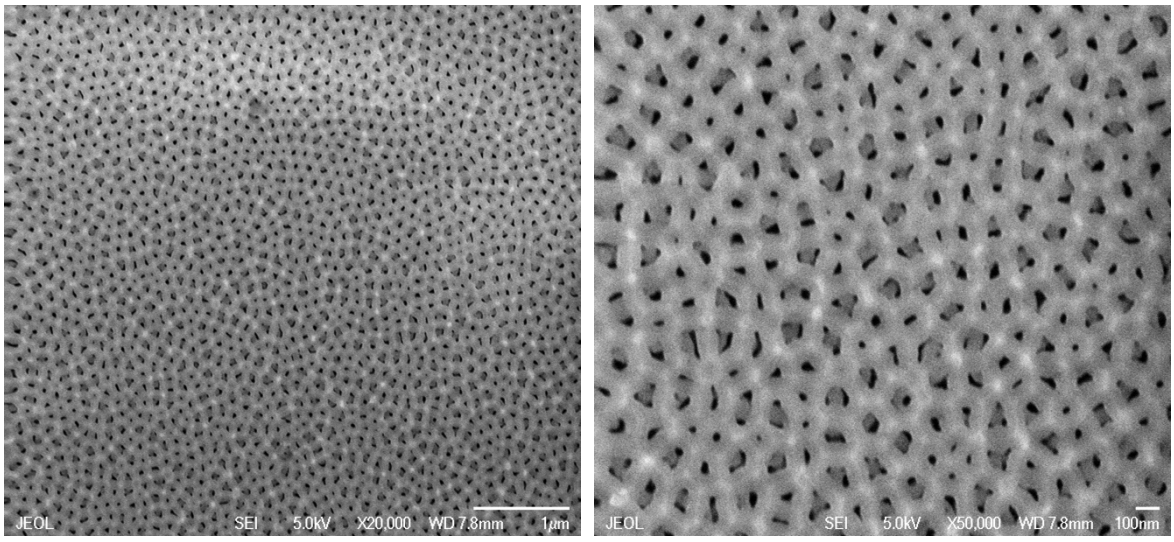

Figure 22. AAO template on high purity aluminum.

4.5 Low purity aluminum (1100) anodization for 2 h

An AAO template was also fabricated in low purity aluminum. In Figure 23 it is shown the template obtained, in which it can be observed that a pattern is formed, not as ordered as the high purity, but it is presented as an alternative of low-cost template.

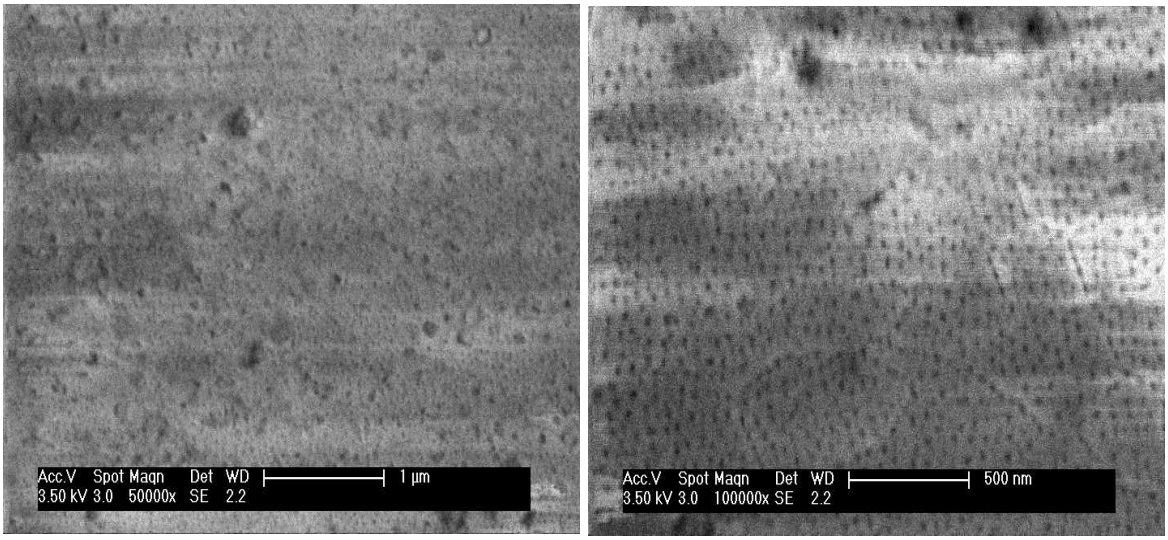

Figure 23. AAO in low purity aluminum.

4.6 Poly(3-hexylthiophene)

4.6.1 UV-Vis spectrophotometry

Polymer was characterized, in different concentrations, by spectrophotometry UV-Vis. As can be observed in Figure 24, the two characteristic band are shown in the spectra. First band, around 450 nm, is associated to the $\pi - \pi^*$ transitions of the conjugated segments between the adjacent rings caused by moving an electron from a bonding π orbital to an antibonding π^* orbital. Second band, around 260 nm, is associated with the movement of an electron from a nonbonding electron pair to an orbital π^*.

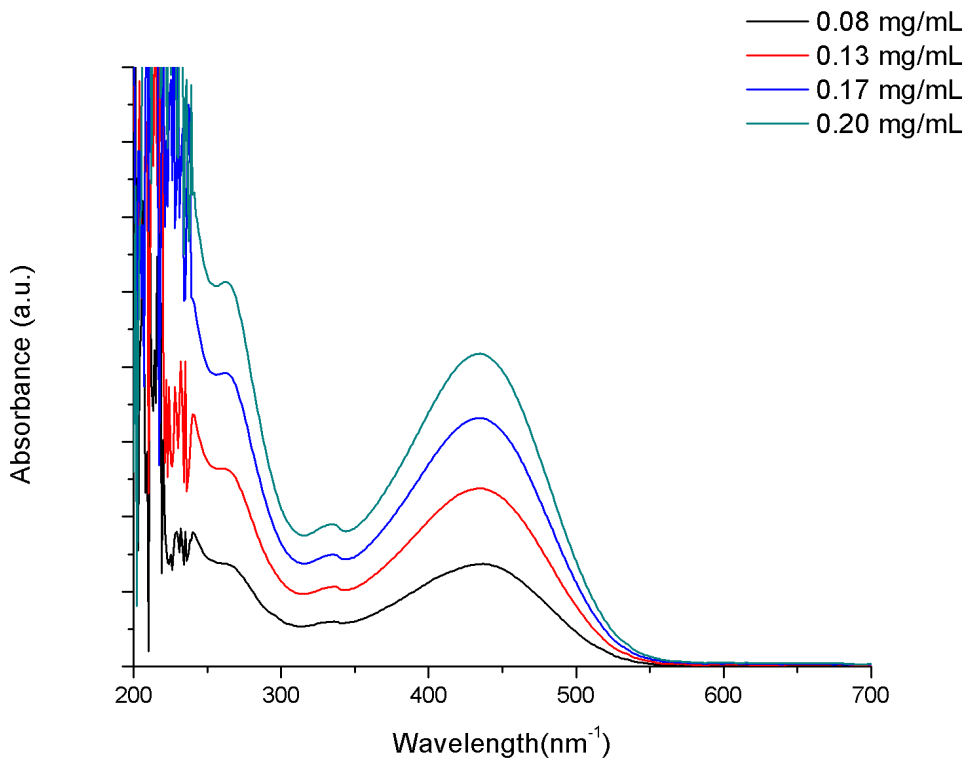

Figure 24. UV-vis spectrum of P3HT at different concentrations.

4.6.2 Bandgap calculation

An approximation of the energy bandgap was made using Tauc's plot using n=1/2, corresponding to allow direct transition. As can be observed in Figure 25, a bandgap value of, approximately, 1.8 eV was obtained for the synthesized polymer. This result is in good agreement with literature [168, 169].

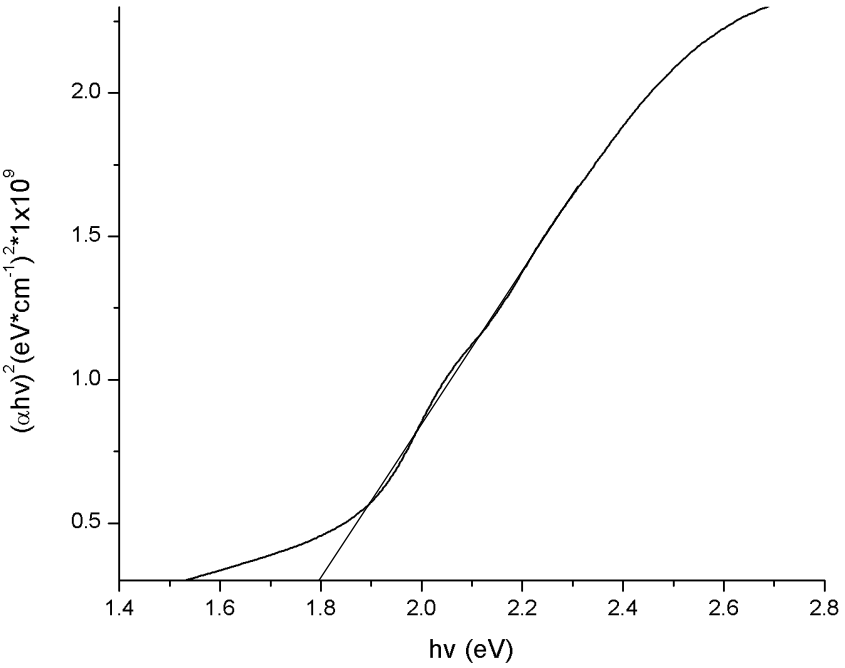

Figure 25. Tauc's plot of P3HT.

4.6.3 Fourier transformed infrared spectroscopy

Polymer was also characterized by FTIR. In Figure 26, it can be detected the four characteristic signals of the P3HT, according to literature [169, 170]. Band "A" is associated to vibrations in the aliphatic chain of hexyl groups. In band "B" the presence of thiophene ring is confirmed. Band "C" is associated to the presence of C-H of the aromatic ring. Finally, band "D" is related to bending of link C-S. These signals are summarized in Table 5.

Table 5. FTIR band assignment.

Band	Position (cm^{-1})	Assignment
A	~2918 y 2849	Stretching C-H chain
B	~ 1458	Stretching C=C
C	~ 1121	Stretching C-H ring
D	~ 820	Bending C-S

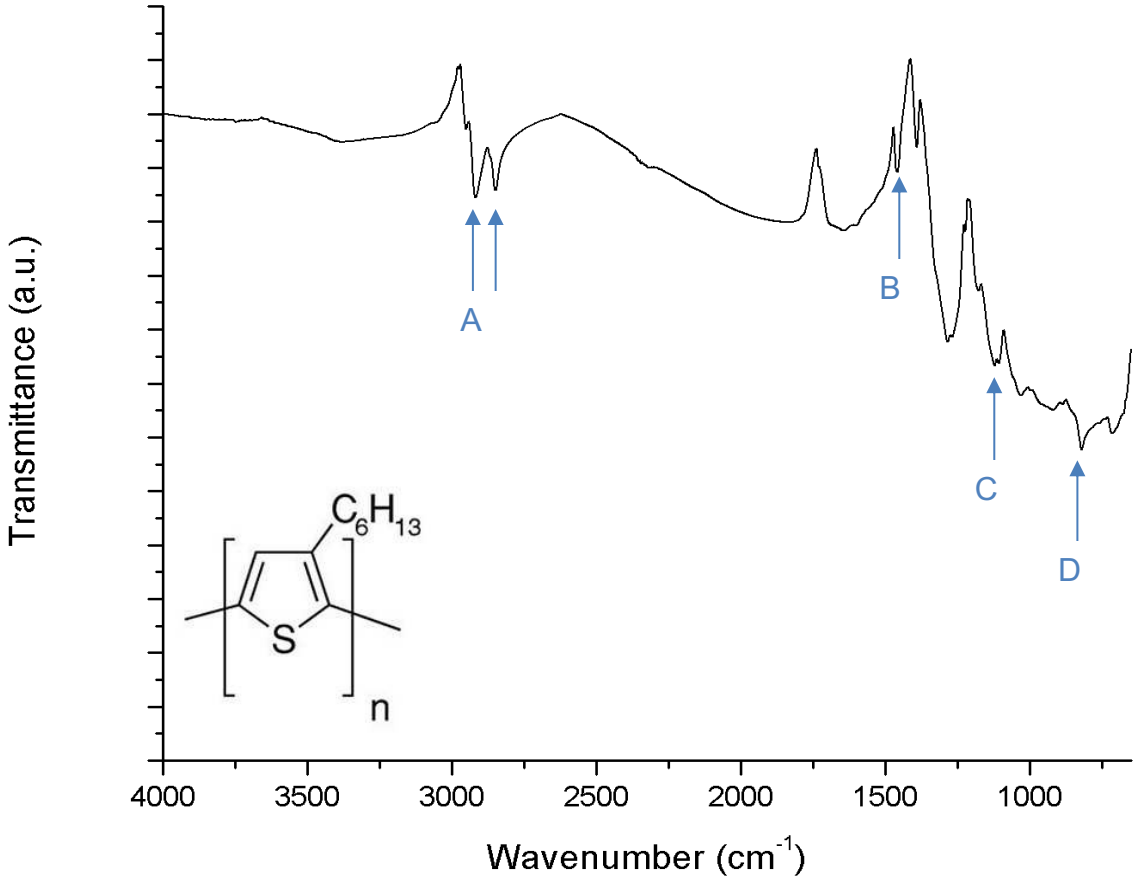

Figure 26. FTIR spectrum of P3HT.

4.6.4 P3HT nanorods in AAO template

AAO was spin coated at 3500 rpm with P3HT suspended in chlorobenzene (1 wt%). By capillary forces, the polymer achieved to enter the pores of the template. In Figure 27, can be seen how effectively some of the pores were filled with the polymer.

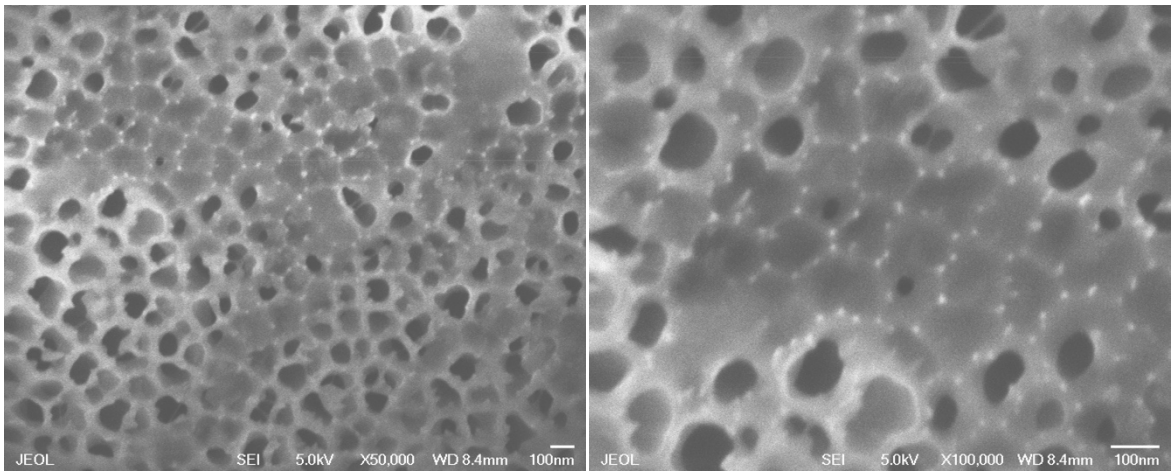

Figure 27. Surface electron microscopy of P3HT inside the pores of AAO template.

To adhere the thin film of polymer nanorods to ITO glass, the methodology described in section 3 was carried out. Figure 28 shows this process. In (a), the polymer thin film was on AAO template, which is being dissolved in NaOH 0.05 M. Image (b) shows the thin film suspended in the solution, after the template was completely dissolved. Finally, in image (c) can be observed the thin film already adhered to the substrate.

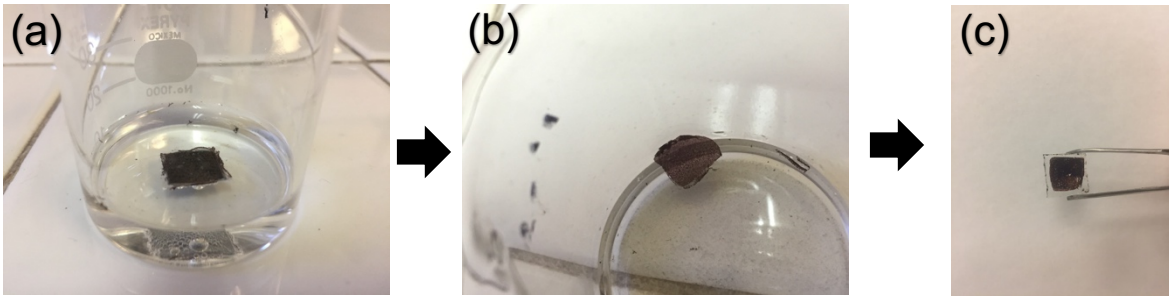

Figure 28. Methodology for obtaining the thin film of polymer nanorods on ITO glass. (a) AAO in NaOH 0.05, (b) P3HT in NaOH 0.05 M and (c) P3HT on ITO glass.

4.7 ZnO nanords by hydrothermal route

ZnO nanorods were obtained by seed and growth method. Figure 29 shows an AFM micrograph of these nanorods; however, they have a size of approximately 200 nm that represented a problem for their incorporation into the template.

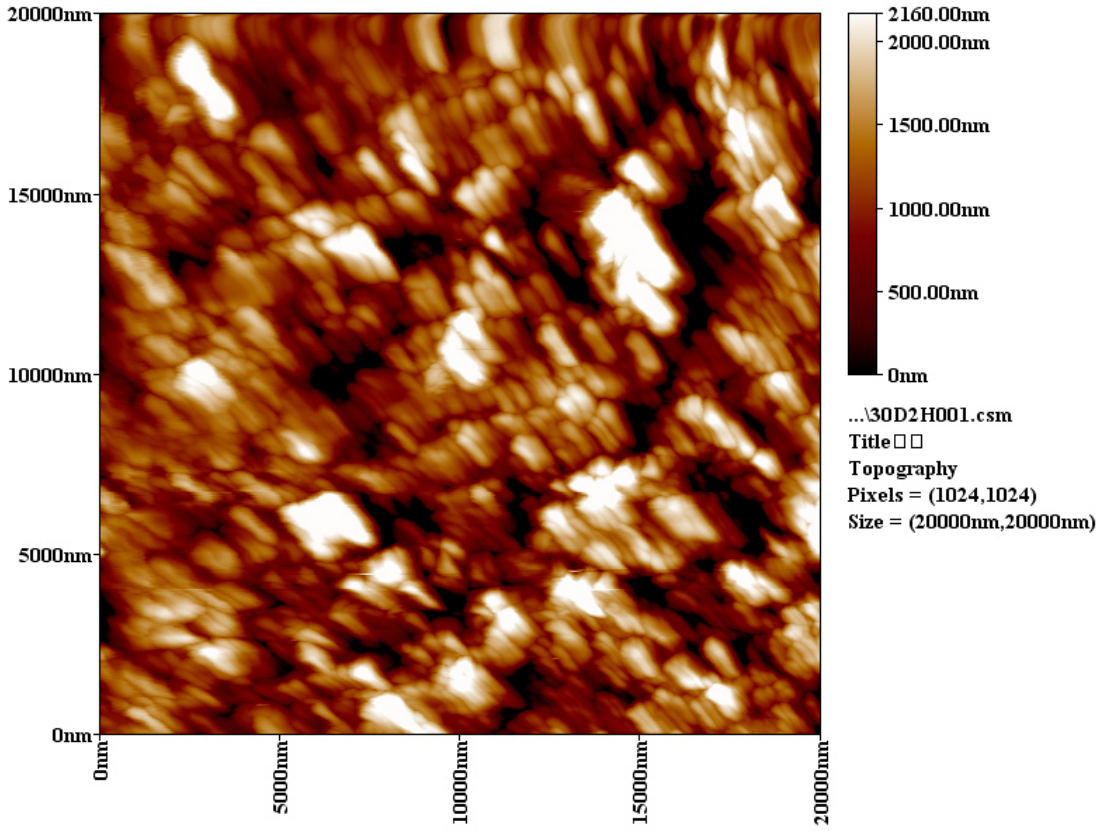

Figure 29. AFM micrography of ZnO nanorods obtained by hydrothermal route.

4.8 ZnO nanorods by electrochemical route

4.8.1 SEM

Two conditions were tested for the electrochemical synthesis of ZnO nanorods. Synthesis was made in a three-electrode cell. In the first reaction, $Zn(NO_3)_2 \cdot 6H_2O$ 0.005 M was used as precursor, a voltage of 1 V vs Ag/AgCl was applied for 10 min at a temperature of 70 ºC. Figure 30 shows the SEM micrographs of the ZnO nanorods obtained. These nanorods have a hexagonal shape of approximately 100 nm of diameter. However, the hexagonal shape, is not completely defined and some “needles” are still observed.

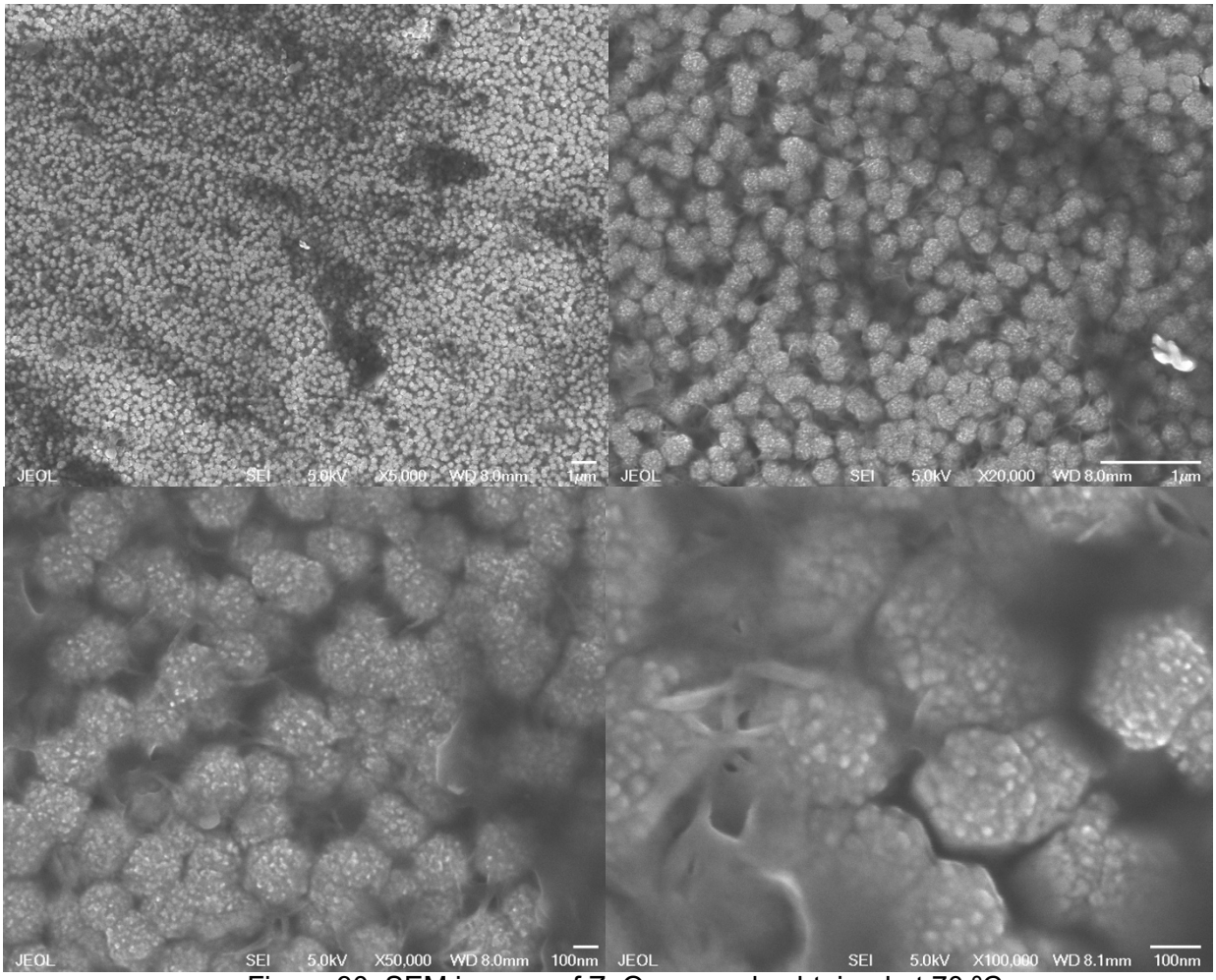

Figure 30. SEM images of ZnO nanorods obtained at 70 ºC.

According to previous results, it was decided to increase the reaction temperature up to 80 ºC with the aim to obtain defined faces of these hexagonal nanorods. Figure 31 shows the micrographs of the nanorods obtained. It can be observed how the faces of the hexagonal nanorods are now defined and even the body of this shape can be noticed.

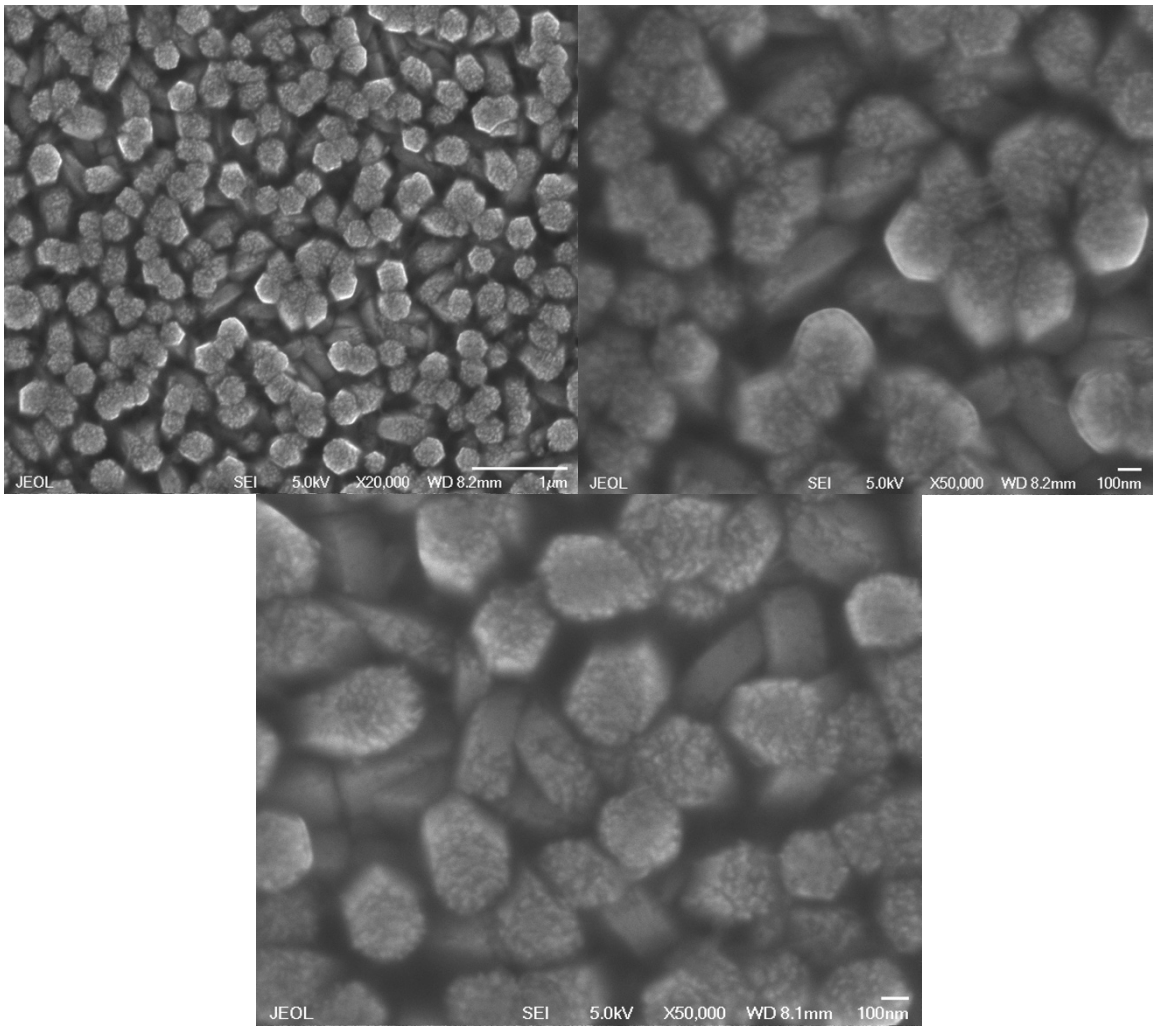

Figure 31. SEM images of ZnO nanorods obtained at 80 ºC.

4.9 Synthesis of gold nanoparticles

The synthesized gold nanoparticles were characterized by UV-Vis spectrophotometry and dynamic light scattering to observe its characteristic plasmon signal and size distribution, respectively.

4.9.1 Dynamic light scattering

4.9.1.1 Thermal heating method

Gold nanoparticles obtained under conventional heating method, have a size between 5 and 10 nm showing narrow size distribution as can be observed in Figure 32.

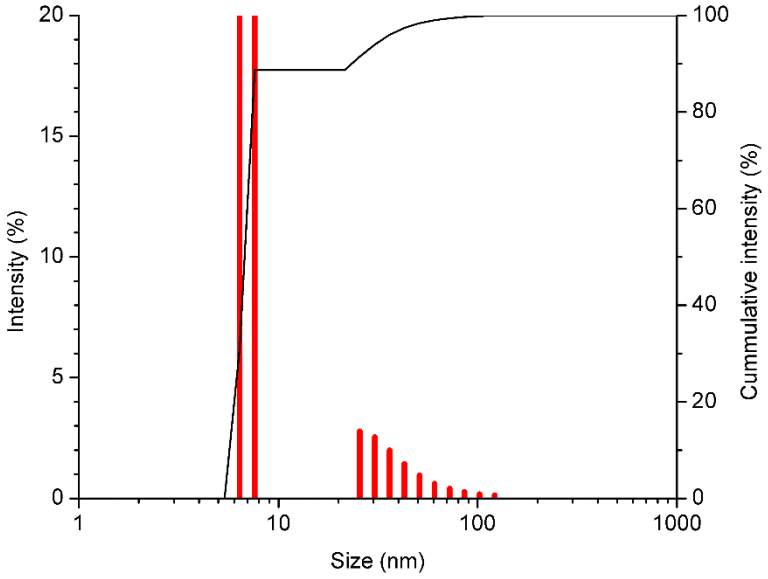

Figure 32. DLS analysis of gold NP obtained by conventional heating method.

4.9.1.2 Microwave method

4.9.1.2.1 Without cycles

In microwave synthesis for 10 min without cycles, sonication times were varied in 10 (WC-10), 15 (WC-15) and 20 min (WC-20). According to the results, increasing the sonication time, resulted in the reduction of the size and size distribution of the nanoparticles. See Figure 33.

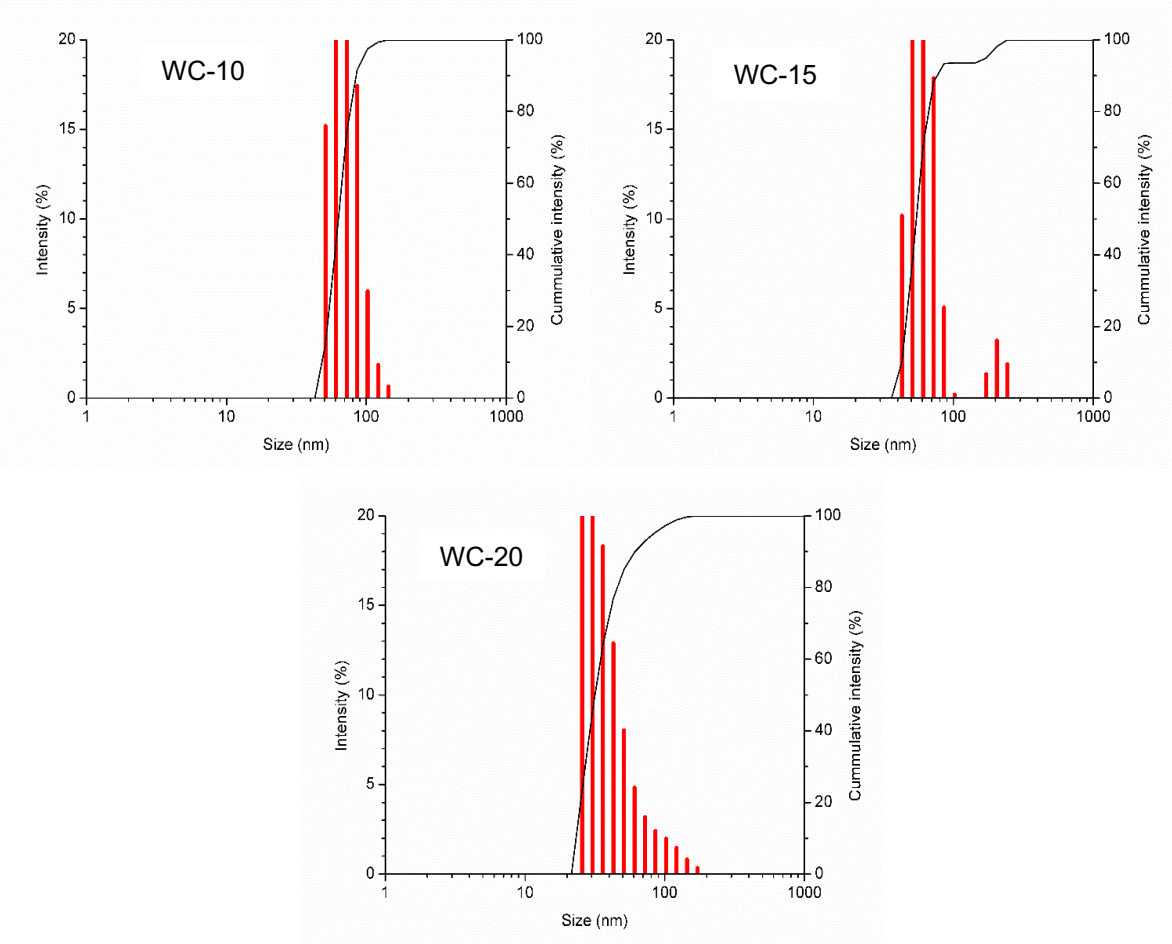

Figure 33. DLS analysis of gold nanoparticles synthesized by microwave without cycles.

4.9.1.2.2 5 cycles

In the synthesis for 10 min with 5 cycles (2 min on, 30 secs off), sonication times were also varied in 10 min (5C-10), 15 min (5C-15) and 20 min (5C-20), respectively. Once again, it can be observed how the increase in sonication time, reduced the size and size distribution of the nanoparticle. However, the size distribution is larger than the other synthesis without cycles, this could be due because, keeping a uniform heating temperature, was a critical parameter to achieve a narrow size distribution [171]. See Figure 34.

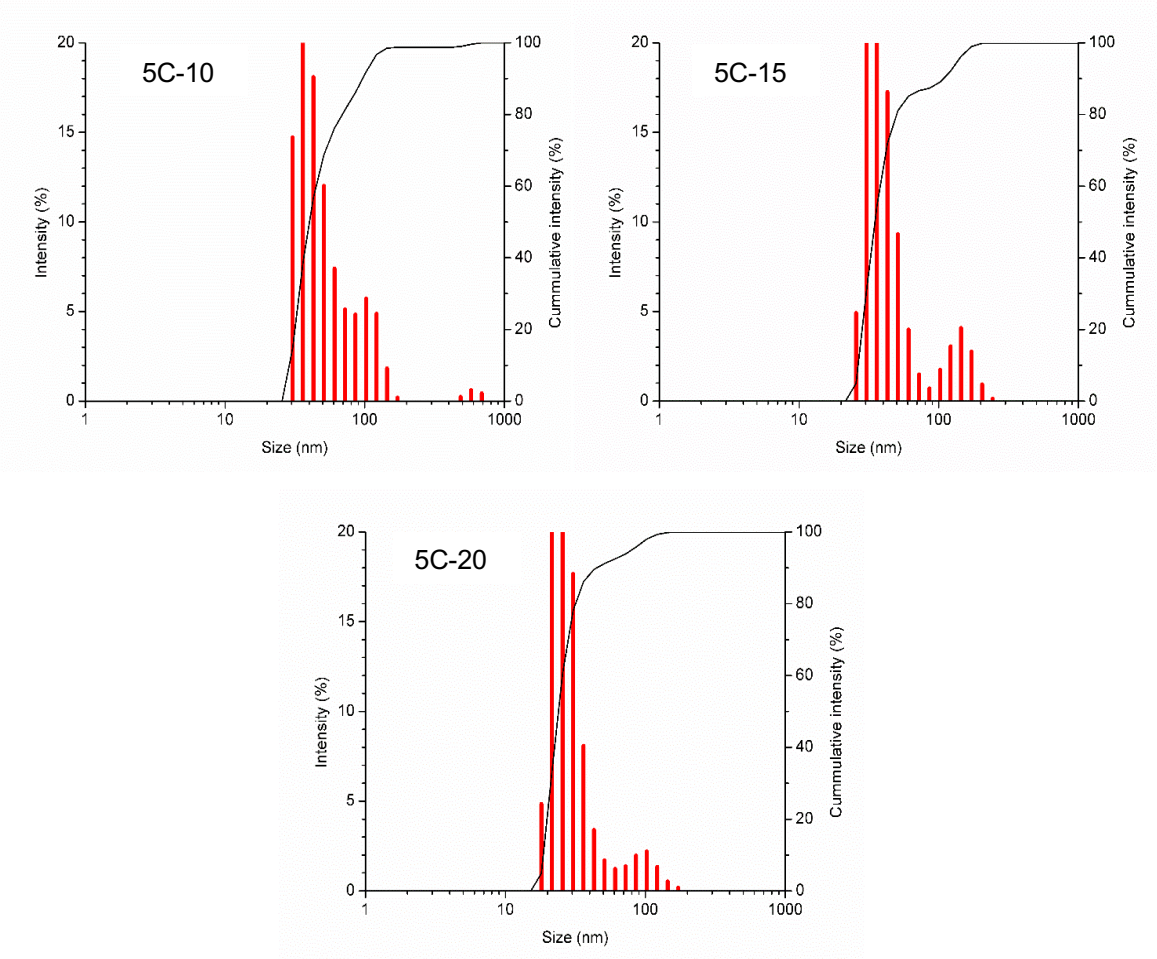

Figure 34. DLS analysis of gold nanoparticles synthesized by microwave in 5 cycles.

4.9.1.2.3 10 cycles

In the synthesis for 10 min with 10 cycles (1 min on, 30 secs off), sonication times were also varied in 10 (10C-10), 15 (10C-15) and 20 min (10C-20). However, under these conditions, the synthesis showed the smaller NP size for 10C-10 followed by 10C-20 and finally 10C-15. This probably because NP synthesized under 10 cycles showed less stability than the synthesized under 5 cycles and no-cycles due to heating was interrupted by cycles resulting in a wider distribution of size, as mentioned before. See Figure 35.

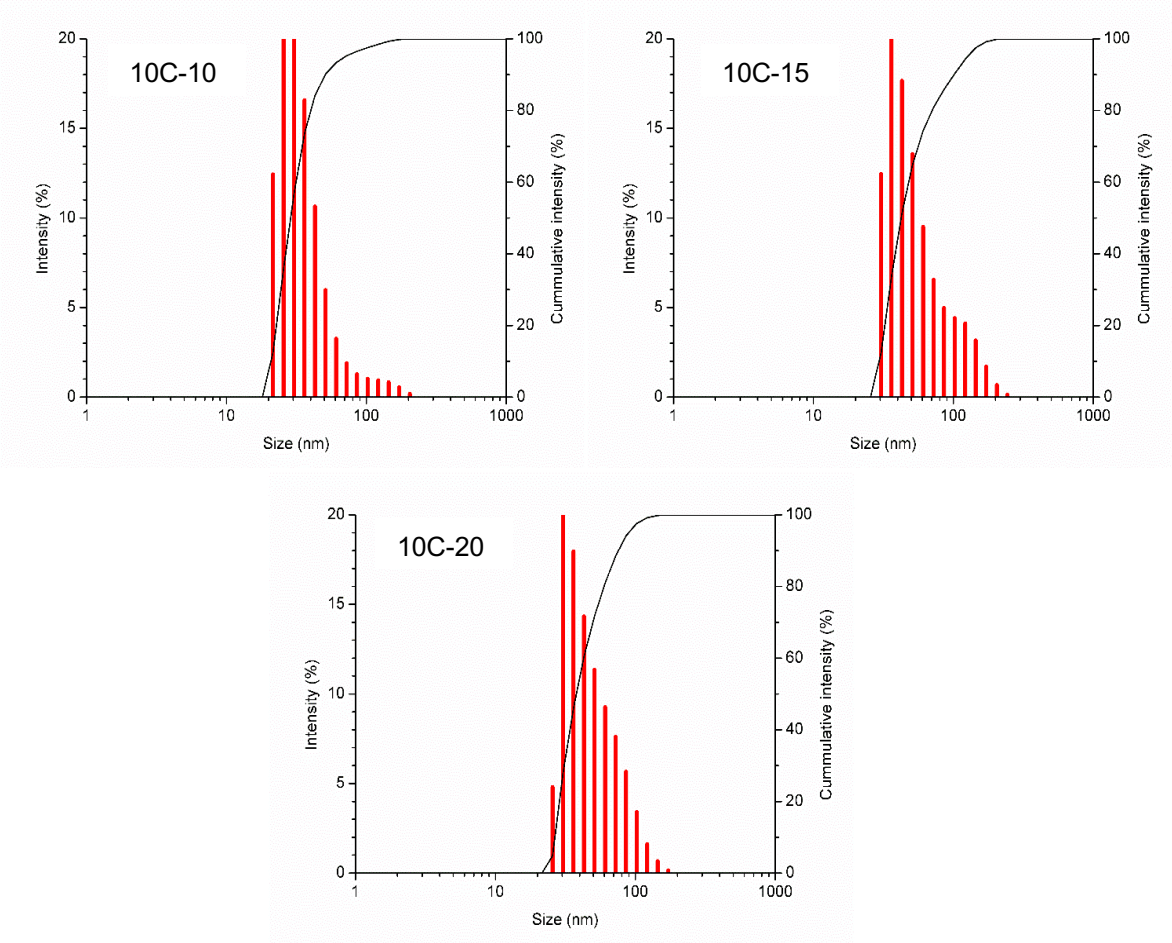

Figure 35. DLS analysis of gold nanoparticles synthesized by microwave in 10 cycles.

Comparing the results obtained by conventional thermal heating method and microwave heating, it can be observed that the first one presents a narrow size distribution, even though the heating by microwave radiation is more uniform, therefore, the synthesis of thermal heating is about 30-40 min which allows to reduce the volume of the solution, reducing in turn the temperature gradient, making heating more uniform. Also, it has been known that increasing the sodium citrate concentration, resulted in narrow size distribution [171].

4.9.2 UV-Vis spectrophotometry

4.9.2.1 Thermal heating method

Gold nanoparticles synthesized under conventional heating method present the characteristic LSPR (around 526 nm), however, this synthesis presents low absorbance as can be observed in Figure 36.

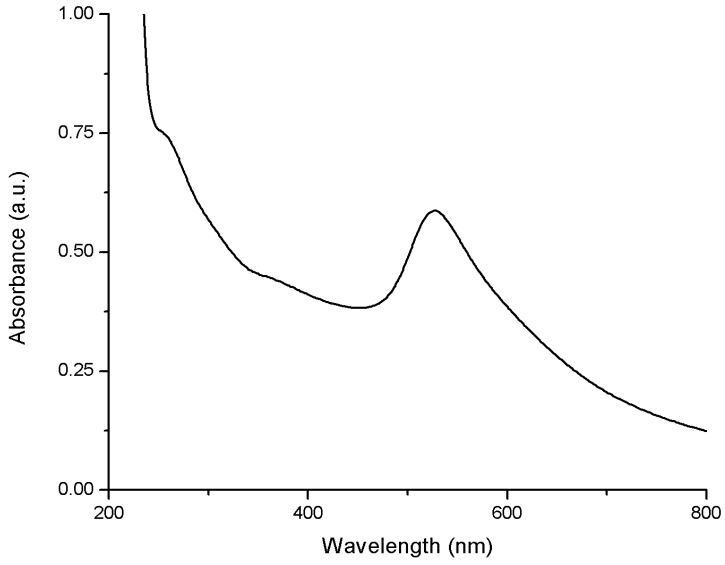

Figure 36. Absorption spectrum of gold NP synthesized by conventional heating method.

4.9.2.2 Microwave

The Lambert-Beer law indicates that the absorbance is directly proportional to the extinction coefficient multiplied by the path length and the concentration of the solution. Therefore, greater absorption it's related to a higher concentration of gold nanoparticles.

Microwave radiation can penetrate the reaction solution with different wavelength (than thermal heating) to heat the solution uniformly, so the concentration of gold nanoparticles is expected to be higher than thermal heating.

4.9.2.3 Without cycles

All the nanoparticles obtained by microwave synthesis for 10 min without cycles, present the characteristic LSPR. It is observed in Figure 37 that these nanoparticles show larger absorption than the obtained by thermal heating method.

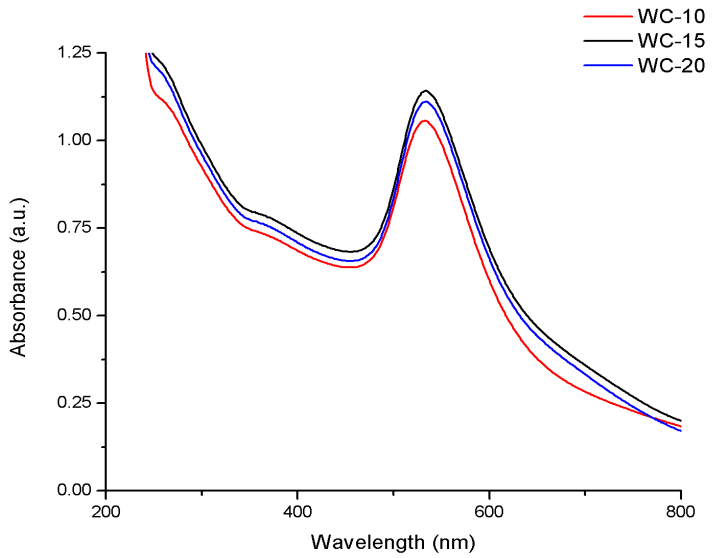

Figure 37. Absorption spectra of gold nanoparticles synthesized by microwave without cycles at different sonication times.

4.9.2.4 5 cycles

Gold nanoparticles obtained by microwave synthesis in 5 cycles show also the LSPR. 5C-20 synthesis showed the larger absorbance indicating, a higher concentration of gold (Figure 38).

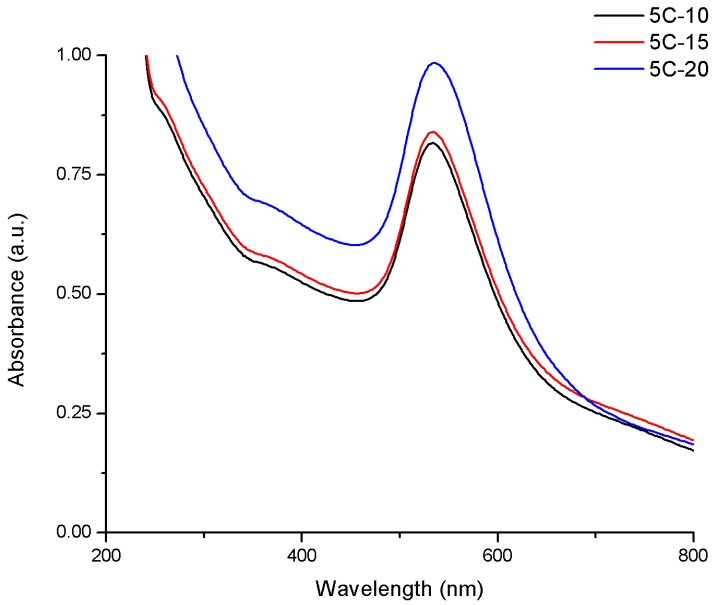

Figure 38. Absorption spectra of gold nanoparticles synthesized by microwave in 5 cycles at different sonication times.

4.9.2.5 10 cycles

Gold nanoparticles obtained by microwave synthesis in 10 cycles show the LSPR. However, it can be observed in Figure 39 that, for the 10C-15 synthesis, the absorbance is as low as the nanoparticles obtained by thermal heating method, possibly due to low stability that is observed under this synthesis, as mentioned earlier.

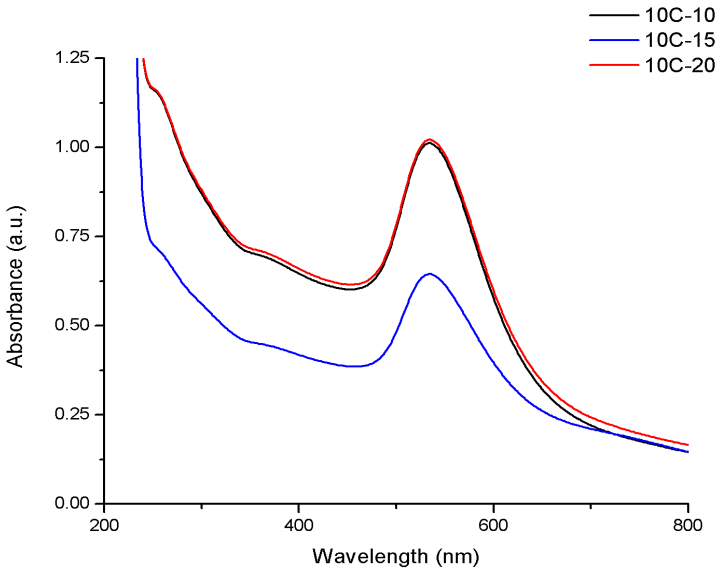

Figure 39. Absorption spectra of gold nanoparticles synthesized by microwave in 10 cycles at different sonication times.

A higher concentration of gold nanoparticles was obtained under microwave radiation; remembering that thermal heating method has higher concentration of sodium citrate, absorbance was expected to be lower.

In a combined analysis of the two techniques DLS and UV-Vis Spectrometry, it was conclude that the best gold nanoparticles were those obtained by synthesis using microwave for 10 min without cycles and sonication of 20 min, because they presented the higher absorption and smaller size distribution, compared with the rest of the synthesis, being both important parameters to consider in optoelectronic applications.

4.9.2.6 Stability

4.9.2.6.1 Stability of plasmon resonance

An additional analysis was made, to observe the stability of the plasmon resonance signal of the nanoparticle solution. The synthesis using microwave without cycles and 20 min of sonication was kept in a dry and dark ambient and its UV-Vis spectrum was measured exactly one year after its synthesis. As can be observed in Figure 40, the plasmon signal presents a decrease almost insignificant, which is an indicative that the nanoparticles remained without agglomerating with each other. Avoiding agglomeration over time is an important factor for the synthesis of nanoparticles because, as the size of the nanoparticle increases, the plasmon resonance signal decrease and therefore the optical properties are lost. It is important to mention that the nanoparticles obtained were kept in its reaction medium, which could had helped to maintain its stability.

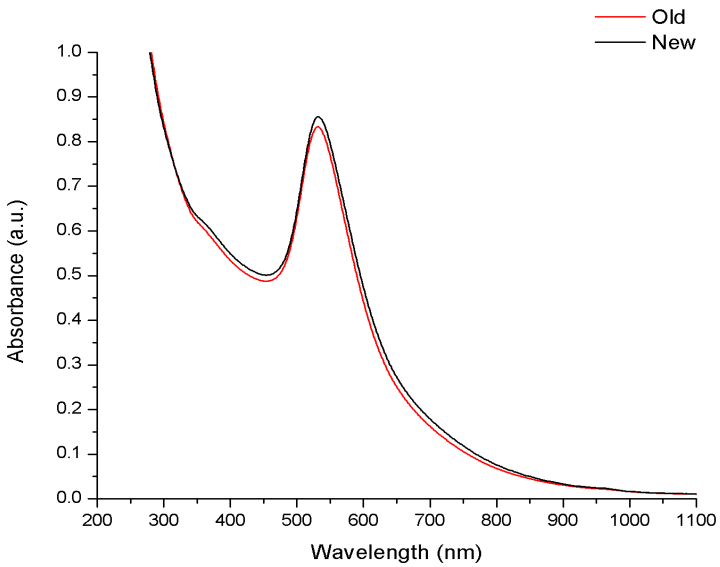

Figure 40. Absorption spectra of gold nanoparticles synthesized by microwave without cycles. Black line represents the newly synthesized nanoparticles and red line represents the same nanoparticle solution one year after its synthesis.

4.9.2.6.2 Stability of nanoparticle size

One of the main problems in nanoparticles solutions is the tendency to agglomerate over time, having as a consequence an increase in size and the loss of properties. Despite of the stability of plasmon resonance, the nanoparticle size tends to increase with time.

Gold nanoparticles (and in general all sort of nanoparticles) tends to form agglomerates, that can be reduced by sonication. Figure 41 shows a comparison of the newly synthesized and one-year aged nanoparticles. Images labeled as (a) and (b) belong to the “fresh synthesis” in which it can be observed the nanospheres in an isolated way; (c) and (d) shows the agglomerated formed by these nanoparticles aged for one year.

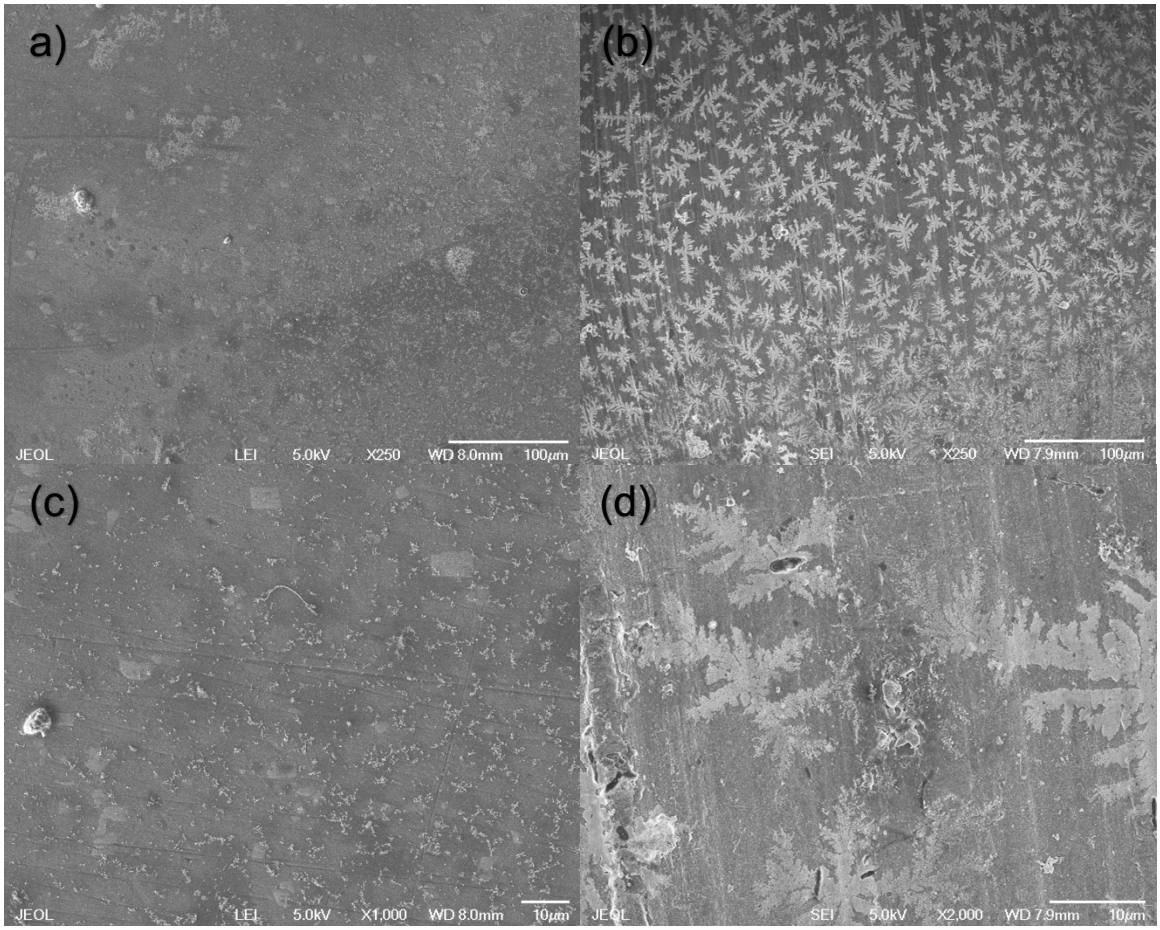

Figure 41. Surface electron microscopy images of gold nanoparticles synthesized by microwave. (a) and (b) are the newly synthesized nanoparticles; (c) and (d) one-year aged nanoparticles.

According to measurements made in an image analyzer, the newly synthesized nanoparticles have an average size between 20 nm and 30 nm (Figure 42a), which can be increased up to 70 nm after one year of being synthesized (Figure 42b).

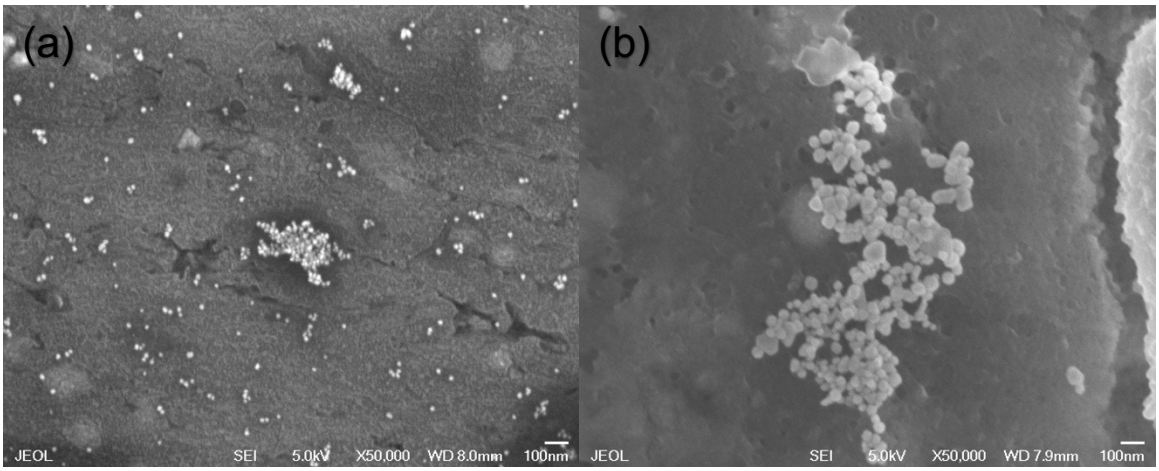

Figure 42. Surface electron microscopy of gold nanoparticles comparing size: (a) newly synthesized and (b) aged for one year.

In addition to the increase in size, these nanoparticles tend to modify its original form by sticking each other to form more complex forms. Figure 43 presents a micrography where, nanospheres, nanorods and nanotriangles of gold are clearly observed.

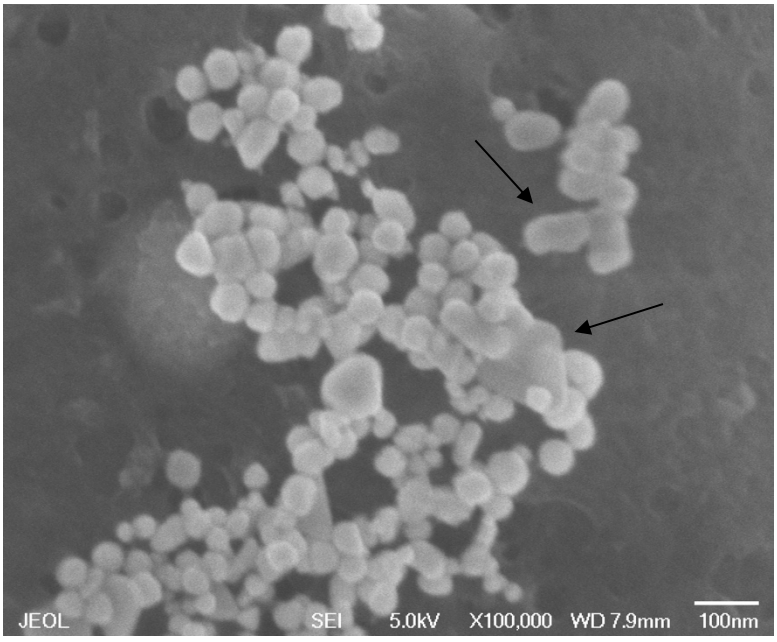

Figure 43. Micrograph of gold nanoparticles after one year of its synthesis, showing different nanoforms.

4.9.2.7 Extinction coefficient.

4.9.2.7.1 Gold atoms per nanoparticle

For the calculation of the average number of gold atoms contained in a nanoparticle, a spherical shape was assumed. Equation 1 was used for this estimation, where ρ is the density of gold (1.93×10^{-20} g/nm^3), N_A is the Avogadro number ($6.02214179 \times 10^{23}$) , M is the atomic mass of gold (197 g/mol) and D is the average diameter of nanoparticles in nm.

$$N = \frac{\pi \rho N_A D^3}{6M} \qquad (1)$$

4.9.2.7.2 Molar concentration

Equation 2 was used for the determination of the molar concentration of the solutions, where N_{Total} is the quantity of gold atoms in the initial solution, V is the reaction volume and N was obtained from equation (1).

$$C = \frac{N_{Total}}{N V N_A} \qquad (2)$$

4.9.2.7.3 Estimation of the coefficients

Extinction coefficients (ε) of gold nanoparticles were calculated according to Lambert-Beer law (Equation 3), where A represents the absorbance in a specific wavelength, *l* is the path length in cm and C is the molar concentration of the solution.

$$A = \varepsilon l C \qquad (3)$$

Table 6 summarizes the molecular concentration and extinction coefficients calculated for each synthesis. It is evident how the extinction coefficient increased, in order of magnitude, with the average size of nanoparticle. Thermal synthesis has the smallest coefficient according to its nanoparticle size, as well as its maximum wavelength that showed a shift to the blue.

Table 6. Extinction coefficients (ε) of the different synthesized nanoparticles.

Synthesis	Average D (nm)	Concentration (mol/L)	Maximum wavelength	Ɛ ($M^{-1}cm^{-1}$)
Thermal	7.5	1.91802E-08	528	2.75E+10
WC-10	65	2.94644E-11	533	1.81E+13
WC-15	55	4.86351E-11	534	1.10E+13
WC-20	27	4.11099E-10	534	1.30E+12
5C-10	38	1.47464E-10	534	3.62E+12
5C-15	35	1.88727E-10	534	2.83E+12
5C-20	22	7.59923E-10	535	7.04E+11
10C-10	28	3.68607E-10	534	1.45E+12
10C-15	40	1.26432E-10	535	4.23E+12
10C-20	30	2.99691E-10	534	1.78E+12

The extinction coefficients were calculated at the maximum absorbance wavelength, i.e. plasmon signal. The variation of the extinction coefficients according to the molar concentration of the gold nanoparticles synthesized by microwave, are presented in Figure 44 showing an exponential behavior.

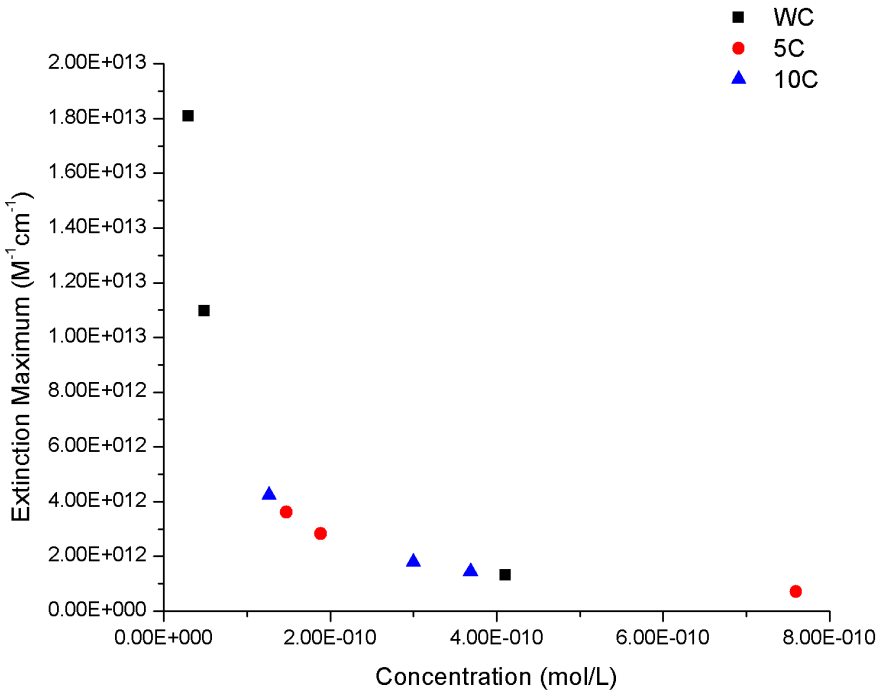

Figure 44. Extinction coefficients of gold nanoparticle synthesized by microwave. Squares represent the gold nanoparticles obtained in continuous heating (without cycles), circles represent the synthesis in 5 cycles and triangles represent the synthesis in 10 cycles.

The curve behavior was adjusted with a power trendline, getting the Equation 4 with a coefficient of determination (R^2) of 0.99999.

$$\varepsilon = 542.61 * C^{-0.999} \quad (4)$$

The natural logarithm of extinction coefficient was also plotted against the natural logarithm of the diameter of the nanoparticles (Figure 45). A linear adjustment was made, obtaining a coefficient of determination (R^2) of 0.999997 in accordance with Mie theory [68, 172]. Equation (5) represents the behavior of plot in Figure 45.

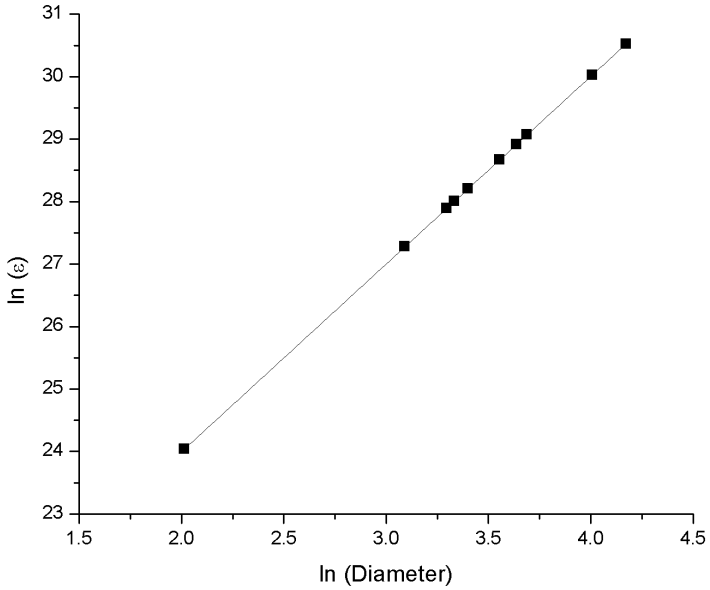

Figure 45. Linear fitting curve of natural logarithm of the extinction coefficients obtained for the different syntheses vs natural logarithm of the diameter of gold nanoparticles synthesized.

$$\ln(\varepsilon) = 3.00464 * \ln(D) + 17.9877 \quad (5)$$

Equation 4 and 5 can be used to estimate important parameters of a gold nanoparticle solution such as average diameter, molar concentration and even the extinction coefficient, as long as one of the parameters has been obtained by a characterization analysis technique. Finding the maximum absorption wavelength, the solution molar concentration can be obtained. On the other hand, if the average diameter is known, the extinction coefficient can be estimated. This can be useful for the experiment planning without the need of extensive characterization.

4.9.2.7.4 Au nanorods synthesized by seedless method

Five different Au nanorods were obtained. Figure 45 shows the UV-Vis spectra and can be observed how the two characteristic plasmon signals are affected by the different aspect ratios (S1 – 18 nm x 4.5 nm, S2 – 25 nm x 5 nm, S3 – 27 nm x 5.5 nm, S4 – 10.5 nm x 2.8 nm, S5 – 14 nm x 4.2 nm). S2 presents the highest absorption and a shift to the red region; according to literature, nanorod size have approximately 25 nm x 5 nm, considered appropriate to be incorporated into solar cells.

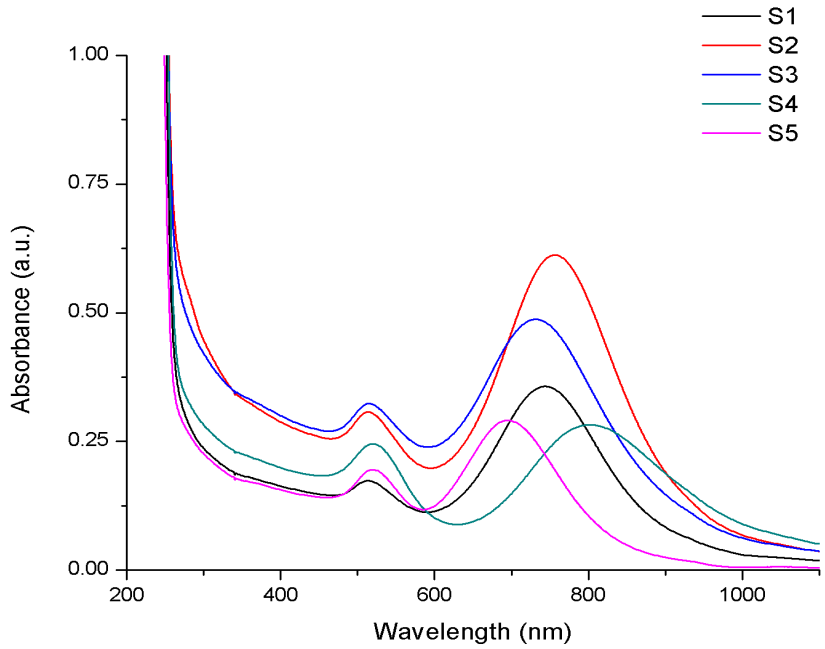

Figure 46. UV-Vis spectra of five different Au nanorods.

4.10 Hybrid active layer

4.10.1 ZnO nanorods on P3HT nanorods

Figure 47 shows the current-time curve of ZnO nanorods formation on ITO glass compared with the curve obtained for ZnO nanorods formation over P3HT nanorods film on ITO glass. As can be notice, the characteristic behavior is maintained, confirming the formation of ZnO nanorods on the P3HT film.

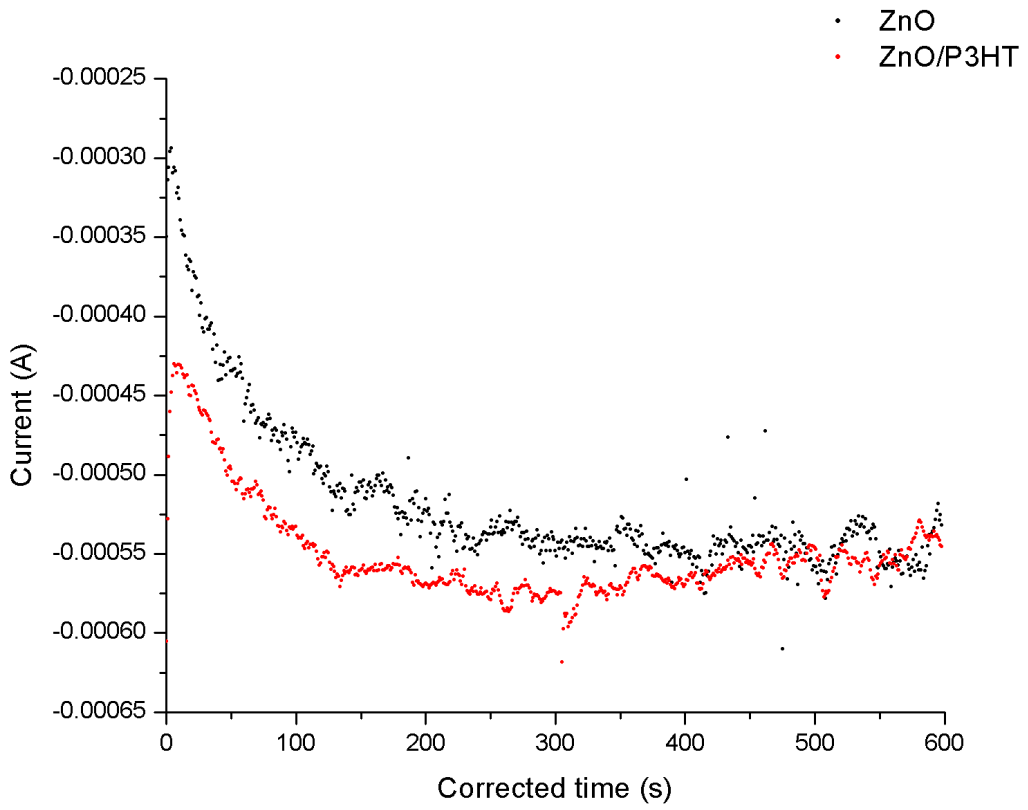

Figure 47. Current-time curve of ZnO nanords deposited on ITO glass (black) and ZnO nanorods deposited on P3HT/ITO (red).

4.10.2 Adding the gold nanoparticles to the ZnO/P3HT active layer

Gold nanoparticles were added to the hybrid active layer by electrophoretic deposition, under the conditions described in section 3. It can be observed, in Figure 48, the configuration used for this process, in which the gold nanoparticle solution synthesized by microwave was used, obtaining an homogeneous gold thin film.

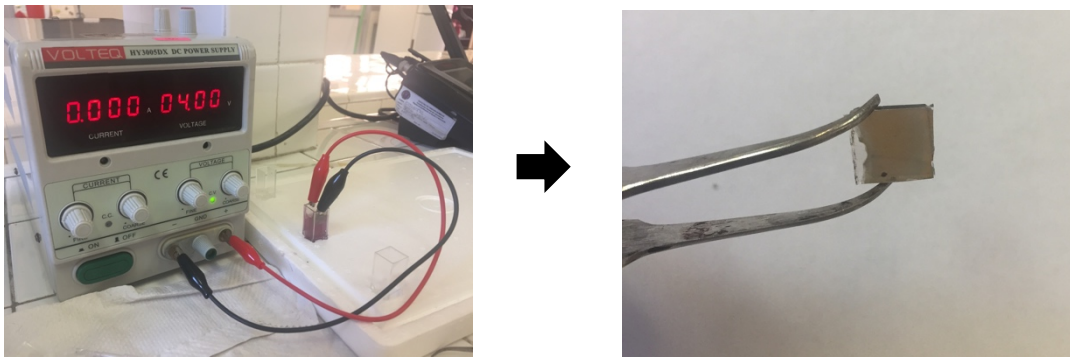

Figure 48. Electrophoretic deposition configuration (left) and gold nanoparticles deposit obtained (right).

4.10.3 Transmittance

Transmittance spectra of ZnO nanorods film and P3HT nanorods film was measured to observe the influence on ITO glass. Figure 49 shows the spectra comparison in which it can be observed the reduction of the transmittance spectrum of ITO glass with the ZnO and P3HT, which is favorable for the active layer, since the absorbance is increased.

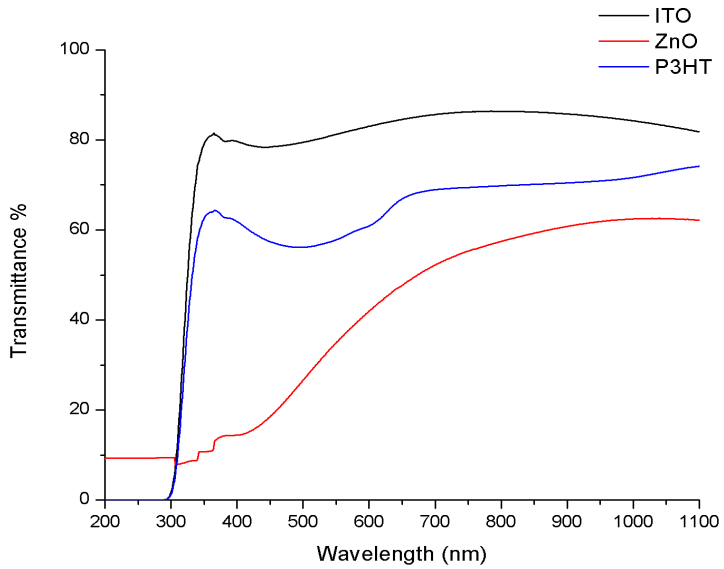

Figure 49. Transmittance spectra of ITO glass (black line), ZnO nanorods on ITO (red line) and P3HT on ITO (blue line).

4.11 J vs V curves

4.11.1 Device D1: configuration (ITO/ZnO/P3HT/Au)

J-V curve is shown in Figure 50 in dark and light for the inverted configuration ITO/ZnO/P3HT/Au; from the data of current density and voltage, power is calculated (P=J*V) to determine the maximum power. Once obtained these data, the basic performance parameters of a solar cell can be estimated.

Table 7. Parameters of the inverted solar cell.

V_{oc} (mV)	J_{sc} (mA/cm^2)	FF (%)	η (%)
400	6.95×10^{-8}	28	7.66×10^{-7}

Due to the little contact of the components of the active layer, low values of short circuit current density and power efficiency were obtained.

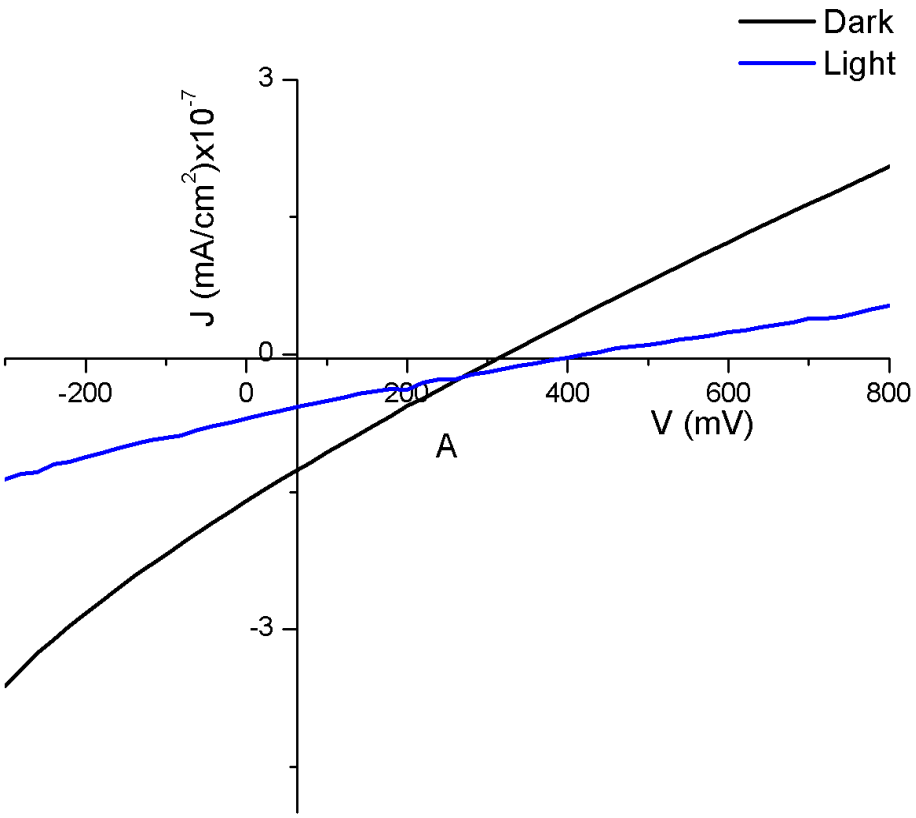

Figure 50. J-V curve of the solar cell with structure ITO/ZnO/P3HT/Au

4.11.2 Device D2: configuration (ITO/P3HT/ZnO/Au)

Figure 51 shows the J-V curve in dark and light for the conventional configuration ITO/P3HT/ZnO/Au. The obtained parameters are listed below.

Table 8. Parameters of the conventional solar cell.

V_{oc} (mV)	J_{sc} (mA/cm^2)	FF (%)	η (%)
200	1.09×10^{-7}	30	6.53×10^{-7}

An improvement in the short circuit current density and fill factor values were obtained under this configuration, however, they remain low due to the little contact in its components. This increment was expected due to due to the ITO

glass (positive electrode) is in direct contact with the P3HT, whereupon holes travel through this, and electrons in opposite direction.

On the other hand, the open circuit voltage of the inverted solar cell was higher than the conventional. This is possibly due to the higher contact between the ZnO and the P3HT achieved in the synthesis.

By increasing the contact between the layers of the solar cells, by means of technical treatment or vacuum deposit, it will be possible to improve the parameters.

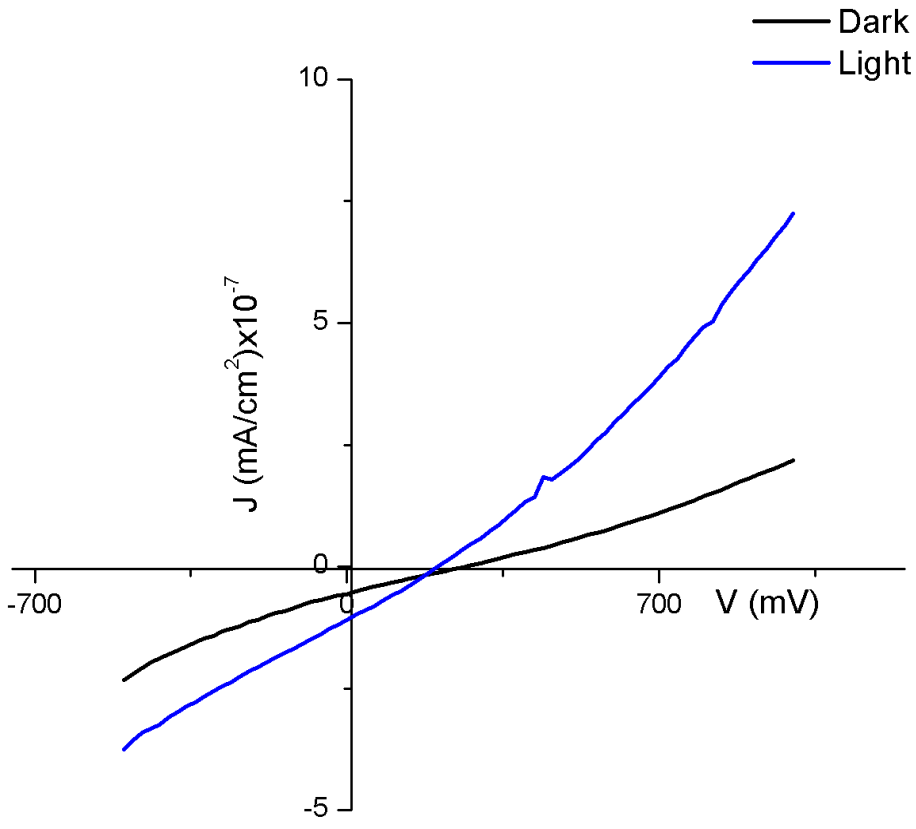

Figure 51. J-V curve of the solar cell with structure ITO/P3HT/ZnO/Au

5. CONCLUSIONS

Al thin films, approximately of 1 μm, were deposited on ITO substrates by two techniques: sputtering and electron gun. However, they present low adherence to the ITO glass and defects in their structure, which prevents the formation of a high-order AAO template.

AAO templates were obtained from aluminum of high purity, pore size of approximately 100 nm by means of a synthesis with 2 anodizations (12 h and 6 min).

P3HT was synthesized by chemical oxidative polymerization of the monomer 3HT using $FeCl_3$ as an oxidizing agent under N_2 atmosphere.

ZnO nanorods vertically aligned on ITO glass substrates were synthesized by the electrochemical reaction of Zn $(NO_3)_2 \cdot 6H_2O$ in a three-electrode cell.

It was possible to adhere P3HT on ITO glass. Which was previously activated with $CHCl_3$. This indicates that the methodology is feasible to perform with the P3HT nanobars.

Gold nanoparticles were synthesized by two methods: conventional heating and microwave. The nanoparticles obtained by conventional heating have a smaller size and narrower size distribution than nanoparticles obtained by microwave, due to the uniformity of the heating.

Gold nanoparticles obtained by microwaves present higher absorbance than those obtained by conventional heating indicating that there is a higher concentration of gold nanoparticles.

Gold nanoparticles obtained by synthesis in microwaves for 10 min without cycles and sonication time of 20 min, present the greater absorption and smaller size distribution, compared with the rest of the synthesis, for which it is established that are the indicated for the incorporation to the active layer. These nanoparticles increase it size after one year, nevertheless plasmon resonance remains almost unaffected.

Gold nanorods were synthesized by seedless method with different values of aspect ratio (S1 – 18 nm x 4.5 nm, S2 – 25 nm x 5 nm, S3 – 27 nm x 5.5 nm, S4 – 10.5 nm x 2.8 nm, S5 – 14 nm x 4.2 nm), according to the signals obtained in the absorption spectra (longitudinal and transversal). S2 was established as the ideal to work in a solar cell since it is the one that presents higher absorption in its longitudinal signal.

Two solar cells were fabricated: conventional ITO/P3HT/ZnO/Au and inverted configuration ITO/ZnO/P3HT/Au. The power efficiency for both cells were low (6.53×10^{-7} for the conventional and 7.66×10^{-7} for the inverted) due to the little contact of the layers of the solar cell.

6. REFERENCES

1 Kaldellis, J.K., Apostolou, D.: 'Life cycle energy and carbon footprint of offshore wind energy. Comparison with onshore counterpart' *Renew. Energy*, 2017, **108**, pp. 72–84.

2 Shahriari, M., Blumsack, S.: 'Scaling of wind energy variability over space and time' *Appl. Energy*, 2017, **195**, pp. 572–585.

3 Al-falahi, M.D.A., Jayasinghe, S.D.G., Enshaei, H.: 'A review on recent size optimization methodologies for standalone solar and wind hybrid renewable energy system' *Energy Convers. Manag.*, 2017, **143**, pp. 252–274.

4 Tang, H.S., Kraatz, S., Qu, K., Chen, G.Q., Aboobaker, N., Jiang, C.B.: 'High-resolution survey of tidal energy towards power generation and influence of sea-level-rise: A case study at coast of New Jersey, USA' *Renew. Sustain. Energy Rev.*, 2014, **32**, pp. 960–982.

5 Yah, N.F., Oumer, A.N., Idris, M.S.: 'Small scale hydro-power as a source of renewable energy in Malaysia: A review' *Renew. Sustain. Energy Rev.*, 2017, **72**, pp. 228–239.

6 Dadu, V., Dadu, A., Frunza, D., Catarig, G., Popa, F., Popa, B.: 'Innovative Concepts Applied to Recent Small Hydropower Plants' *Energy Procedia*, 2017, **112**, pp. 426–433.

7 Balkhair, K.S., Rahman, K.U.: 'Sustainable and economical small-scale and low-head hydropower generation: A promising alternative potential solution for energy generation at local and regional scale' *Appl. Energy*, 2017, **188**, pp. 378–391.

8 Neiva de Figueiredo, J., Mayerle, S.F.: 'A systemic approach for dimensioning and designing anaerobic bio-digestion/energy generation biomass supply networks' *Renew. Energy*, 2014, **71**, pp. 690–694.

9 Mussard, M.: 'Solar energy under cold climatic conditions: A review' *Renew. Sustain. Energy Rev.*, 2017, **74**, pp. 733–745.

10 Sütterlin, B., Siegrist, M.: 'Public acceptance of renewable energy technologies from an abstract versus concrete perspective and the positive imagery of solar power' *Energy Policy*, 2017, **106**, pp. 356–366.

11 Mohamed, M.H., William, G.E., Fatouh, M.: 'Solar energy utilization in water production from humid air' *Sol. Energy*, 2017, **148**, pp. 98–109.

12 Bağmancı, M., Karaaslan, M., Ünal, E., Akgol, O., Karadağ, F., Sabah, C.: 'Broad-band polarization-independent metamaterial absorber for solar

energy harvesting applications' *Phys. E Low-dimensional Syst. Nanostructures*, 2017, **90**, pp. 1–6.

13 Amin, N., Ahmad Shahahmadi, S., Chelvanathan, P., Rahman, K.S., Istiaque Hossain, M., Akhtaruzzaman, M.D.: 'Solar Photovoltaic Technologies: From Inception Toward the Most Reliable Energy Resource', in 'Reference Module in Earth Systems and Environmental Sciences' (2017)

14 Wang, Q., Xie, Y., Soltani-Kordshuli, F., Eslamian, M.: 'Progress in emerging solution-processed thin film solar cells - Part I: Polymer solar cells' *Renew. Sustain. Energy Rev.*, 2016, **56**, pp. 347–361.

15 Mali, S.S., Shim, C.S., Kim, H., Patil, P.S., Hong, C.K.: 'In situ processed gold nanoparticle-embedded TiO_2 nanofibers enabling plasmonic perovskite solar cells to exceed 14% conversion efficiency' *Nanoscale*, 2016, **8**, (5), pp. 2664–2677.

16 Minqi, L.: 'World Energy 2017-2050: Annual Report' (2017)

17 Jean, J., Brown, P.R., Jaffe, R.L., Buonassisi, T., Bulović, V.: 'Pathways for solar photovoltaics' *Energy Environ. Sci.*, 2015, **8**, (4), pp. 1200–1219.

18 Nelson, J.: 'The Physics of Solar Cells' (Imperial College Press, 2003)

19 Venugopal, N., Kaur, G., Mitra, A.: 'Plasmonics effect of Ag nanoislands covered n-Al:ZnO/p-Si heterostructure' *Appl. Surf. Sci.*, 2014, **320**, pp. 30–42.

20 Sánchez De La Morena, S., Recio-Sánchez, G., Torres-Costa, V., Martín-Palma, R.J.: 'Hybrid gold/porous silicon thin films for plasmonic solar cells' *Scr. Mater.*, 2014, **74**, pp. 33–37.

21 Ren, X., Li, X., Choy, W.C.H.: 'Optically enhanced semi-transparent organic solar cells through hybrid metal/nanoparticle/dielectric nanostructure' *Nano Energy*, 2015, **17**, pp. 187–195.

22 Liu, Y., Zi, W., Liu, S. (Frank), Yan, B.: 'Effective light trapping by hybrid nanostructure for crystalline silicon solar cells' *Sol. Energy Mater. Sol. Cells*, 2015, **140**, pp. 180–186.

23 Wu, J., Yu, P., Susha, A.S., *et al.*: 'Broadband efficiency enhancement in quantum dot solar cells coupled with multispiked plasmonic nanostars' *Nano Energy*, 2015, **13**, pp. 827–835.

24 Hu, Z., Dong, S., Xue, Q., *et al.*: 'In-situ synthesis of metal nanoparticle-polymer composites and their application as efficient interfacial materials for both polymer and planar heterojunction perovskite solar cells' *Org. Electron.*, 2015, **27**, pp. 46–52.

25 Krajangsang, T., Inthisang, S., Sritharathikhun, J., *et al.*: ‘An intrinsic amorphous silicon oxide and amorphous silicon stack passivation layer for crystalline silicon heterojunction solar cells’ *Thin Solid Films*, 2017, **628**, pp. 107–111.

26 Yang, L., Liu, Y., Wang, Y., *et al.*: ‘18.87%-efficient inverted pyramid structured silicon solar cell by one-step Cu-assisted texturization technique’ *Sol. Energy Mater. Sol. Cells*, 2017, **166**, pp. 121–126.

27 Xu, M., Bearda, T., Sivaramakrishnan Radhakrishnan, H., *et al.*: ‘Silicon heterojunction interdigitated back-contact solar cells bonded to glass with efficiency >21%’ *Sol. Energy Mater. Sol. Cells*, 2017, **165**, pp. 82–87.

28 Wang, Q., Pan, C., Chen, K., Zou, S., Shen, M., Su, X.: ‘Efficient nanostructured quasi-single crystalline silicon solar cells by metal-catalyzed chemical etching’ *Sol. Energy Mater. Sol. Cells*, 2017, **164**, pp. 40–46.

29 Chebotareva, A.B., Untila, G.G., Kost, T.N., Stepanov, A.S., Salazkin, S.N., Shaposhnikova, V.V.: ‘Transparent conductive polymers for laminated multi-wire metallization of bifacial concentrator crystalline silicon solar cells with TCO layers’ *Sol. Energy Mater. Sol. Cells*, 2017, **165**, pp. 1–8.

30 Xie, F., Choy, W.C.H., Sha, W.E.I., *et al.*: ‘Enhanced charge extraction in organic solar cells through electron accumulation effects induced by metal nanoparticles’ *Energy Environ. Sci.*, 2013, **6**, (11), p. 3372.

31 Xia, Z., Song, T., Sun, J., Lee, S.-T., Sun, B.: ‘Plasmonic enhancement in hybrid organic/Si heterojunction solar cells enabled by embedded gold nanoparticles’ *Appl. Phys. Lett.*, 2014, **105**, (24), p. 241110.

32 El alamy, A., Bourass, M., Amine, A., Hamidi, M., Bouachrine, M.: ‘New organic dyes based on phenylenevinylene for solar cells: DFT and TD-DFT investigation’ *Karbala Int. J. Mod. Sci.*, 2017, **3**, (2), pp. 75–82.

33 Jiang, X., Wang, Z., Han, W., *et al.*: ‘High performance silicon-organic hybrid solar cells via improving conductivity of PEDOT:PSS with reduced graphene oxide’ *Appl. Surf. Sci.*, 2017, **407**, pp. 398–404.

34 Agrawal, N., Zubair Ansari, M., Majumdar, A., Gahlot, R., Khare, N.: ‘Efficient up-scaling of organic solar cells’ *Sol. Energy Mater. Sol. Cells*, 2016, **157**, pp. 960–965.

35 Wright, M., Uddin, A.: ‘Organic-inorganic hybrid solar cells: A comparative review’ *Sol. Energy Mater. Sol. Cells*, 2012, **107**, pp. 87–111.

36 Haidari, G., Hajimahmoodzadeh, M., Fallah, H.R., Varnamkhasti, M.G.: ‘Effective medium analysis of thermally evaporated Ag nanoparticle films for plasmonic enhancement in organic solar cell’ *Superlattices Microstruct.*, 2015, **85**, pp. 294–304.

37 Sharma, R., Lee, H., Borse, K., *et al.*: 'Ga-doped ZnO as an electron transport layer for PffBT4T-2OD: PC70BM organic solar cells' *Org. Electron.*, 2017, **43**, pp. 207–213.

38 Cha, H., Park, C.E., Kwon, S.-K., An, T.K.: 'Ternary blends to achieve well-developed nanoscale morphology in organic bulk heterojunction solar cells' *Org. Electron.*, 2017, **45**, pp. 263–272.

39 Liu, C., Luo, H., Shi, G., Nian, L., Chi, Z., Ma, Y.: 'Electrochemical route to fabricate porous organic polymers film and its application for polymer solar cells' *Dye. Pigment.*, 2017, **142**, pp. 132–138.

40 Hassan, A., Kadem, B., Cranton, W.: 'Organic solar cells: Study of combined effects of active layer nanostructure and electron and hole transport layers' *Thin Solid Films*, 2017, **636**, pp. 760–764.

41 Jung, G.H., Lee, J.-L.: 'Origin of gap states in the electron transport layer of organic solar cells' *J. Mater. Chem. A*, 2013, **1**, (9), p. 3034.

42 Chapel, A., Dkhil, S. Ben, Therias, S., *et al.*: 'Effect of ZnO nanoparticles on the photochemical and electronic stability of P3HT used in polymer solar cells' *Sol. Energy Mater. Sol. Cells*, 2016, **155**, pp. 79–87.

43 Jia, Z., Wei, Y., Wang, X., Hu, S., Yao, K., Li, F.: 'Improvement of morphology and performance of P3HT/ZnO hybrid solar cells induced by liquid crystal molecules' *Chem. Phys. Lett.*, 2016, **661**, pp. 119–124.

44 Bliznyuk, V.N., Gasiorowski, J., Ishchenko, A.A., *et al.*: 'Photovoltaic cells based on ternary P3HT:PCBM:polymethine dye active layer transparent in the visible range of light' *Appl. Surf. Sci.*, 2016, **389**, pp. 419–427.

45 Gollu, S.R., Sharma, R., Srinivas, G., Kundu, S., Gupta, D.: 'Incorporation of silver and gold nanostructures for performance improvement in P3HT: PCBM inverted solar cell with rGO/ZnO nanocomposite as an electron transport layer' *Org. Electron.*, 2016, **29**, pp. 79–87.

46 Fakharan, Z., Naji, L.: 'Fabrication of non-fullerene P3HT/Agx-TiO_2 based polymer solar cells with high open circuit voltage' *J. Alloys Compd.*, 2017, **708**, pp. 1184–1194.

47 Ikram, M., Imran, M., Nunzi, J.M., Islah-u-din, Ali, S.: 'Replacement of P3HT and PCBM with metal oxides nanoparticles in inverted hybrid organic solar cells' *Synth. Met.*, 2015, **210**, pp. 268–272.

48 Chen, B., Liu, C., Ge, L., Hayashi, K.: 'Electrical conduction and gas sensing characteristics of P3HT/Au nano-islands composite' *Sensors Actuators B Chem.*, 2017, **241**, pp. 1099–1105.

49 Dasgupta, U., Saha, S.K., Pal, A.J.: 'Plasmonic effect in pn-junction solar cells based on layers of semiconductor nanocrystals: Where to introduce

metal nanoparticles?' *Sol. Energy Mater. Sol. Cells*, 2015, **136**, pp. 106–112.

50 Tarwal, N.L., Devan, R.S., Ma, Y.R., Patil, R.S., Karanjkar, M.M., Patil, P.S.: 'Spray deposited localized surface plasmonic Au–ZnO nanocomposites for solar cell application' *Electrochim. Acta*, 2012, **72**, pp. 32–39.

51 Arici, E., Karazhanov, S.: 'Carbon nanotubes for organic/inorganic hybrid solar cells' *Mater. Sci. Semicond. Process.*, 2016, **41**, pp. 137–149.

52 Elumalai, N.K., Uddin, A.: 'Hysteresis in organic-inorganic hybrid perovskite solar cells' *Sol. Energy Mater. Sol. Cells*, 2016, **157**, pp. 476–509.

53 Tang, S., Tang, N., Meng, X., Huang, S., Hao, Y.: 'Enhanced power efficiency of ZnO based organic/inorganic solar cells by surface modification' *Phys. E Low-dimensional Syst. Nanostructures*, 2016, **83**, pp. 398–404.

54 Ge, Z., Xu, L., Zhang, R., *et al.*: 'Improved performance of silicon nanowire/cadmium telluride quantum dots/organic hybrid solar cells' *Appl. Surf. Sci.*, 2015, **334**, pp. 15–18.

55 Mu, X., Yu, X., Xu, D., *et al.*: 'High efficiency organic/silicon hybrid solar cells with doping-free selective emitter structure induced by a WO_3 thin interlayer' *Nano Energy*, 2015, **16**, pp. 54–61.

56 Kittel, C.: 'Introduction to Solid State Physics' (1985, Eighth Edi)

57 Maier, S.: 'Plasmonics : Fundamentals and Applications' (Springer Science, 2007)

58 Petryayeva, E., Krull, U.J.: 'Localized surface plasmon resonance: Nanostructures, bioassays and biosensing-A review' *Anal. Chim. Acta*, 2011, **706**, (1), pp. 8–24.

59 Mandal, P., Sharma, S.: 'Progress in plasmonic solar cell efficiency improvement: A status review' *Renew. Sustain. Energy Rev.*, 2016, **65**, pp. 537–552.

60 Watanabe, R., Miyano, K.: 'Metal nanoparticles in a photovoltaic cell: Effect of metallic loss' *AIP Adv.*, 2011, **1**, (4), p. 042154.

61 Skrabalak, S.E., Au, L., Li, X., Xia, Y.: 'Facile synthesis of Ag nanocubes and Au nanocages.' *Nat. Protoc.*, 2007, **2**, (9), pp. 2182–2190.

62 Wang, L., Song, Y., Sun, L., Guo, C., Sun, Y., Li, Z.: 'Controllable synthesis of gold nanowires' *Mater. Lett.*, 2008, **62**, (25), pp. 4124–4126.

63 Eller, P.C.H., Haastrup, S.: 'Preparation and characterization of metal nanoparticles'2011.

64 Link, S., Link, S., El-Sayed, M. a., El-Sayed, M.: 'Spectral Properties and Relaxation Dynamics of Surface Plasmon Electronic Oscillations in Gold and Silver Nanodots and Nanorods' *J. Phys. Chem. B*, 1999, **103**, (40), pp. 8410–8426.

65 Noguez, C.: 'Surface Plasmons on Metal Nanoparticles: The Influence of Shape and Physical Environment' *J. Phys. Chem. C*, 2007, **111**, (10), pp. 3806–3819.

66 Horikoshi, S., Serpone, N.: 'Microwaves in Nanoparticles Synthesis: Fundamentals and Applications' (2013)

67 Koole, R., Groeneveld, E., Vanmaekelbergh, D., Meijerink, A., de Mello Donegá, C.: 'Size Effects on Semiconductor Nanoparticles', in de Mello Donegá, C. (Ed.): 'Nanoparticles: Workhorses of Nanoscience' (Springer Berlin Heidelberg, 2014), pp. 13–51

68 Horvath, H.: 'Light scattering: Mie and More commemorating 100 years of Mie's 1908 publication' *J. Quant. Spectrosc. Radiat. Transf.*, 2009, **110**, (11), pp. 783–786.

69 Lee, J.M., Kim, S.O.: 'Enhancing organic solar cells with plasmonic nanomaterials' *ChemNanoMat*, 2016, **2**, (1), pp. 19–27.

70 Tang, M., Sun, B., Zhou, D., *et al.*: 'Broad-band plasmonic Cu-Au bimetallic nanoparticles for organic bulk heterojunction solar cells' *Org. Electron.*, 2016, **38**, pp. 213–221.

71 del Rio, M., Palomino Cabello, C., Gonzalez, V., *et al.*: 'Metal Oxide Assisted Preparation of Core-Shell Beads with Dense Metal-Organic Framework Coatings for the Enhanced Extraction of Organic Pollutants' *Chem. - A Eur. J.*, 2016, **22**, (33), pp. 11770–11777.

72 Gawande, M.B., Goswami, A., Asefa, T., *et al.*: 'Core-shell nanoparticles: synthesis and applications in catalysis and electrocatalysis' *Chem. Soc. Rev.*, 2015, **44**, (21), pp. 7540–7590.

73 Segal-Peretz, T., Sorias, O., Moshonov, M., Deckman, I., Orenstein, M., Frey, G.L.: 'Plasmonic nanoparticle incorporation into inverted hybrid organic-inorganic solar cells' *Org. Electron. physics, Mater. Appl.*, 2015, **23**, pp. 144–150.

74 Fu, W.-F., Chen, X., Yang, X., *et al.*: 'Optical and electrical effects of plasmonic nanoparticles in high-efficiency hybrid solar cells' *Phys. Chem. Chem. Phys.*, 2013, **15**, (40), pp. 17105–17111.

75 Chung, C.-C., Tran, B.T., Lin, K.-L., *et al.*: 'Efficiency improvement of InGaP/GaAs/Ge solar cells by hydrothermal-deposited ZnO nanotube structure.' *Nanoscale Res. Lett.*, 2014, **9**, (1), p. 338.

76 Liu, A., Ren, Q., Zhao, M., *et al.*: 'Photovoltaic performance enhancement of CdS quantum dot-sensitized TiO_2 photoanodes with plasmonic gold nanoparticles' *J. Alloys Compd.*, 2014, **589**, pp. 218–225.

77 Xue, M., Li, L., Tremolet De Villers, B.J., *et al.*: 'Charge-carrier dynamics in hybrid plasmonic organic solar cells with Ag nanoparticles' *Appl. Phys. Lett.*, 2011, **98**, (25), pp. 16–19.

78 Pillai, S., Green, M.A.: 'Plasmonics for photovoltaic applications' *Sol. Energy Mater. Sol. Cells*, 2010, **94**, (9), pp. 1481–1486.

79 Atwater, H.A., Polman, A.: 'Plasmonics for improved photovoltaic devices' *Nat. Mater.*, 2010, **9**, (10), pp. 865–865.

80 Achermann, M.: 'Exciton-plasmon interactions in metal-semiconductor nanostructures' *J. Phys. Chem. Lett.*, 2010, **1**, (19), pp. 2837–2843.

81 Stratakis, E., Kymakis, E.: 'Nanoparticle-based plasmonic organic photovoltaic devices' *Mater. Today*, 2013, **16**, (4), pp. 133–146.

82 Hong, L., Wang, X., Zheng, H., Wang, J., Wang, H., Yu, H.: 'Si/PEDOT:PSS hybrid solar cells incorporated with silver plasmonic nanospheres' *Thin Solid Films*, 2016, **599**, pp. 37–41.

83 Aurang, P., Doganay, D., Bek, A., Turan, R., Unalan, H.E.: 'Silver nanowire networks as transparent top electrodes for silicon solar cells' *Sol. Energy*, 2017, **141**, pp. 110–117.

84 Knight, M.W., van de Groep, J., Bronsveld, P.C.P., Sinke, W.C., Polman, A.: 'Soft imprinted Ag nanowire hybrid electrodes on silicon heterojunction solar cells' *Nano Energy*, 2016, **30**, pp. 398–406.

85 Jarrett, R., Kanda, H., Harano, N., Noguchi, T., Crook, R., Ito, S.: 'Evidence of plasmonic effects in random orientation silver nanowire meshes on silicon' *Sol. Energy*, 2015, **116**, pp. 257–264.

86 Wu, J., Mangham, S.C., Reddy, V.R., Manasreh, M.O., Weaver, B.D.: 'Surface plasmon enhanced intermediate band based quantum dots solar cell' *Sol. Energy Mater. Sol. Cells*, 2012, **102**, pp. 44–49.

87 Xiao, H., Wang, J., Huang, H., *et al.*: 'Performance optimization of flexible a-Si: H solar cells with nanotextured plasmonic substrate by tuning the thickness of oxide spacer layer' *Nano Energy*, 2015, **11**, pp. 78–87.

88 Saravanan, S., Dubey, R.S.: 'Optical absorption enhancement in 40nm ultrathin film silicon solar cells assisted by photonic and plasmonic modes' *Opt. Commun.*, 2016, **377**, pp. 65–69.

89 Tzounis, L., Gravalidis, C., Papamichail, A., Logothetidis, S.: 'Enhancement of P3HT:PCBM Photovoltaic Shells Efficiency Incorporating Core-shell

Au@Ag Plasmonic Nanoparticles1' *Mater. Today Proc.*, 2016, **3**, (3), pp. 832–839.

90 Al-Azawi, M.A., Bidin, N., Bououdina, M., Mohammad, S.M.: 'Preparation of gold and gold-silver alloy nanoparticles for enhancement of plasmonic dye-sensitized solar cells performance' *Sol. Energy*, 2016, **126**, pp. 93–104.

91 Cheng, K., Wu, Y., Meng, J., Zhao, Y., Wang, X., Du, Z.: 'Plasmon-enhanced photocurrent generation in quantum dots-sensitized solar cells by coupling of gold nanocrystals' *Sci. Bull.*, 2015, **60**, (5), pp. 541–548.

92 Eskandari, M., Ahmadi, V., Yousefi rad, M., Kohnehpoushi, S.: 'Plasmon enhanced CdS-quantum dot sensitized solar cell using ZnO nanorods array deposited with Ag nanoparticles as photoanode' *Phys. E Low-dimensional Syst. Nanostructures*, 2015, **68**, pp. 202–209.

93 Kim, S.-S., Na, S.-I., Jo, J., Kim, D.-Y., Nah, Y.-C.: 'Plasmon enhanced performance of organic solar cells using electrodeposited Ag nanoparticles' *Appl. Phys. Lett.*, 2008, **93**, (073307), pp. 1–3.

94 Gao, Y., Jin, F., Su, Z., *et al.*: 'All thermal-evaporated surface plasmon enhanced organic solar cells by Au nanoparticles' *Org. Electron.*, 2016, **39**, pp. 71–76.

95 Liu, K., Bi, Y., Qu, S., *et al.*: 'Efficient hybrid plasmonic polymer solar cells with Ag nanoparticle decorated TiO_2 nanorods embedded in the active layer.' *Nanoscale*, 2014, **6**, (11), pp. 6180–6.

96 Markvart, T., Castañer, L.: 'Principles of Solar Cell Operation', in McEvoy, A., Castañer, L., Markvart, T.B.T.-S.C. (Second E. (Eds.): 'Solar Cells: Materials, Manufacture and Operation' (Elsevier, 2013), pp. 3–25

97 Jørgensen, M., Norrman, K., Krebs, F.C.: 'Stability/degradation of polymer solar cells' *Sol. Energy Mater. Sol. Cells*, 2008, **92**, (7), pp. 686–714.

98 Kwak, D.-J., Moon, B.-H., Lee, D.-K., Park, C.-S., Sung, Y.-M.: 'Comparison of transparent conductive indium tin oxide, titanium-doped indium oxide, and fluorine-doped tin oxide films for dye-sensitized solar cell application' *J. Electr. Eng. Technol.*, 2011, **6**, (5), pp. 684–687.

99 Aziz, N. a. N., Isa, M.I.N., Hasiah, S.: 'Electrical and Hall Effect Study of Hybrid Solar Cell' *J. Clean Energy Technol.*, 2014, **2**, (4), pp. 322–326.

100 Chamberlain, G.A.: 'Organic Solar Cells: A Review' *Sol. Cells*, 1983, **8**, pp. 47–83.

101 Atyaoui, M., Atyaoui, A., Khalifa, M., Elyagoubi, J., Dimassi, W., Ezzaouia, H.: 'Enhancement in photovoltaic properties of silicon solar cells by surface plasmon effect of palladium nanoparticles' *Superlattices Microstruct.*, 2016, **92**, pp. 217–223.

102 Tu, W.-C., Chang, Y.-T., Wang, H.-P., *et al.*: 'Improved light scattering and surface plasmon tuning in amorphous silicon solar cells by double-walled carbon nanotubes' *Sol. Energy Mater. Sol. Cells*, 2012, **101**, pp. 200–203.

103 Lee, J.H., Park, J.H., Kim, J.S., Lee, D.Y., Cho, K.: 'High efficiency polymer solar cells with wet deposited plasmonic gold nanodots' *Org. Electron.*, 2009, **10**, (3), pp. 416–420.

104 Baek, S.-W.W., Park, G., Noh, J., *et al.*: 'Au@Ag core-shell nanocubes for efficient plasmonic light scattering effect in low bandgap organic solar cells' *ACS Nano*, 2014, **8**, (4), pp. 3302–3312.

105 Lee, D., Jeong, S., Park, J.H., Park, S.Y., Jang, D.J.: 'Effects of gold nanorods on the excited-state dynamics and photovoltaic performances of hybrid nanocomposites containing poly(3-hexylthiophene)' *J. Mater. Sci.*, 2016, **51**, (21), pp. 9669–9678.

106 de León, A., Arias, E., Moggio, I., *et al.*: 'Synthesis of mercaptopropyl-(phenylene)s-benzoates passivated gold nanoparticles: Implications for plasmonic photovoltaic cells' *J. Colloid Interface Sci.*, 2015, **456**, pp. 182–189.

107 Yoon, W.-J., Jung, K.-Y., Liu, J., *et al.*: 'Plasmon-enhanced optical absorption and photocurrent in organic bulk heterojunction photovoltaic devices using self-assembled layer of silver nanoparticles' *Sol. Energy Mater. Sol. Cells*, 2010, **94**, (2), pp. 128–132.

108 Fung, D.D.S., Qiao, L., Choy, W.C.H., *et al.*: 'Optical and electrical properties of efficiency enhanced polymer solar cells with Au nanoparticles in a PEDOT–PSS layer' *J. Mater. Chem.*, 2011, **21**, pp. 16349–16356.

109 Kim, R.S., Zhu, J., Park, J.H., *et al.*: 'E-beam deposited Ag-nanoparticles plasmonic organic solar cell and its absorption enhancement analysis using FDTD-based cylindrical nano-particle optical model' *Opt. Express*, 2012, **20**, (12), pp. 12649–12657.

110 Tong, S.W., Zhang, C.F., Jiang, C.Y., *et al.*: 'Improvement in the hole collection of polymer solar cells by utilizing gold nanoparticle buffer layer' *Chem. Phys. Lett.*, 2008, **453**, (1), pp. 73–76.

111 Hao, J., Xu, Y., Chen, S., *et al.*: 'Broadband plasmon-enhanced polymer solar cells with power conversion efficiency of 9.26% using mixed Au nanoparticles' *Opt. Commun.*, 2016, **362**, pp. 50–58.

112 Wang, Y., Wang, H., Xing, X.: 'Nanosilver surface plasmon response enhanced the photovoltaic performance of organic solar cells' *Opt. - Int. J. Light Electron Opt.*, 2014, **125**, (19), pp. 5600–5602.

113 Chen, B., Zhang, W., Zhou, X., *et al.*: 'Surface plasmon enhancement of polymer solar cells by penetrating Au/SiO2 core/shell nanoparticles into all

organic layers' *Nano Energy*, 2013, **2**, (5), pp. 906–915.

114 Ma, C., Qin, W., Xu, X., *et al.*: 'Plasmon-enhanced organic solar cells with solution-processed three-dimensional Ag nanosheets' *Sol. Energy Mater. Sol. Cells*, 2013, **109**, pp. 227–232.

115 Hong, L., Rusli, W., Wang, X., *et al.*: 'Si/PEDOT:PSS hybrid solar cells incorporated with silver plasmonic nanospheres' *Thin Solid Films*, 2016, **599**, pp. 37–41.

116 Zhao, M., Zhang, J., Gao, N., *et al.*: 'Actively Tunable Visible Surface Plasmons in Bi2Te3 and their Energy-Harvesting Applications' *Adv. Mater.*, 2016, **28**, (16), pp. 3138–3144.

117 Lu, R., Xu, L., Ge, Z., *et al.*: 'Improved Efficiency of Silicon Nanoholes/Gold Nanoparticles/Organic Hybrid Solar Cells via Localized Surface Plasmon Resonance' *Nanoscale Res. Lett.*, 2016, **11**, (1), p. 160.

118 Saliba, M., Zhang, W., Burlakov, V.M., *et al.*: 'Plasmonic-Induced Photon Recycling in Metal Halide Perovskite Solar Cells' *Adv. Funct. Mater.*, 2015, **25**, (31), pp. 5038–5046.

119 Yang, X., Liu, W., Xiong, M., *et al.*: 'Au nanoparticles on ultrathin MoS_2 sheets for plasmonic organic solar cells' *J. Mater. Chem. A*, 2014, **2**, (36), pp. 14798–14806.

120 Shen, X., Xia, Z., Chen, L., Li, S., Zhao, J.: 'Optical and electrical enhancement for high performance hybrid Si/organic heterojunction solar cells using gold nanoparticles' *Electrochim. Acta*, 2016, **222**, pp. 1387–1392.

121 Mahmoudi, T., Seo, S., Yang, H.-Y., Rho, W.-Y., Wang, Y., Hahn, Y.-B.: 'Efficient bulk heterojunction hybrid solar cells with graphene-silver nanoparticles composite synthesized by microwave-assisted reduction' *Nano Energy*, 2016, **28**, pp. 179–187.

122 Hsu, H.-L., Juang, T.-Y., Chen, C.-P., *et al.*: 'Enhanced efficiency of organic and perovskite photovoltaics from shape-dependent broadband plasmonic effects of silver nanoplates' *Sol. Energy Mater. Sol. Cells*, 2015, **140**, pp. 224–231.

123 Lee, Y.H., Kim, D.H., Kim, T.W.: 'Enhancement of the power conversion efficiency due to the plasmonic resonant effect of Au nanoparticles in ZnO nanoripples' *Org. Electron.*, 2016, **37**, pp. 74–79.

124 Chan, K.H., Elumalai, N.K., Tayebjee, M.J.Y., Uddin, A., Pillai, S.: 'Dark carrier dynamics and electrical characteristics of organic solar cells integrated with Ag-SiO_2 core-shell nanoparticles' *Synth. Met.*, 2017, **223**, pp. 34–42.

125 Liu, Z., Xu, L., Zhang, W., *et al.*: 'Extended short-wavelength spectral response of organic/(silver nanoparticles/Si nanoholes nanocomposite films) hybrid solar cells due to localized surface plasmon resonance' *Appl. Surf. Sci.*, 2015, **334**, pp. 110–114.

126 Valdez, J., Bawage, S., Gomez, I., Singh, S.R.: 'Facile and rapid detection of respiratory syncytial virus using metallic nanoparticles' *J. Nanobiotechnology*, 2016, **14**, p. 13.

127 Sengani, M., Grumezescu, A.M., Rajeswari, V.D.: 'Recent trends and methodologies in gold nanoparticle synthesis – A prospective review on drug delivery aspect' *OpenNano*, 2017, **2**, pp. 37–46.

128 Fritea, L., Bănică, F., Costea, T.O., Moldovan, L., Iovan, C., Cavalu, S.: 'A gold nanoparticles - Graphene based electrochemical sensor for sensitive determination of nitrazepam' *J. Electroanal. Chem.*, 2018, **830**–**831**, pp. 63–71.

129 Chen, H., Zhou, K., Zhao, G.: 'Gold nanoparticles: From synthesis, properties to their potential application as colorimetric sensors in food safety screening' *Trends Food Sci. Technol.*, 2018, **78**, pp. 83–94.

130 González, V., Puente, C., López, I.: 'Nanomaterials for Printing Technology: A Revolution in Industrial Manufacturing' *Handb. Nanomater. Ind. Appl.*, 2018, pp. 1012–1030.

131 Luo, J., Chen, J., Wang, H., Liu, H.: 'Ligand-exchange assisted preparation of plasmonic Au/TiO_2 nanotube arrays photoanodes for visible-light-driven photoelectrochemical water splitting' *J. Power Sources*, 2016, **303**, pp. 287–293.

132 Borran, A.A., Aghanejad, A., Farajollahi, A., Barar, J., Omidi, Y.: 'Gold nanoparticles for radiosensitizing and imaging of cancer cells' *Radiat. Phys. Chem.*, 2018, **152**, pp. 137–144.

133 Dahan, I., Sorrentino, S., Boujemaa-Paterski, R., Medalia, O.: 'Tiopronin-Protected Gold Nanoparticles as a Potential Marker for Cryo-EM and Tomography' *Structure*, 2018, **26**, (10), pp. 1408–1413.

134 Staykov, A., Miwa, T., Yoshizawa, K.: 'Aerobic oxidation of alkanes on icosahedron gold nanoparticle Au55' *J. Catal.*, 2018, **364**, pp. 141–153.

135 Zhang, K., Shen, M., Liu, H., Shang, S., Wang, D., Liimatainen, H.: 'Facile synthesis of palladium and gold nanoparticles by using dialdehyde nanocellulose as template and reducing agent' *Carbohydr. Polym.*, 2018, **186**, pp. 132–139.

136 Zarzuela, R., Luna, M.J., Gil, M.L.A., *et al.*: 'Analytical determination of the reducing and stabilization agents present in different Zostera noltii extracts used for the biosynthesis of gold nanoparticles' *J. Photochem. Photobiol. B*

Biol., 2018, **179**, pp. 32–38.

137 Hamelian, M., Hemmati, S., Varmira, K., Veisi, H.: 'Green synthesis, antibacterial, antioxidant and cytotoxic effect of gold nanoparticles using Pistacia Atlantica extract' *J. Taiwan Inst. Chem. Eng.*, 2018, **93**, pp. 21–30.

138 Qiu, W.-Y., Wang, K., Wang, Y.-Y., *et al.*: 'pH dependent green synthesis of gold nanoparticles by completely C6-carboxylated curdlan under high temperature and various pH conditions' *Int. J. Biol. Macromol.*, 2018, **106**, pp. 498–506.

139 Tan, N.P.B., Lee, C.H., Li, P.: 'Influence of temperature on the formation and encapsulation of gold nanoparticles using a temperature-sensitive template' *Data Br.*, 2015, **5**, pp. 434–438.

140 Liu, X., Atwater, M., Wang, J., Huo, Q.: 'Extinction coefficient of gold nanoparticles with different sizes and different capping ligands' *Colloids Surfaces B Biointerfaces*, 2007, **58**, (1), pp. 3–7.

141 Ruankham, P., Wongratanaphisan, D., Gardchareon, A., Phadungdhitidhada, S., Choopun, S., Sagawa, T.: 'Full coverage of perovskite layer onto ZnO nanorods via a modified sequential two-step deposition method for efficiency enhancement in perovskite solar cells' *Appl. Surf. Sci.*, 2017, **410**, pp. 393–400.

142 Gwozdz, K., Placzek-Popko, E., Zielony, E., *et al.*: 'Deep traps in the ZnO nanorods/Si solar cells' *J. Alloys Compd.*, 2017, **708**, pp. 247–254.

143 Huang, Z.-L., Chen, C.-M., Lin, Z.-K., Yang, S.-H.: 'Efficiency enhancement of regular-type perovskite solar cells based on Al-doped ZnO nanorods as electron transporting layers' *Superlattices Microstruct.*, 2017, **102**, pp. 94–102.

144 Ebadi, M., Zarghami, Z., Motevalli, K.: '40% Efficiency enhancement in solar cells using ZnO nanorods as shell prepared via novel hydrothermal synthesis' *Phys. E Low-dimensional Syst. Nanostructures*, 2017, **87**, pp. 199–204.

145 Govindaraj, R., Santhosh, N., Senthil Pandian, M., Ramasamy, P.: 'Synthesis of nanocrystalline TiO_2 nanorods via hydrothermal method: An efficient photoanode material for dye sensitized solar cells' *J. Cryst. Growth*, 2017, **468**, pp. 125–128.

146 Kislyuk, V. V, Dimitriev, O.P.: 'Nanorods and nanotubes for solar cells.' *J. Nanosci. Nanotechnol.*, 2008, **8**, (1), pp. 131–148.

147 Iqbal, P., Preece, J.A., Mendes, P.M.: 'Nanotechnology: The "Top-Down" and "Bottom-Up" Approaches', in 'Supramolecular Chemistry' (2012)

148 Teo, B.K., Sun, X.H.: 'From top-down to bottom-up to hybrid

nanotechnologies: Road to nanodevices' *J. Clust. Sci.*, 2006, **17**, (4), pp. 529–540.

149 Houng, M., Lu, W., Yang, T., Lee, K.: 'Characterization of the Nanoporous Template Using Anodic Alumina Method' *J. Nanomater.*, 2014, **2014**, pp. 1–7.

150 Heakal, F.E.-T., Shehata, O.S., Awad, A.M.: 'Relevant aspects in the stability performance of different anodic alumina (AAO) films in aqueous sulfate solutions' *J. Electroanal. Chem.*, 2017, **792**, pp. 95–103.

151 Yin, H., Li, X., Que, L.: 'Fabrication and characterization of aluminum oxide thin film micropatterns on the glass substrate' *Microelectron. Eng.*, 2014, **128**, pp. 66–70.

152 O'Regan, B., Grätzel, M.: 'A low-cost, high-efficiency solar cell based on dye-sensitized colloidal TiO2 films' *Nature*, 1991, **353**, (6346), pp. 737–740.

153 Hagen, J., Schaffrath, W., Otschik, P., *et al.*: 'Novel hybrid solar cells consisting of inorganic nanoparticles and an organic hole transport material' *Synth. Met.*, 1997, **89**, (3), pp. 215–220.

154 Choi, H., Paek, S., Lim, N., Lee, Y.H., Nazeeruddin, M.K., Ko, J.: 'Efficient perovskite solar cells with 13.63 % efficiency based on planar triphenylamine hole conductors.' *Chemistry*, 2014, **20**, (35), pp. 10894–9.

155 Choi, H., Do, K., Park, S., Yu, J.-S., Ko, J.: 'Efficient Hole Transporting Materials with Two or Four N,N-Di(4-methoxyphenyl)aminophenyl Arms on an Ethene Unit for Perovskite Solar Cells.' *Chemistry*, 2015, **21**, (45), pp. 15919–23.

156 Kao, T.-T., Chiu, Y.-Y.: 'Fabrication and wetting characteristics of vertically self-aligned ZnO nanorods formed by anodic aluminum oxide template' *J. Micro/Nanolithography, MEMS, MOEMS*, 2014, **13**, (1), p. 013003.

157 Jo, H., Sohn, A., Shin, K.S., *et al.*: 'Novel architecture of plasmon excitation based on self-assembled nanoparticle arrays for photovoltaics' *ACS Appl. Mater. Interfaces*, 2014, **6**, (2), pp. 1030–1035.

158 Ansari, F., Ghaedi, M., Taghdiri, M., Asfaram, A.: 'Application of ZnO nanorods loaded on activated carbon for ultrasonic assisted dyes removal: Experimental design and derivative spectrophotometry method' *Ultrason. Sonochem.*, 2016, **33**, pp. 197–209.

159 Yu, X., Yu, X., Zhang, J., Zhang, D., Chen, L., Pan, H.: 'Improve the near-UV/blue light scattering of ZnO nanorods via Mg-doping' *Superlattices Microstruct.*, 2016, **100**, pp. 38–44.

160 Yatskiv, R., Grym, J.: 'Luminescence properties of hydrothermally grown ZnO nanorods' *Superlattices Microstruct.*, 2016, **99**, pp. 214–220.

161 Al-Ruqeishi, M.S., Mohiuddin, T., Al-Habsi, B., Al-Ruqeishi, F., Al-Fahdi, A., Al-Khusaibi, A.: 'Piezoelectric nanogenerator based on ZnO nanorods' *Arab. J. Chem.*, 2016.

162 He, H., Cai, W., Lin, Y., Chen, B.: 'Surface decoration of ZnO nanorod arrays by electrophoresis in the Au colloidal solution prepared by laser ablation in water' *Langmuir*, 2010, **26**, (11), pp. 8925–8932.

163 Sabri, N.S., Yap, C.C., Yahaya, M., Haji Jumali, M.H., Mat Salleh, M.: 'Optimizing the performance of inverted type hybrid organic solar cell based on ZnO/P3HT with various polymer deposition parameters' *J. Mater. Sci. Mater. Electron.*, 2016.

164 Liu, S., Xiong, Z., Zhu, C., Li, M., Zheng, M., Shen, W.: 'Fast anodization fabrication of AAO and barrier perforation process on ITO glass.' *Nanoscale Res. Lett.*, 2014, **9**, (1), p. 159.

165 Pourjafari Nokandeh, D.: 'Synthesis of zinc oxide nanorods via conductive polymeric template and its potential application in hybrid solar cells'. UANL, 2014

166 Ali, M.R.K., Snyder, B., El-Sayed, M.A.: 'Synthesis and Optical Properties of Small Au Nanorods Using a Seedless Growth Technique' *Langmuir*, 2012, **28**, (25), pp. 9807–9815.

167 Akinci, Z.B., Urgen, M.: 'A Simple Method for the Production of AAO Templates for DC Electrodeposition of Nanostructures' *ECS Electrochem. Lett.*, 2014, **3**, (10), pp. D46–D49.

168 Hussein, A.A., Sultan, A.A., Obeid, M.T., Abdulnabi, A.T., Ali, M.T.: 'Synthesis and Characterization of poly(3-hexylthiophene)' *Int. J. Sci. Eng. Appl. Sci.*, 2015, **1**, (17), pp. 2395–3470.

169 Ansari, M.A., Mohiuddin, S., Kandemirli, F., Malik, M.I.: 'Synthesis and characterization of poly(3-hexylthiophene): improvement of regioregularity and energy band gap' *RSC Adv.*, 2018, **8**, (15), pp. 8319–8328.

170 Floresyona, D., Goubard, F., Aubert, P.-H., *et al.*: 'Highly active poly(3-hexylthiophene) nanostructures for photocatalysis under solar light' *Appl. Catal. B Environ.*, 2017, **209**, pp. 23–32.

171 Thanh, N.V.K., Giang, N.D., Vinh, L.Q., Dat, H.T.: 'A Low Cost Microwave Synthesis Method for Preparation of Gold Nanoparticles' *Commun. Phys.*, 2014, **24**, (2), p. 146.

172 Baffou, G.: 'Mie theory for metal nanoparticles' (2017), pp. 1–2